Investigations of the SAA and the long-time behavior of Vela X-1

Diploma Thesis of

Felix Fürst

from Stuttgart, Germany

performed at the

Dr. Karl Remeis-Sternwarte Bamberg
(Astronomical Institute of the University of Erlangen-Nuremberg)
Sternwartstr. 7, 96049 Bamberg

supervisor:

Prof. Dr. Jörn Wilms

24. September 2008

To my mother,
who I will always love and never forget.

Zusammenfassung

Für diese Diplomarbeit wurden zwei recht verschiedene Themen bearbeitet. Der erste Teil beschäftigt sich mit der Südatlantischen Anomalie (SAA), einer Region von erhöhtem Teilchenhintergrund in erdnahen Satellitenorbits. Die SAA wird mit Hilfe des Teilchenmonitors an Bord des „Rossi X-ray Timing Explorers“ (*RXTE*) vermessen. Daraus wird die Position der SAA an Hand der Maxima von Weibull-Fits an den Teilchenhintergrund bestimmt. Die Position der SAA ändert sich durchschnittlich mit circa $0.3\,\mathrm{deg\,a^{-1}}$, wobei aber gezeigt wird, dass es zwei deutliche Sprünge in der gleichförmigen Bewegung gibt. Diese Unstetigkeitsstellen werden zum ersten Mal gesehen und ausgemessen und in Verbindung mit so genannten „geomagnetic jerks“ gebracht. „Geomagnetic jerks“ sind plötzliche Sprünge in der kontinuierlichen Veränderung des Erdmagnetfeldes und haben dadurch auch Einfluss auf den Teilchenhintergrund. Außerdem werden Karten der SAA auf Quartalsbasis angelegt, die eine räumliche Auflösung von 0,25 deg in geographischer Länge und 0,5 deg in geographischer Breite sowie 10 km in Höhe haben. Aus diesen Karten und den Fits wird die Veränderung der Größe und Stärke der SAA bestimmt. Es wird gezeigt, dass die Größe der SAA sich antizyklisch zur Sonnenaktivität ändert.

Der zweite Teil der Arbeit untersucht den Neutronenstern Vela X-1. Das Binärsystem Vela X-1 besteht aus einem der schwersten bekannten Neutronensterne und einem roten Überriesen. Der europäische Satellit „International Gamma-Ray Observatory“ (*INTEGRAL*) hat inzwischen über 3 Msec lang das System beobachtet. Diese Daten werden in dieser Arbeit reduziert und analysiert. Dabei werden zwei verschieden Zustände von Vela X-1 gefunden, ein leuchtstärkerer dafür weicherer und ein leuchtschwächerer und härterer Zustand. Für jeden dieser Zustände wird separat ein Spektrum extrahiert. Die bekannte Zyklotronline bei circa 50 keV kann darin bestätigt werden. Darüberhinaus wird die Leuchstärke mit statistischen Mitteln analysiert. Diese zeigt eine breite Schwankung um bis zu Faktor 70. Es wird gezeigt, dass die Leuchtstärke einer log-normal Verteilung folgt. Dies wird mit einem klumpigen Wind des optischen Begleiters erklärt.

Abstract

In this diploma thesis two quite different topics are covered. The first part investigates the "South Atlantic Anomaly" (SAA), a region with increased particle background in low-earth orbits of satellites. The SAA is measured by means of the particle monitor aboard the "Rossi X-ray Timing Explorer" (*RXTE*). With these data the position of the SAA is determined by calculating the position of the maximum of Weibull fits to the particle background. The position of the SAA is changing on average with about $0.3\,\mathrm{deg\,yr^{-1}}$, but it is shown that there are two distinct irregularities in this uniform movement. These irregularities are seen an examined closer for the first time and are connected to so-called "geomagnetic jerks". Geomagnetic jerks are sudden jumps in the continuous change of Earth's magnetic field and thus have an influence onto the particle background. Furthermore maps of the SAA on a quarter a year basis are made, with a spatial resolution of 1/4 deg in longitude and 1/2 deg in latitude as well as 10 km in altitude. With the help of these maps and the fits changes in size and power of the SAA is determined. It is shown, that the size of the SAA varies antiphased to the solar activity.

In the second part of this work the neutron star Vela X-1 is investigated. The binary system Vela X-1 consist of one of the heaviest known neutron stars and a red hypergiant. The European satellite "International Gamma-Ray Observatory" (*INTEGRAL*) accumulated by now more than 3 Msec of data from this system. These data is reduced and analyzed in this work. Two different states are found, one brighter and softer and one dimmer and harder state. For each of these states a spectrum is fitted. The well known cyclotron line at about 50 keV can be confirmed therein. Additionally the luminosity is analyzed statistically. The luminosity shows a strong variance by factor 70. It is shown, that the luminosity is following a log-normal distribution, which can be explained by the clumped stellar wind of the optical companion.

Contents

The small image on the title page shows the eastern dome of the Dr. Karl-Remeis-Observatory in Bamberg, Germany.

Röntgen's X-rays will turn out to be an elaborate hoax.

(Lord Kelvin)

1 Introduction

THE field of X-ray astronomy has been one of the most vivid fields of astronomy in the last 30 years. As the atmosphere of the Earth is opaque to X-rays it was necessary to develop means which could carry X-ray detectors above the atmosphere to effectively measure X-ray radiation from the universe. The first measurement of X-rays from out of space was carried out in 1946 by Golian and his collaborators at the Naval Research Lab (NRL). Using captured V2 rockets and Geiger counters, they detected strong X-rays from the sun (Golian et al., 1946). But these detections did not spur a more intensive search for other cosmic X-rays sources, but on contrary slowed it down. The reason was when calculating the X-ray luminosity of stars using a blackbody ansatz, it was found that the detectors by far could not detect any radiation. It was only in 1962 when another important X-ray mission was launched. The goal of that mission was to detect X-ray emission from the moon as part of the preparation for the lunar landing. It was a rocket mission of a group at American Science and Engineering (AS&E) led by R. Giacconi and B. Rossi. They did not detect any X-rays from the moon, but in the course of the experiment scanned parts of the surrounding sky, too. There they found a very strong source of X-rays, which they called Scorpius X-1. It was soon found that Sco X-1 must be an extra-solar source which releases an amount of energy which was thought to be almost impossible (Giacconi et al., 1962). Sco X-1 has an energy output in X-rays of about 60 000 times that of the sun. This was the start of X-ray astronomy. X-ray astronomy today allows us to investigate physics at very high temperatures and energies and allows us to test different theories, for example Einstein's theory of relativity.

To be able to observe one source quasi-continuously and to monitor the X-ray sky over a long range of time, almost all modern X-ray investigations are carried out using satellites. The first X-ray satellite to orbit the Earth was *Uhuru* in 1971. The observations by R. Giacconi and E. Schreier (Giacconi et al., 1971) done with *Uhuru* led to the detection of pulses of Cen X-3. This detection was the first proof for a rotating neutron star. Many more sources, galactic and extra-galactic were found with *Uhuru* (Giacconi et al., 1974). It became necessary to map the sky even more thor-

oughly, not least to distinguish well between sources and background. A major step into that direction was the launch of the "Einstein Observatory" in 1978 (Schreier, 1978). It was the first fully imaging X-ray telescope and thus was, amongst other, able to analyze the extended X-ray regions of supernova remnants. The first European X-ray astronomy satellite and the successor of "Einstein" was the "European X-Ray Observatory Satellite" (EXOSAT), launched in 1983 (Taylor et al., 1981). It was able to first detect quasiperiodic oscillations in binary systems, which up to date are an intersting field of research. The most important sky-mapping experiment was the RASS, the *ROSAT* All Sky Survey. It was carried out on the "RÖntgenSATellit" (*ROSAT*) a German X-ray satellite launched in 1990 (see, e.g., Trümper, 1990). *ROSAT* mapped over 150 000 individual sources. Today the Earth is orbited by at least 6 different X-ray astronomy satellites, which provide data in differrent energy bands from about 0.1 keV up to more then 300 keV. Among the most important of these one should name "XMM-Newton" (de Chambure et al., 1999), "Chandra" (Weisskopf et al., 2000) and "Suzaku" (Kelley & Mitsuda, 2002). The two newest members of the high energy satellite community are the Italian "Astro-rivelatore Gamma ad Immagini LEggero" (*AGILE*) (Basset & The AGILE Team, 2007) and the American "Fermi Gamma-ray Space Telescope" (Michelson, 2008). The Fermi telescope was formally known as "Gamma-ray Large Area Space Telescope" (*GLAST*) and renamed on 2008 August 28 (Harrington et al., 2008). *AGILE* was successfully started on 2007 April 23 while *GLAST* is in orbit only since 2008 June 11. Both satellites are built for very high energies of some MeV. *AGILE* already detected some sources in these very high energies, see, e.g., Verrecchia et al. (2008) and Pittori et al. (2008). The checkout phase of *GLAST* was ended on 2008 August 13 and a first image of the sky as seen by its instruments was realeased on 2008 August 28 (Ritz, 2008). A nice overview over past and present X-ray astronomy satellite missions can be found on the homepage of NASA's High Energy Astrophysics Science Archive Research Center (HEASARC)[1]. Each one of these satellites is a very sophisticated machine, which carries hi-tech but unfortunately very damageable instruments. That is the reason why most of these satellites carry not only telescopes to watch the cosmic X-rays, but also particle detectors to monitor the radiation environment of the satellite. Increased radiation in the environment can damage the instruments irreversibly. When measuring the environment, counter measurements like reducing the high voltage can be taken to minimize the risks to the devices. On the other hand, the radiation monitors allow us to investigate the radiation belts of the Earth in a wide area of space. Moreover, they allow us to monitor the magnetic field of the Earth, as the trapped radiation follows the magnetic field lines.

For this diploma thesis I used data from two different satellites, the "Rossi X-Ray Timing Explorer" (*RXTE*) and the "INTErnational Gamma-Ray Astrophysics Laboratory" (*INTEGRAL*). *RXTE* is a satellite in an almost circular low-Earth orbit with

[1] `http://heasarc.gsfc.nasa.gov/docs/heasarc/missions/`

an altitude of about 500 km and operated by NASA. It was launched in 1995 and is still in operation today. *INTEGRAL* on the other hand is in a very eccentric orbit with an apogee of about 153 000 km. It is operated by ESA and was launched in 2002. More details about the satellites are found in Sects. 2.1.3 and 3.2.

In the first part (Chap. 2) of this work I looked at data from the particle monitor of *RXTE*. In its orbit *RXTE* crosses a region called the "South Atlantic Anomaly" (SAA). This is a region of increased radiation background, and thus very important to modern spaceflight. I could access data taken constantly for over 12 years. These data were rebinned to a 0.25 degrees in longitude, 0.5 degrees in latitude and 10 km in altitude grid. Using the rebinned data I derived maps of the SAA which show its location very clearly and allowed us to follow the size and shape of the SAA through time and space. The data then was used to compare the size and power of the SAA to the 10.7 cm radio flux of the sun. The 10.7 cm solar radio flux is a good gauge for solar activity. I could find a good anticorrelation with a 1 year time lag. Furthermore I investigated the drift rate of the SAA. I measured an average drift rate of about $0.3\,\mathrm{deg\,year^{-1}}$ westwards. Additionally I found irregularities in the drift rate, where the SAA moves suddenly backwards. The most prominent of these irregularities was found in the second quarter of 2003. This is the first time, that variations from the smooth movement are measured. The variations could be correlated with "geomagnetic jerks", which are sudden changes in the secular variation of the magnetic field.

In the second part (chapter 3) of this diploma thesis I discuss *INTEGRAL* data of Vela X-1. Vela X-1 is a binary system containing a neutron star and is showing strong X-ray emission. Neutron stars are the most compact objects in the universe, except for black holes. This means they exhibit some very special physical behavior and help us to understand the forces which act in atomic nuclei. As Vela X-1 has been studied for a long time already (there are about 200 papers about the object directly, almost 1000 about it in general), I studied all public available data of Vela taken with *INTEGRAL*. I found that there are brighter and dimmer parts in the Lightcurve which correspond to softer and harder spectra. I investigated the difference between the spectra of the soft and hard state, especially regarding the "Cyclotron Resonant Scattering Features" (CRSF). CRSF are absorption line-like features, produced by resonant scattering of photons on electrons in extreme magnetic fields. I did not find any change in the CRSF during the different states. Additionally I took a look at the flaring behavior of Vela X-1. I found that the brightness of Vela is distributed following a log-normal distribution. In the soft band, a distinct excess in the bright flank from the log-normal distribution was measured. I calculated the possibility of very intense flares, similar to the ones found by Kreykenbohm et al. (2008). To reduce the noise in the data, Bayesian Blocks were used to further investigate the distribution of the flares. Furthermore I investigated the ingress and egress of the eclipse of Vela X-1. A peculiar eclipse is found, which exhibits characteristic bumps before and after

the eclipse. I interpret these bumps as being due to the accretion stream.

Chapter 4 finally summarizes the findings and gives a brief outlook to future works.

Magnus magnes ipse est globus terrestris.

(William Gilbert, "De Magnete")

2 The South Atlantic Anomaly

Contents

2.1 Introduction

THIS section is about my findings of the temporal variations of the "South Atlantic Anomaly" (SAA). I show a very detailed look at the size and shape of the SAA on a data basis which lasts for over 12 years. In the first section 2.1.1 the basics of geomagnetically trapped radiation, the radiation belts, and the SAA are explained. In Sect. 2.1.2 some prior works on the SAA and its variations are recapitulated and put into context to this work. My analysis is based upon data taken with the "Rossi X-ray Timing Explorer" (*RXTE*). In Sect. 2.1.3 *RXTE* is described, with special regard of HEXTE and its particle monitor. In the Sect. 2.2 my data extraction pipeline is explained and maps of the SAA are shown. In Sect. 2.3 the results about the location and the drift of the SAA are shown. In the last Sect. 2.4 I summarize my results

and discuss some future interrogations. Parts of this chapter are based on Fürst et al. (2008), and thus adopt the "we"-style used in that paper.

2.1.1 Geomagnetically trapped radiation

The magnetic field of the Earth has been known for a very long time and can be seen in everyday life for example when using a compass. In his book "De Magnete" from 1600 William Gilbert was the first to note that the Earth was a giant magnet (Gilbert, 1991, facsimile). Earth-scientists and geomagnetists have since then tried to evaluate the exact shape and power of the magnetic field. In a crude approximation the field can be seen as an inclined, off-center magnetic dipole. The offset is about 500 km from the Earth's center towards Southeast Asia, the inclination is about 11 degrees (see Pinto et al., 1992). This model does of course not express in any way the physical formation of the field but is just an experimental approximation. As for the formation of the field, the most accepted theory today is the so called "Dynamo Theory", which was first proposed by Elsasser (1946) to be applicable to the Earth. According to this theory, the movements of the fluid outer core of the Earth are responsible for the field. The outer core, consisting mainly of molten iron, is highly conducting and driven by convection and the Coriolis force. These motions induce electric currents and magnetic fields, which are more or less well aligned along the rotation axis of the Earth. Through complex magnetohydrodynamical calculations it can be shown, that these currents are self-reinforcing and thus stable (Roberts & Glatzmaier, 2000). Because of the complexity of this process the emerging magnetic field is very complex and highly dynamically. Additionally other factors do participate to the overall shape of the geomagnetic field, such as magnetized rocks or the ring current in the magnetosphere. This work is focused on trapped particles in the vicinity of the Earth, where the field produced through the dynamo is by far the most important one (Walt, 1994). To accommodate for the complexity of the magnetic field the International Association of Geomagnetism and Aeronomy (IAGA) releases a new field model every 5 years. The model is called International Geomagnetic Reference Field (IGRF) and the newest issue is number 10. See Fig. 2.1.1 for a plot of the field intensity of this model at the surface of the Earth. Comparing the IGRF field to the aforementioned dipole approximation, it can be seen, that the dipole can account for the facts that the poles are around 130° east and −60° south and around 100° east and 60° north as well as for the region of weakend field around South America and the south Atlantic.

The magnetic field is not restricted to the surface of the Earth, but extends far into space. But until the 1950s it was not known that the magnetic field in the outer envelope of the near-Earth region is not empty, but contains a dynamic population of charged particles. This particles could be first measured by van Allen (1958) with the spacecrafts Explorer 1 and 3. It was shown that the particles are mostly found

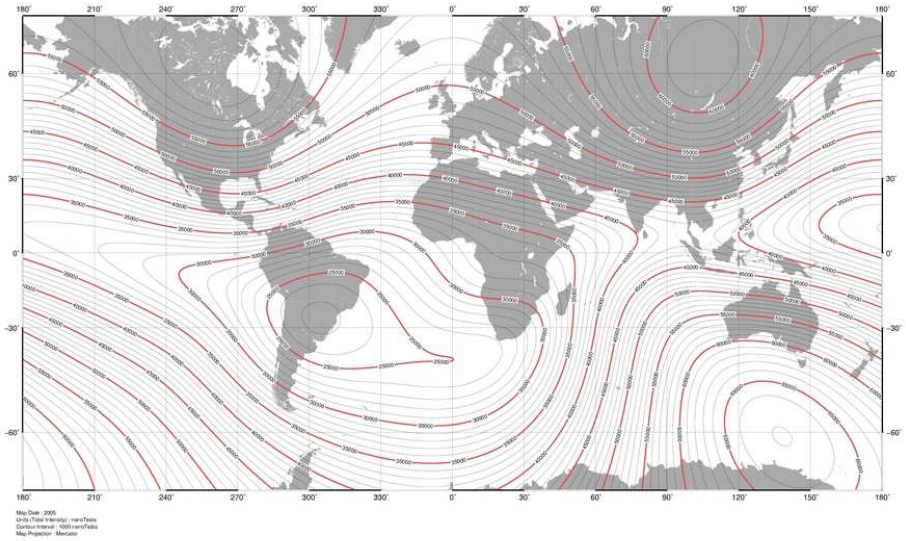

Figure 2.1.1: The Main Field Total Intensity of the 10th IGRF for the Epoch 2005. (`ftp://ftp.ngdc.noaa.gov/Solid_Earth/Mainfld_Mag/images/F_map_mf_2005_large.jpeg`)

in spatial regions, which look like shell structures around the Earth. These regions are accordingly called "radiation belts" or "van-Allen-belts". These particles must be trapped through the magnetic field of the Earth, which was deduced by van Allen (1958) already. How charged particles can be trapped in this field can be seen by calculating the Lorentz-force $\vec{F_{\mathrm{L}}} = q\left(\vec{E} + \vec{v} \times \vec{B}\right)$ acting on the particles. For the actual magnetic field this can not be done analytically. Nonetheless the main results are achieved when approximating the field as a dipole. The following calulations are based on (Walt, 1994) and (Prölss, 2001). In the first step, let us regard a homogeneous magnetic field without any electric field. As the Lorentz-force is proportional to the vector-product $\vec{v} \times \vec{B}$ of the velocity of the particle and the magnetic field, only the velocity-component $v_\perp$ perpendicular to the magnetic field will contribute to the Lorentz-force.

$$\vec{F}_{\mathrm{L}} = q\vec{v}_\perp\vec{B} \tag{2.1}$$

This means, the particle will be forced onto a circular path. The radius of the circle will be determined by the restriction, that the Lorentz-force and the centrifugal force F_{cen} have to balance each other,

$$F_{\mathrm{cen}} = \frac{mv_\perp^2}{\rho} = qv_\perp B = F_{\mathrm{L}} \tag{2.2}$$

where ρ is the radius of the circle, which is called gyroradius or cyclotron radius. Let us now regard an inhomogeneous magnetic field, which changes its intensity parallel

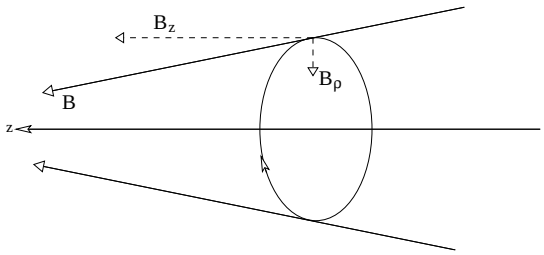

Figure 2.1.2: Sketch of the path of a particle in a inhomogeneous magnetic field (after Walt (1994))

to the magnetic field lines (see Fig. 2.1.2). We can then split the magnetic field vector into two components, one in the plane of the circular motion, called B_ρ, and one perpendicular to it, called B_z, which causes the circular motion in the first place. The force exhibited by B_ρ can be calculated via

$$\vec{F}_z = q\left(\vec{v} \times \vec{B}_\rho\right) = qv_\perp \vec{B}_\rho \tag{2.3}$$

To calculate B_ρ, we remember the Maxwell-Equation $\vec{\nabla}\vec{B} = 0$. Taking cylindrical coordinates and assuming azimuthal symmetry we can conclude that

$$B_\rho = -\frac{r}{2}\frac{\partial B_z}{\partial z} \tag{2.4}$$

Which leads, when inserted into equation 2.3, directly to

$$F_z = -qv_\perp \frac{\rho}{2}\frac{\partial B_z}{\partial z} \cdot \hat{e}_z = -\frac{mv_\perp^2}{2b}\frac{\partial B_z}{\partial z} \cdot \hat{e}_z \tag{2.5}$$

where $\hat{e}_z$ is the unit vector in the z-direction and the transformation was done using equation 2.2. Equation 2.5 thus shows that the force on the particle is always directed in the opposite direction of the magnetic field gradient, independent of the charge of the particle. When a charged particle is injected into such a inhomogeneous magnetic field, with a velocity component v_z in positive z-direction, the force will slow down the particle in this direction and finally accelerate it in negative z-direction. This is the so called "mirroring". When we regard the dipole approximation of the magnetic field of the Earth we see that there is a strong gradient in the direction of both poles (Fig. 2.1.3).

These gradients mean that while the particles are gyrating around the magnetic field lines, they move into the direction of one pole, say the magnetic north pole. On their way there, they are getting slower, until they reach a point where their v_z velocity is zero. This point is called the "mirror point". After reaching the mirror point they will be accelerated in the other direction, following the magnetic field line across the

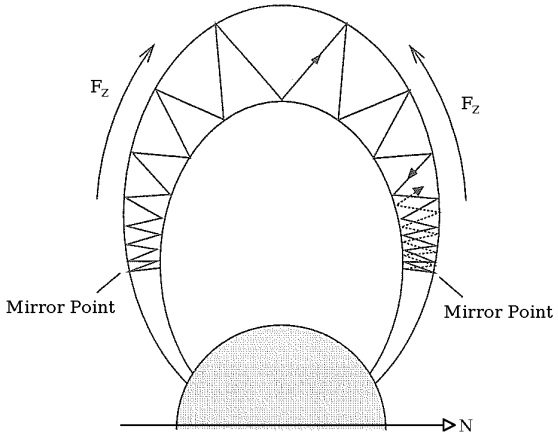

Figure 2.1.3: Sketch of the path of a particle mirroring in the geomagnetic field (after Prölss, 2001)

equator to the south pole. Again they will be slowed down, mirrored, and accelerated in the other direction. This idealized process is stable and particles which are injected from outside the magnetic field can become trapped. The mirror points of the particles depend strongly on the pitch angle α, which is defined by

$$\tan \alpha = \frac{v_\perp}{v_z} \tag{2.6}$$

Additionally the mirrorpoints depend on the absolute kinetic energy and the strength of the magnetic field. On their path around the Earth, the particles do not loose energy or change their pitch angel. This means, that one set of particles always mirrors at the same values of the magnetic field.

With the two effects of gyrating and mirroring, the particles are moving overall only in a 2-dimensional orbit, as the gyroradius can be neglected compared to the travelled distance while mirroring. To form the shell like structure which of the van-Allen-belts, we have to take to other effects into account, which cause the trapped particles to drift around the Earth. The first effect is the gradient drift in a inhomogeneous B-field with the gradient perpendicular to the fieldvector. The relation between the gyroradius ρ and the magnetic field strength B is $\rho \propto B^{-1}$. This means, a stronger B-field will result in a smaller gyroradius and thus the distance travelled in the x-direction perpendicular to the gyroradius (y-direction) and the magnetic field vector (z-direction) will be different. This leads to a net drift in that direction. The speed of this drift rate can be calculated to (see Prölss, 2001):

$$\vec{v}_g = \frac{mv_\perp^2}{2qB^3}\left(\vec{B}\times\vec{\nabla}B\right) \tag{2.7}$$

The second and more important effect causing a drift around the Earth is the curvature drift. This drift is due to the fact, that while following the curved magnetic field lines from north to south and back again, a centrifugal force acts upon the particles. Together with the B-field this force induces a force perpendicular to the magnetic field and the centrifugal force and thus results in a drift motion around the Earth. This drift is in the same direction as the gradient drift, which means eastwards for electrons, and westwards for protons. The drift rate can be calculated to

$$\vec{v}_c = \frac{mv_z^2}{qB^3}\left(\vec{B}\times\vec{\nabla}B\right) \tag{2.8}$$

This two drift motions can be added to the overall drift

$$\vec{v}_d = \frac{m}{2qB^3}\left(v_\perp^2 + 2v_z^2\right)\left(\vec{B}\times\vec{\nabla}B\right) \tag{2.9}$$

These three effects, namely the gyration, the mirroring and the overall drift are the three main effects on charged particles in the geomagnetic field. As their timescales are very different, they can be linearly superposed. Typical values of the timescales for 20 keV protons are 0.1 s for the gyration period, 1 min for the mirroring period and 9 h for the drift period around the Earth (Prölss, 2001). There are numerous additional effects, especially when the geomagnetic field is modelled more precisely and different inhomogeneities are to be regarded. Furthermore we have neglected any E-field which, of course, is present in the ionosphere. But these additional effects to not change the overall shape or formation of the radiation belts so they are not further investigated in this work.

The trapped particle population consists mainly of electrons with energies between 50 keV and 10 MeV and protons between 1 MeV and 100 MeV. For a 50 MeV proton the flux in the radiation belts is about $10^8\mathrm{m}^{-2}\mathrm{s}^{-1}$. The particles are either injected through the solar wind or cosmic rays or are produced in the so called "Cosmic Ray Albedo Neutron Decay" (CRAND) (see Prölss, 2001; Walt, 1994). In the CRAND process, cosmic rays which collide with atoms in the thicker atmosphere create free neutrons. These neutrons can drift into the radiation belts, and as neutrons are not stable, decay there via β-decay to protons, electrons and and anti-neutrinos.

$$n \longrightarrow p + e + \bar{\nu}_e \tag{2.10}$$

Killeen et al. (1963) have shown that these process can take place after nuclear bomb explosions in the upper atmosphere, too. The explosions inject neutrons in the atmosphere which decay rapidly. The resulting electrons become easily trapped and

thus increase the population of the radiation belts drastically. The details of particle diffusion, transport and lifetime in the radiation belts would lead to far for this work.

Let us now take again a look at the overall intensity of the magnetic field as seen in Fig. 2.1.1, looking closer at the region of weakend magnetic field over South America and the South Atlantic. This region is named "South Atlantic Magnetic Anomaly" (SAMA). We have seen that trapped particles always mirror at the same magnetic field strength. As the field strength in the SAMA is distinctly reduced, trapped particles will mirror at lower altitudes in this region. In fact, the altitude of the mirror points is decreased so far that satellites in low Earth orbits, with altitudes between 300 km and 600 km, are exposed to a drastically increased particle rate. The count rate increases about up to 2 decades. This region of increased count rate is called the "South Atlantic Anomaly" (SAA) and is one of the hazards to modern spaceflight. It can not only cause failure of microprocessors aboard satellites, bias measurements of cosmic sources, or overflow sensitive detectors, but it also poses a health hazard to astronauts. Therefore it is important to have good measurements of the size, shape, strength, and location of the SAA at any given time.

2.1.2 Former investigations of the SAA

There have been many works on the topic of the location and the movement of the SAA. To be able to predict the flux in the SAA, models have been developed to describe the particle environment. The most used of these models are the *AP-8/AE-8* models. The *AP-8* model for protons was released in 1976 and includes all data taken after 1970 (Sawyer & Vette, 1976), while the *AE-8* for electrons was released in 1991 (Vette, 1991). Both models together include data from over 43 satellites (Barth et al., 2003). Most of the previous works on the movement of the SAA compare recent measurements of the particle flux to the particle flux predicted by these models. Nonetheless, these models are based on data taken with older instruments which were not necessarily as sophisticated as modern devices. Garrett & Hastings (1994) caution that the models are very old, and that the particle background changes continuously. These authors name numerous reasons, like the decay of neutrons from atomic bomb explosions or the individuality of every solar cycle.

With the help of these models, Konradi et al. (1994) and Badhwar et al. (1994) have shown that the SAA is located distinctly more westwards in modern measurements, leading to an average annual movement of about $0.3\,\mathrm{deg\,year^{-1}}$. The derived drift rate depends on the accuracy of the models, of course. Grigoryan et al. (2005) have shown that the SAA has somewhat different sizes and locations in different energy bands. This change of shape leads to a systematic error when comparing older models to recent measurements, which have been made using different detectors. In an effort to

compare measurements made with an identical setup, Badhwar (1997) compared data taken 21.2 years apart, on *Skylab* during December 1973 and January 1974 and on *Mir* in March 1995. These authors found a drift rate of $0.28 \pm 0.03\,\mathrm{deg\,year^{-1}}$ westward which is in very good agreement with other measurements. Ginet et al. (2006) used a similar approach in comparing measurements from the Tri-Service Experiments Mission-5 (*TSX-5*) ranging from 2000–2006 to data from the Advanced Photovoltaic and Electronic Experiments (*APEX*) ranging from 1994–1996, resulting in a somewhat faster movement of $0.43 \pm 0.13\mathrm{deg\,year^{-1}}$. The long average of the *TSX-5* mission might be responsible for that discrepancy (Ginet et al., 2006). Another indirect way to measure the particle flux is to record Single Event Upsets (SEU) or Single Event Effects (SEE) in electronic devices, see, e.g., Lauriente et al. (1996), Mullen et al. (1998) or Adolphsen et al. (1995). These measurements bear a higher systematic error, as the upsets can be caused by particles with different energies or even by cosmic rays. This uncertainty is reflected in the larger scatter of the derived movement rates, which vary between $0.19\,\mathrm{deg\,year^{-1}}$ and $0.4\,\mathrm{deg\,year^{-1}}$.

A shortcoming of all of these previous studies, however, is that most of the measurements were taken with detectors on missions with a short lifetime, like, e.g., manned spacecrafts. Therefor only pointwise data are available, even if they were taken over a long range of time. This means that short time variations of the drift rate of the SAA had to be ignored.

2.1.3 The Rossi X-ray Timing Explorer

For our analysis we used data taken by the Rossi X-Ray Timing Explorer (*RXTE*), which is a satellite based X-ray detector. It was launched on 1995 December 30th, and started orbiting the Earth in a circular low-Earth orbit (LEO) with an altitude of about 592 km. Since then the altitude was reduced to about 488 km in December 2007 due to atmospheric drag. *RXTE* is still in operation today and the current status and location of the satellite can be checked in the internet[1]. The inclination of the orbit is 23 deg. The inclination is defined as the angle between the equatorial plane of the Earth and the orbital plane of the satellite. Through that definition, the inclination gives the northernmost and southernmost latitude the satellite reaches. This means that the orbit of *RXTE* moves through the SAA but does not reach the very center of that region. Aboard *RXTE* three different instruments are situated which allow for a energy range coverage from 2 – 200 keV: the Proportional Counter Array (PCA), the All-Sky Monitor (ASM) and the High Energy Timing Experiment (HEXTE). See Fig. 2.1.4 for a sketch of the satellite and its instruments. *RXTE*'s main goal is to investigate the physics of compact objects, i.e., white dwarfs, neutron stars and black

[1] `http://heasarc.gsfc.nasa.gov/docs/xte/SOF/CurrentLocation3.html`

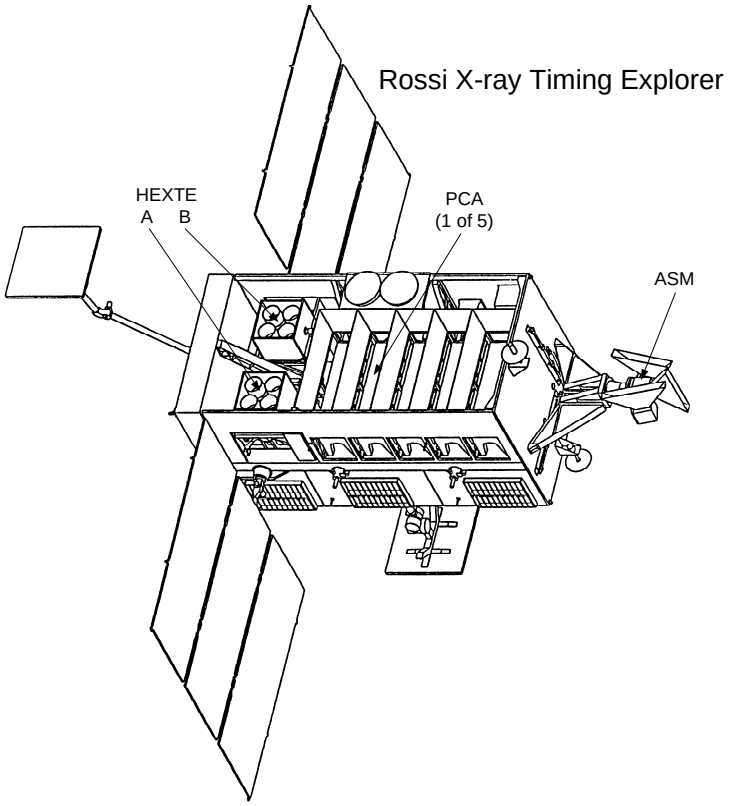

Figure 2.1.4: Sketch of the RXTE spacecraft, clearly visible are the three instruments (from left to right): HEXTE, PCA, ASM (from `http://mamacass.ucsd.edu/hexte/pictures/rxte_label1.eps.gz`)

holes. To achieve this goal it has an extraordinary time resolution of about $1\,\mu$s.

As the name says, the PCA consists of five identical proportional chambers with a xenon/methane gas mixture in the main volume. It is sensitive in the range from $2 - 60\,$keV and can achieve timing with the accuracy of $1\,\mu$s. See Chapter 4 of the technical appendix F (Swank, 2007) or Jahoda et al. (2006) for a detailed description of the PCA.

The ASM aboard *RXTE* was built to fulfill three different tasks. Firstly, it scans

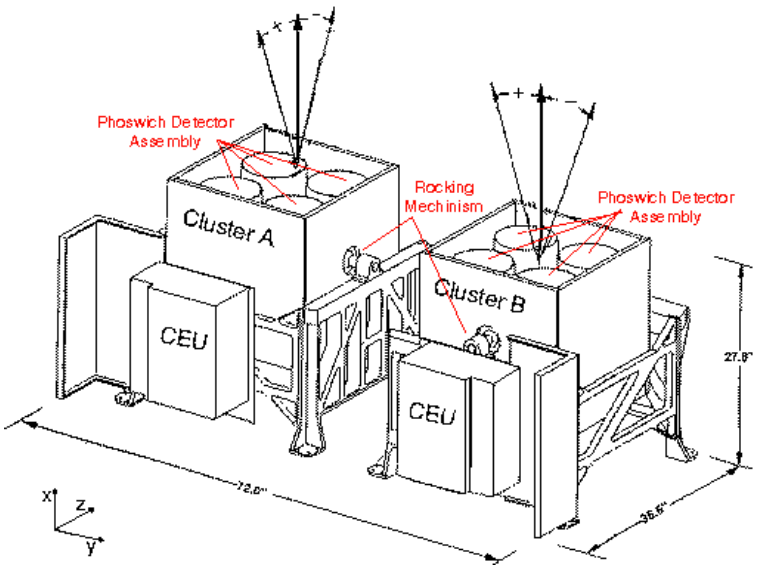

Figure 2.1.5: Sketch of HEXTE with the two independent clusters and the rocking mechanism clearly visible. (from `http://mamacass.ucsd.edu:8080/hexte/pictures/hexte_clusters_3d_sm1.gif`)

about 80% of the sky every 90 min. This means, the appearance of transients or other variable sources can be found quickly. Secondly, about 50 of the brightest X-ray sources are monitored with a time-resolution of 90 sec. This is helpful when analyzing the long-time behavior of these sources and constructing a flaring statistic, see Sect. 3.4. The third task is to study short-timed intensity variations from intense sources, as the cumulative count rate from each detector is saved and send back to Earth in 0.1 s bins. To achieve all these goals, the ASM consists of three identical Scanning Shadow Cameras (SSC), which can be rotated to some extend. A SSC is a position-sensitive proportional counter (PSPC) which views the sky trough a coded mask. The PSPCs are sensitive in the range of about 2 – 10 keV. The coded masks casts a shadow on the PSPC and this shadowgram can be deconvolved to the actual position in the sky. The coded mask technique is used in a more difficult way in the detectors of *INTEGRAL* as well and will be explained in Sect. 3.2 in more detail. In Chapter 6 of the technical appendix F (Swank, 2007) or in Levine et al. (1996) more details about ASM can be found.

HEXTE consists of two independent detector clusters (called A and B), each consisting of four NaI(Tl)/CsI(Na) phoswich scintillation counters. The counters are sensitive in the energy range 15 – 250 keV and provide a time resolution of 8 μs. See Fig. 2.1.5 for a sketch of HEXTE. The name phoswich counters comes from the fact, that the main counter NaI(Tl) is attached to a CsI(Na) shielding crystal. This shielding crystal

provides active anticoincidence shielding from X-rays not originating from the source in the field of view and additionally makes the NaI(Tl) scintillator uniformly visible to the photomultiplier. The X-rays are directed onto the scintillators via a collimator, consisting mainly of lead. The collimator consists of a honeycomb structure of hollow hexagonal tubes and provides a field of view at Full Width Half Maximum (FWHM) of 1°. As the X-ray background in the energy range of HEXTE is quite high, it is required to achieve a near-realtime background measurement. This is done by the so-called "rocking mechanism". The two detectors of HEXTE are mounted on a rotation axis, so that they can be moved away from the source for up to 3°. The rotation axes of the two detectors are perpendicular to each other, so that a spurious background source can be more easily identified. This can be clearly seen in Fig. 2.1.5. The rocking is done in the following way: while HEXTE A points to the source, HEXTE B is in the first background position. After a given time-interval between 16 s and 128 s, the detectors are moved, so that HEXTE A points on its first background position, while HEXTE B views the source. After the next time-interval HEXTE A is on-source again, while HEXTE B moved to the second background position, on the other side of the source. After the next step, where HEXTE A is in its other background position and HEXTE B is on-source the whole cycle is repeated. Of course, the guest-observer can give different-modi in which HEXTE is operated. For example, a staring mode is also possible, where one or both detectors are not rocking, but are staying fixed in either the on-source or off-source position. This mode has been used since 2006 October 20 for HEXTE A. This is due to the fact, that since the beginning of 2006 HEXTE A showed rocking anomalies and to prevent it of being stuck in the off-source position it was decided to fix it. The background of HEXTE A can be calculated through interpolation of the background of HEXTE B as the detectors are almost identical (Pottschmidt et al., 2006). The attempt to improve this background transfer led to the investigations of the SAA presented in this work. Another small setback with HEXTE incurred quite in the beginning of the mission on 1996 March 6, where one of the detectors of HEXTE B started to malfunction (Rothschild, 1996). Since then, only 3 of 4 detectors of HEXTE B are working, which must be taken in account when comparing count rates between the two detectors or trying to calculate the background for HEXTE A out of data from HEXTE B. The photomultipliers which are attached to the phoswich scintillators feature a 845 V high-voltage. These photomultipliers are very sensitive to energetic particles and can easily be permanently damaged. To prevent such damage the high-voltage is reduced to 220 V in case of increased background radiation. In order to do so the background radiation is constantly monitored using an separate particle monitor in each detector. These monitors each consists of a 1.27 cm diameter by 1.27 cm thick plastic scintillator cylinder and a 0.5 inch photomultiplier tube. Figure 2.1.6 shows a photograph of parts of HEXTE with the particle monitor in the lower right corner. The monitors are shielded by aluminum, providing a threshold energy of around 0.5 MeV for electrons. The monitors remain of course fully functional at all time, especially also during SAA passages. This allows us to use data taken by these detectors to measure the SAA in

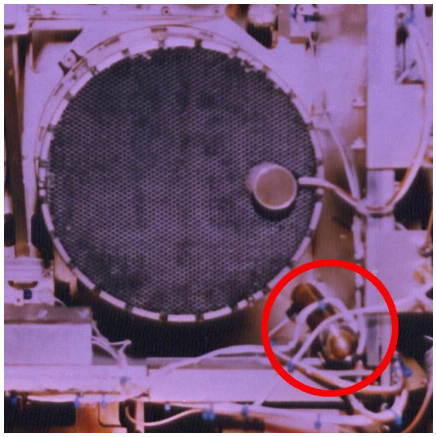

Figure 2.1.6: Photograph of HEXTE, particle monitor in the red circle in the lower right.

detail. For more information about HEXTE see Chapter 5 of the technical appendix F (Swank, 2007) or Rothschild et al. (1998).

As stated above, HEXTE is turned off in the SAA region and no science telemetry data is transmitted. However, the housekeeping data, containing the data from the particle background monitors, are sent back to Earth. These data are taken in 16 s intervals and exists from January 1996 onwards. We regarded data up to January 2008. These facts lead to the point that we have detailed background radiation measurements of the whole *RXTE* orbit for more than 12 years. This is one of the best statistics of radiation environment in this region and the SAA investigated up to date.

2.2 Measuring the SAA with *RXTE*

2.2.1 Mapping the SAA

In order to study the shape and location of the SAA, averaged particle flux maps were calculated with a time resolution of 3 months and a spatial resolution of 0.25 deg in longitude, 0.5 deg in latitude, and 10 km in altitude. To construct these maps we compared the time-stamps of the housekeeping data with the time in the orbit ephemeris files. As the time resolution of the ephemeris files is only 60 sec, we extrapolate the actual position using the last measured speed of the satellite. The projected location on the Earth is then rebinned into 0.25 degrees in longitude and 0.5 degrees in latitude bins. For these bins an average count rate for three months is calculated. The chosen

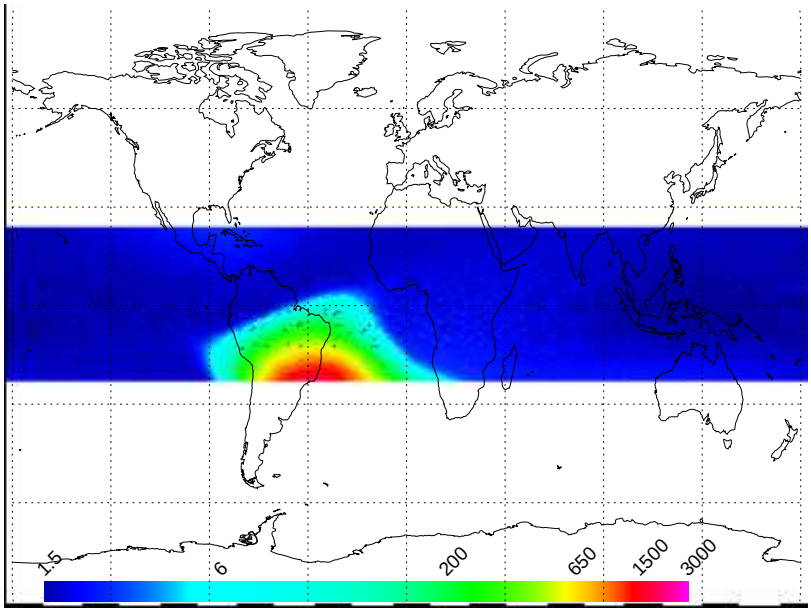

Figure 2.2.7: Maps of the average count rate of the particle monitor of *HEXTE B* in 1997, 1st quarter, altitude 570–579 km.

grid spacing is a compromise between the desire to obtain a good spatial resolution and a good signal to noise ratio in the resulting maps. On average, for each map each bin is visited ∼1.5×, although this is a strong function of latitude. In the southernmost latitude bins, where the center of the SAA is situated, each bin represents the average of at least 6 measurements taken in this latitude-longitude-altitude bin. Figure 2.2.7 and 2.2.8 shows two examples for the generated maps which show the countrate projected on the Earth. We have chosen the years 1997 and 2003 as examples as they provide good statistics and show the typical change of the SAA over the years.

As discussed in Sect. 2.1.3, atmospheric drag causes the satellite to constantly loose altitude. This leads to the fact that the highest altitudes are only measured in the first few years, while lower altitudes are only measured more recently. To indicate this change, in this paper the different colors and symbols indicated in Table 2.2.1 are used in all plots displaying the time dependence of an SAA related quantity.

2.2.2 Describing the Shape of the SAA

Due to the 23° inclination of *RXTE*'s orbit, the satellite does not pass through the location of the lowest B-field, i.e., the center of the SAA. *RXTE* does move southward

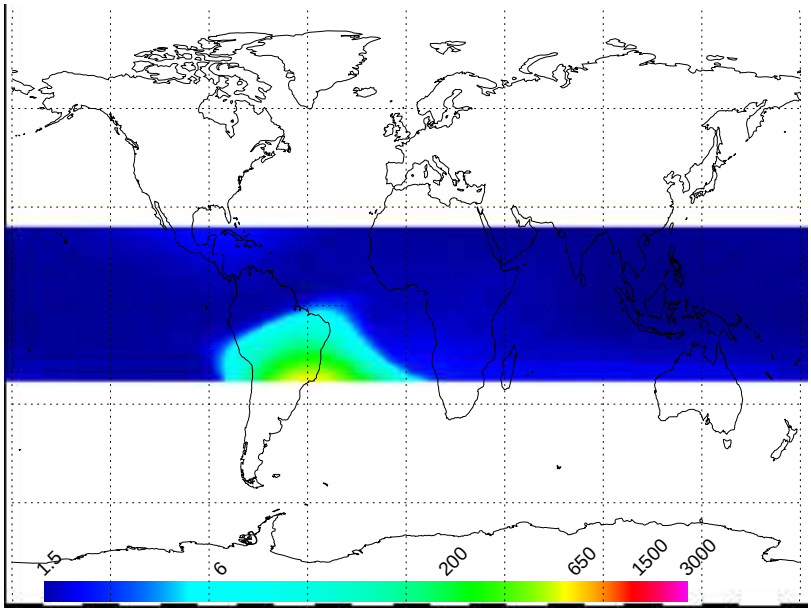

Figure 2.2.8: Same as Fig. 2.2.7 but for 2003, 3rd quarter,altitude 500–509 km.

Table 2.2.1: Symbols and colors used in the plots. The last column gives the time-bins in years for which data for that specific altitude are available. Time-bins are 3 months in duration each.

Symbol	**color**	**Altitude** (km)	**Time-Bins**
cross (+)	red	580–589	1996.00–1999.50
asterisk (∗)	orange	570–579	1996.00–2000.25
diamond (⋄)	yellow	560–569	1996.00–2001.00
triangle (△)	light green	550–559	1999.50–2001.75
square (□)	dark green	540–549	2000.50–2002.00
times (×)	turquoise	530–539	2001.25–2002.75
cross (+)	light blue	520–529	2001.75–2003.25
asterisk (∗)	azure	510–519	2002.25–2004.50
diamond (⋄)	dark blue	500–509	2002.75–2006.25
triangle (△)	violet	490–499	2003.75–2007.75

enough however, to allow us to obtain meaningful results for the strength and position of the feature. The best results are consequently obtained, when concentrating on the southernmost tracks of *RXTE*. For this reason we base our analysis on the HEXTE particle monitor count rate measured in the southernmost and on the average of the rate in the 11 southernmost latitude bins.

The distribution of particle flux with longitude has traditionally been described using

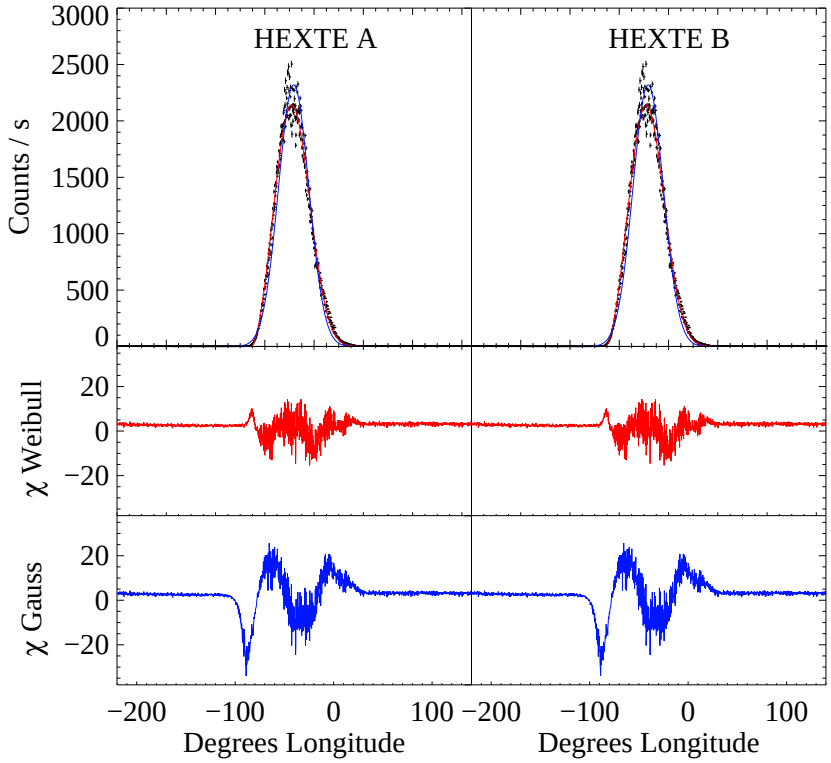

Figure 2.2.9: Simultaneous fit of HEXTE A and B monitor for 1997, 1st quarter, altitude 570 – 579 km, latitude −23° south. The Weibull function is shown in red, the Gaussian function in blue. The residuals are shown in the corresponding colors below the main plot.

Gaussian functions (e.g., Konradi et al., 1994; Bühler et al., 1996, and references therein), with the peak of the Gaussian describing the position of the SAA and its width being a measure for its size. A closer inspection of the particle monitor rates along one latitude bin, however, reveals that the SAA is distinctly asymmetric in shape (see, e.g., Fig. 2.2.9). An asymmetric function is thus better suited to model the overall longitude-dependent particle flux. Numerical experimenting revealed that for all measurements described here, a Weibull function defined by

$$y = \begin{cases} A \cdot \lambda \cdot \left(\frac{x-\theta}{k}\right)^{k-1} \cdot \exp\left(-\left(\frac{x-\theta}{\lambda}\right)^{k}\right) & \text{for } x \geq \theta \\ 0 & \text{for } x < \theta \end{cases} \tag{2.11}$$

gives a significantly better description of the shape of the SAA in terms of the χ^2-value of the fits. Here, A is the normalization, λ the scale parameter, θ the shift parameter and k the shape parameter of the Weibull function. The position of the maximum of

the Weibull function, x, is

$$x = \lambda \cdot \left(\frac{k-1}{k} \right)^{\frac{1}{k}} + \theta \tag{2.12}$$

and the variance of this distribution, σ^2_{wei}, is given by

$$\sigma^2_{\text{wei}} = \lambda^2 \cdot \Gamma \left(1 + \frac{2}{k} \right) - \mu^2 \tag{2.13}$$

Figure 2.2.9 compares the Weibull fits to data from early in the missions with fits where a simple Gaussian function was employed for $b = 23°$ latitude band, illustrating that the Weibull function is a better description for this measurement. We note that for later times, during the solar maximum, the SAA shape becomes more symmetric. During that time interval, Gaussians describe the shape almost as well as the Weibull function. Even during that interval, however, the χ^2-values of the Weibull fits show that this function still describes the SAA shape significantly better than a Gaussian. The variation in the shape of the SAA is relatively small, so that it looks almost the same throughout the years. In the following, we will therefore only present results from the Weibull fits. We note, however, that the main results shown here are independent of the specific fit function used and only differ in minor details.

Finally, we note that the count rates from the monitor of HEXTE A and of HEXTE B do show very similar behavior, with the only difference being that HEXTE A's rates are typically 2% larger than HEXTE B's rates (Fig. 2.2.9). We therefore modeled data from both detectors simultaneously, taking this difference in count rate into account by introducing a flux normalization constant in all fits and keeping all other parameters describing the shape of the SAA the same for both detectors.

Even though some properties of the SAA are changing with altitude (see, for example, Ginet et al., 2006), the movement of the SAA's location is independent of altitude (Grigoryan et al., 2005), as is also confirmed by our results presented below (Sect. 2.3.3).

2.3 Results: Evolution of the SAA 1996–2007

2.3.1 Temporal variation of the Particle Flux

As noted above, the shape of the SAA does not change considerably with time. The absolute count rate on the other hand does change dramatically. To take a closer look at this variation we used the normalization factor of the Weibull fit (see Fig. 2.3.10) as a measure for the power of the SAA and the variance of the fit (see

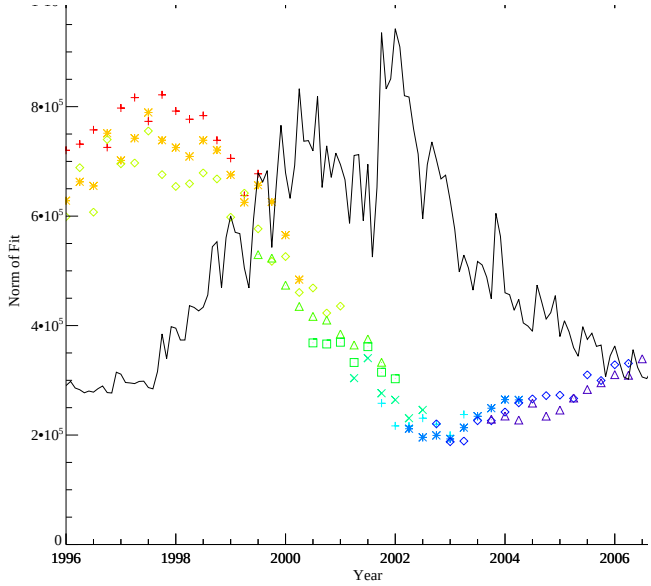

Figure 2.3.10: Norm of Weibull. The black line shows the 10.7 cm flux scaled to the left y-axis. The color code is explained in tab. 2.2.1.

Fig. 2.3.11) as a measure for the size of the SAA and plotted these values as function of time. The time resolution is quarter a year, as were the maps (see Sect. 2.2.1).

Huston et al. (1996) and Dachev et al. (1999) have shown that the SAA varies inversely correlated with the solar activity. These papers explain this behavior through the heating of the atmosphere with higher solar activity. This leads to a higher neutral density in the altitude region of the satellite and consequently to a higher absorption of trapped particles. So fewer particles mirror below or at the altitude of the satellite and thus the particle flux is reduced compared to times with less solar activity. To investigate the relation, we plotted on the second y-axis of Figs. 2.3.10, 2.3.11, 2.3.13, 2.3.14 the observed solar 10.7 cm radio flux in $10^{-22}\,\mathrm{W\,m^{-2}\,Hz^{-1}}$ as a gauge of solar activity. We used data provided by the National Geophysics Data Center (*NGDC*)[2]. The data are provided as monthly average. We used the directly observed flux as it is a good measure for the influence of the sun on our atmosphere. This flux changes not only with solar activity but according to the distance of the Earth to the sun over the year. It can be clearly seen, that there is a definite correlation between solar activity and the power of the SAA (Fig. 2.3.10).

[2]http://www.ngdc.noaa.gov/

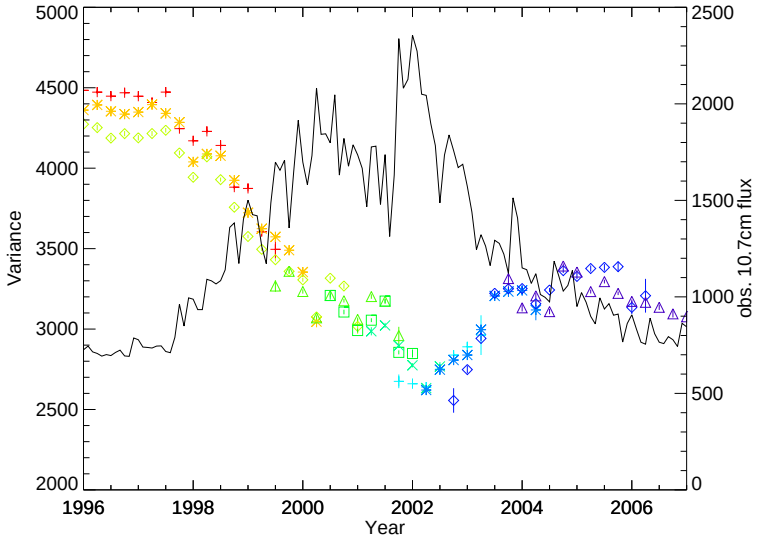

Figure 2.3.11: Same as Fig. 2.3.10, but for the variance of Weibull.

Huston et al. (1996) have also shown that there is a time lag between the 10.7 cm flux from the sun and the measured proton flux. This time lag can be clearly seen when plotting the maximum value of the fitted Weibull function against the solar 10.7 cm flux (Fig. 2.3.12). If there would be no time lag, this plot should show a perfect circle, as the both rates are anticorrelated. The datapoints in Fig. 2.3.12 are apparently arranged as an ellipse and thus a time-lag is evident. We have data for about 12 years, which means it covers more than one 11-year solar cycle. We have thus datapoints to every stage of solar activity. This fact is mirrored in Fig. 2.3.12 as the ellipse is almost. To calculate the time lag we used a cross-correlation function and found a minimal correlation of about -0.75 at a shift of exactly 1 year. This is in accordance with the results of Huston et al. (1996) for the proton flux.

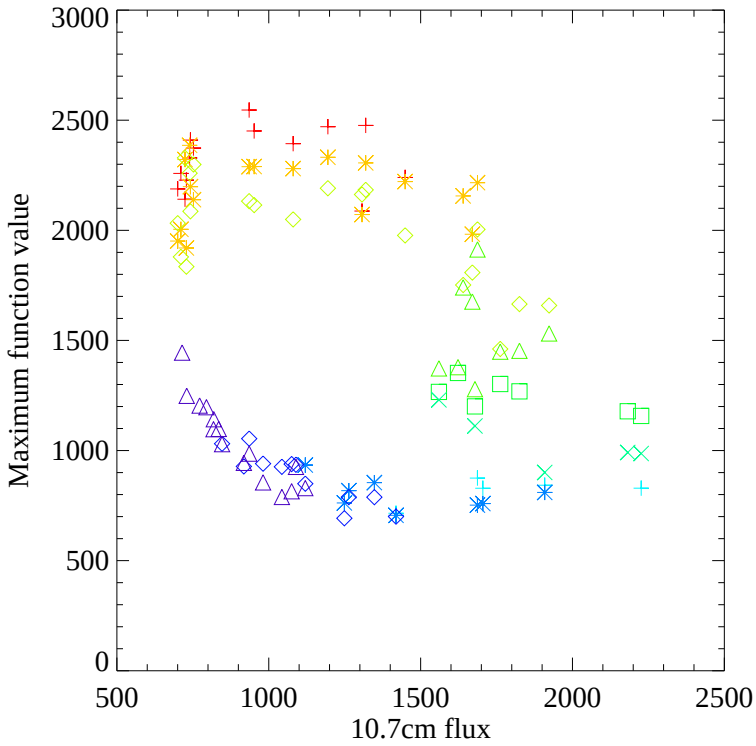

Figure 2.3.12: The maximum value of the Weibull fit plotted against the 10.7 cm flux. The color code used is described in table 2.2.1 and represents the altitudes bins and thus indirectly the time.

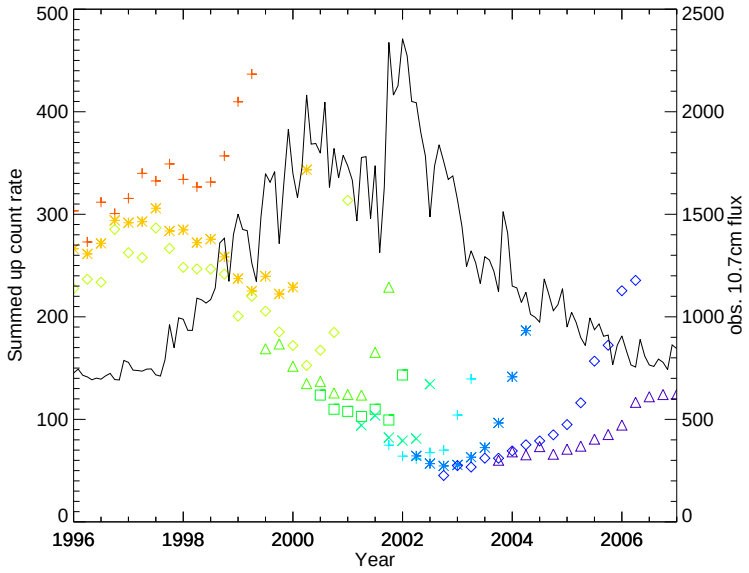

Figure 2.3.13: Averaged summed up count rate of both detectors from longitudes $-80°$ to $+40°$ and latitudes from $0°$ to $-23°$. Black line is the observed 10.7 cm flux.

2.3.2 Temporal variation of the overall count rate

Bühler et al. (1996) investigated the relation between solar activity and the power of the SAA, too. To find the power of the SAA they did not use a fitted function but the overall count rate as a function of time in a rectangle ranging from longitudes 80° west to 40° east and over all latitudes south of the equator. Figure 2.3.13 shows this analysis for our data of the HEXTE particle monitor. We used the total count rate from both HEXTE A and B to minimize noise and statistical errors. As can be seen, the correlation of this analysis with the solar 10.7 cm flux is far worse than the correlation between the radio flux and the values of the fitted functions (Fig. 2.3.10). The worse correlation can be ascribed to the fact that *RXTE* is a bit closer to the Earth in more northern regions of its orbit than in the more southern. As the satellite looses altitude, the later timebins for a given altitude bin contain almost only data from the southernmost latitudes, i.e., where the SAA is located. This leads to a increased average count rate which works against the solar cycle.

To reduce the effect of the satellite orbit, we used a considerably smaller rectangle, especially regarding only the southernmost latitudes. Our new rectangle is ranging from longitudes 70° west to 20° west and from latitudes 23° south to 19° south. The average count rates are of course drastically increased, as our rectangle now only

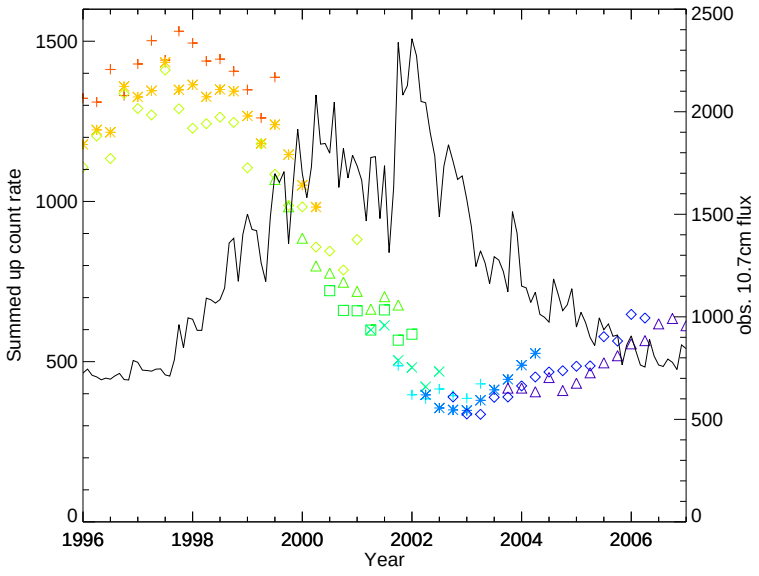

Figure 2.3.14: Averaged summed up count rate of both detectors from longitudes $-70°$ to $-20°$ and latitudes from $-19°$ to $-23°$. Black line is the observed 10.7 cm flux.

consists of the most active area. As expected, this leads to a better correlation (Fig. 2.3.14), which is in perfect accordance to the one found from the fit parameters (see Fig. 2.3.10 and 2.3.11). This shows clearly that the fits and there parameters model the particle background very well.

2.3.3 Movement of the location

To determine the temporal movement of the SAA we calculated the position of the maximum of the Weibull fits for the southernmost latitude (Fig. 2.3.15). A linear fit to the position for the maximum leads to a slope of $0.248 \pm 0.003\,\mathrm{deg\,year^{-1}}$, which is in good agreement with results of other groups. A straight with that is superimposed in Fig. 2.3.15. But obviously the SAA is not moving as smoothly as expected. In Fig. 2.3.15, a strong change in the position of the SAA is clearly visible between 2003 and 2004. This change is in the opposite direction of the usual movement. We can rule out a strange behavior of the Weibull fit, as the Gaussian is showing exactly the same feature, see Fig. 2.3.16. The slope of the best-fitting linear function for the Gaussian movement is $0.412(1)\,\mathrm{deg\,year^{-1}}$ and its graph is overplotted in Fig. 2.3.16.

To further investigate this behavior, we averaged the maximum position of the Weibull

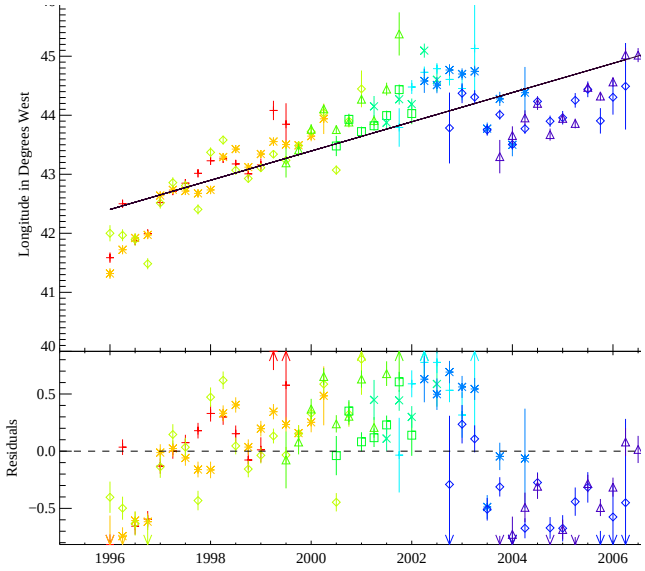

Figure 2.3.15: Position of the maximum of the Weibull Fit for lat $-23°$. Superposed a linear fit over all data, with slope of $0.248(3)\,\mathrm{deg\,year^{-1}}$. The second panel shows the residuals of the fit.

fits over the 11 southernmost latitude bins. This helps to reduced the noise and rule out artefacts in the southernmost latitude bin. In all 11 bins the shape is very similar and they are still close to the center of the SAA. Fig. 2.3.17 shows that the averaged position shows same behavior as the position for latitude 23 deg south only. This means that the sudden change between 2003 and 2004 is a persistent feature and not depending on the latitude. The superposed linear fit corresponds to a movement rate of $0.290 \pm 0.002\,\mathrm{deg\,year^{-1}}$. Regarding the χ^2-values, the quality of the fits has not changed much during the whole time. Especially it does not show any strange behavior between 2003 and 2004, as shown in Fig. 2.3.18. This result further hardens the fact that the feature is real. At the end of every altitude bin, the χ^2-values decreases dramatically. This is due to the fact that at the end of a bin only very few measurements are taken at that altitude, increasing the errors and thus decreasing χ^2.

An alternative way to determine the center of the SAA is not to use the maximum (mode) of the Weibull fits, but the mean (expectation value). We investigated the data in the same way as with the mode. Again, the behavior is very similar, leading to movement rates of $0.291 \pm 0.003\,\mathrm{deg\,year^{-1}}$ for the single latitude bin and $0.312 \pm 0.001\,\mathrm{deg\,year^{-1}}$ for the average over 11 latitude bins. These data also show

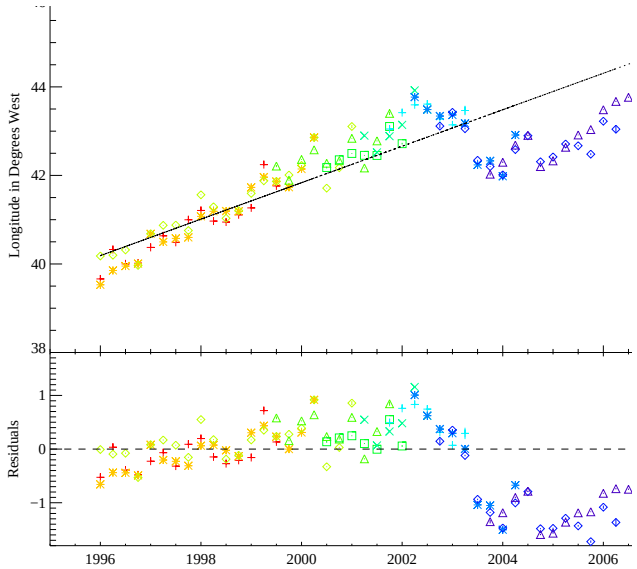

Figure 2.3.16: Same as 2.3.15 but for the position of the maximum of the Gaussian Fit. The superposed linear fit features a slope of $0.412(1)\,\mathrm{deg\,year}^{-1}$.

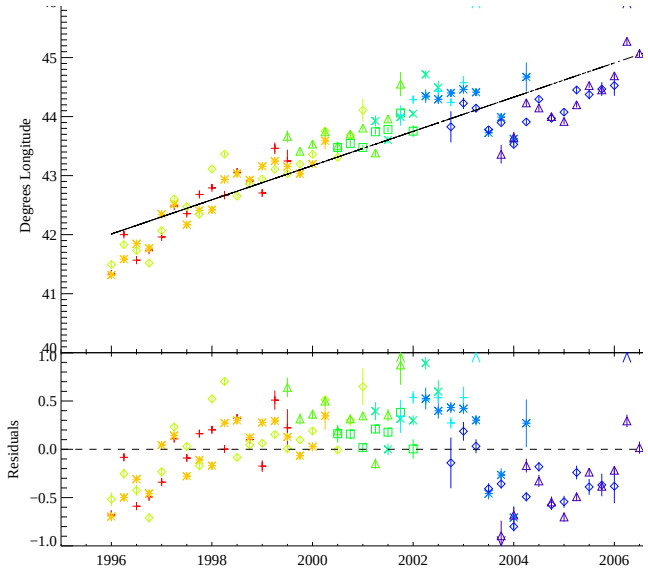

Figure 2.3.17: Average position of the maximum of the Weibull Fits for lat $-23°$ to $-18°$. Superposed a linear fit over all data, with slope of $0.290(2)\,\mathrm{deg\,year}^{-1}$.

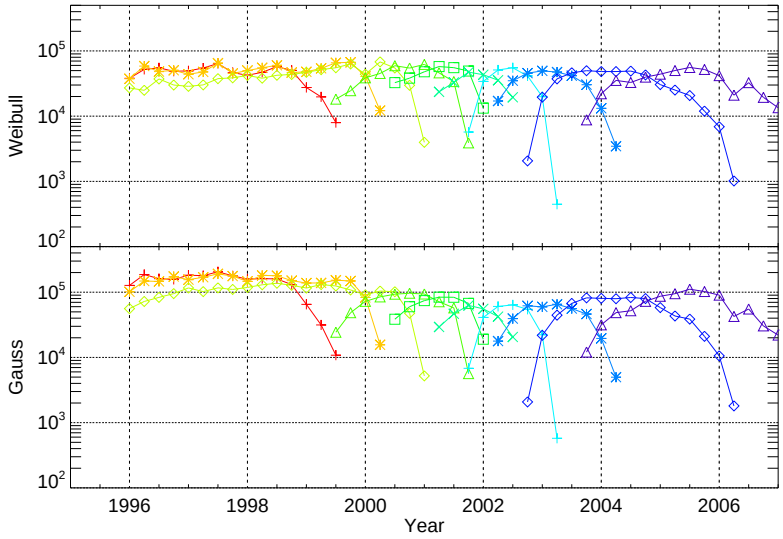

Figure 2.3.18: χ^2 values of the Weibull (top) and Gaussian (bottom) fit.

Table 2.3.2: The slope of all single straight line fits to the different kinds of data

Kind of data	**Slope in deg year^{-1}**
Mode, single lat	0.248 ± 0.003 deg year^{-1}
Mode Gaussian, single lat	0.412 ± 0.001 deg year^{-1}
Mode, multiple lats	0.290 ± 0.002 deg year^{-1}.
Mean, single lat	0.291 ± 0.003 deg year^{-1}
Mean, multiple lats	0.312 ± 0.001 deg year^{-1}

a significant jump between 2003 and 2004. Table 2.3.2 summarizes the results from all different simple straight fits.

As seen above a simple linear fit is not a good approximation to the movement of the SAA due to the sudden change in the movement. Therefore we added 6 additional degrees of freedom to the linear fit by allowing the fitparameters to change at two different points. We found, that a minimal χ^2 is reached, when the fitparameters change at 1998.25 and at 2003.25. The 2003.25 point was expected, but the one at 1998.25 is not quite so clearly visible. Nonetheless, the χ^2 improves by 487.02 from 2527.8 to 2040.78 when added to the averaged maximum value of the Weibull fit. In Fig. 2.3.19 we show these values and the superposed straights. The slopes of the straights and their errors are shown in table 2.3.3. To check the reasonability of the second break point of the linear fit, we used the F-test routine provided by X-SPEC.

Table 2.3.3: Slopes of the three independent fits in Fig. 2.3.19.

Years	**Slope in deg year^{-1}**
1995.00–1998.25	0.656 ± 0.011
1998.50–2003.25	0.346 ± 0.005
2003.50–2007.00	0.467 ± 0.012

We found a very low probability value of $4.065 \cdot 10^{-06}$, which means that the relevance of this second point is very high. We are aware of the fact, that the F-test might not be the correct statistical method to investigate this improvement, but nonetheless it gives a good hint to the quality of it.

We conclude, that a sudden change in the movement of the SAA is not rare, only the strength of the 2003.25-feature seems to be special. Obviously a sudden change means, that the SAA moves every few years very fast eastwards, in third quarter of 2003 as much as about 0.8 deg. Additionally the rate of the movement varies after every single discontinuity. The commonly stated rate of 0.3 deg year^{-1} seems to be only valid on longer timescales. On shorter timescales, the rate can differ drastically from this value. Fits for the other ways shown to determine the maximum of the SAA, like using the mean of the fits, lead to the same time-bins for the break points.

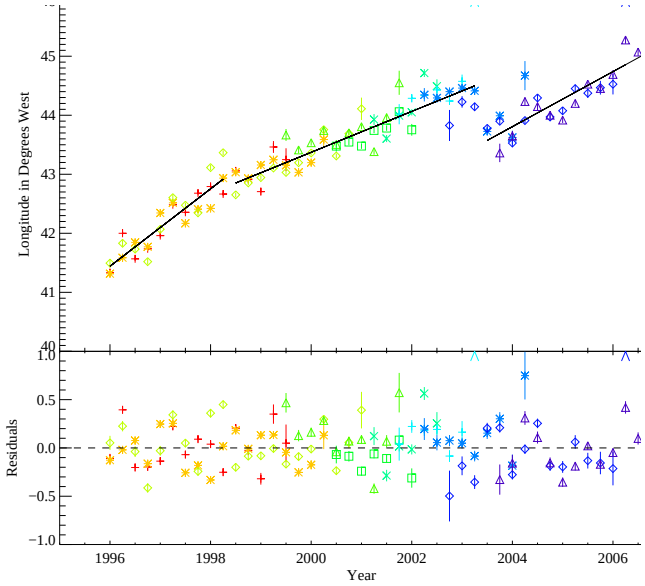

Figure 2.3.19: Average position of the maximum of the Weibull Fits for lat −23° to −18°. Superposed three linear fits, with slope of 0.65(1) deg year^{-1} (1996.0–1998.25), 0.346(5) deg year^{-1} (1996.5–2003.25) and 0.46(1) deg year^{-1} (2003.5–2007.0).

2.4 Summary and conclusion

USING the particle monitor aboard *RXTE* allowed us to look at almost 12 years of constantly taken data of the radiation background in low earth orbits. Even if we can not measure the energy, we get a good picture of shape and position of the SAA. We made maps of the particle environment of *RXTE*, showing the SAA and its temporal behavior very clearly. We have shown that the shape of the SAA along one latitude can be fitted quite well using a Weibull distribution. These fits show a clear anti-correlation between the 10.7 cm solar flux and the intensity and size of the SAA. Additionally, the correlation shows a time lag which could be calculated to be about 1 year. The large time range of our data allowed us to monitor the SAA for one solar cycle and we could show, that after approximately 11 years the SAA has about the same size and power again. Additionally we could measure the location of the maximum and the mean of the fit and follow it through time on a quarter a year resolution. This shows a westward drift of the SAA, with a rate between 0.248 and 0.312 deg year^{-1} for the Weibull-fits. These values are in good agreement to previous work. But in contrary to a smooth movement, the drift rate is not constant, but

shows two irregularities, meaning that its position shifts slightly a little eastward and then continues to move westwards. These break points are in the fist quarter of 1998 and in the second quarter of 2003, where the latter one is distinctly stronger than the first one. These irregularities could indicate a change in the particle population of the SAA. This could happen during huge "coronal mass ejections" (CME) from the sun. These mass ejections can cause geomagnetic storms (Brueckner et al., 1998) and inject electrons and protons into the atmosphere. Asikainen & Mursula (2005) have shown, that during the great storm of March 21, 2001 electrons became trapped in the SAA and drifted around the Earth together with the SAA. In 2003 there was a major CME which resulted in a intense geomagnetic storm, investigated by Becker-Guedes et al. (2007). This event took place November 2003. Regarding our data it is clearly seen the sudden movement change occurred in the beginning of 2003. Furthermore the injected electrons that were seen in 2001 decay with a lifetime of about 8 hours (Asikainen & Mursula, 2005), while the feature seen in the SAA has a longer lasting influence. These facts make it highly unlikely that CMEs are responsible for the measured irregularities. As CME are the most prominent outside source which disturbs the geomagnetic field and the particle population around the Earth, it is more likely that the origin for the changes in the movement is in the interior of the Earth. The main magnetic field of the Earth is produced by dynamic currents in the outer core so irregular changes are not unexpected. This can be seen for example in the secular variation, i.e., the changes of magnetic field with time. From time to time, a abrupt change in the secular variation is measured, which is called a "geomagnetic jerk". These jerks occur when the fluid flows on the core surface change. For the underlying physical processes refer to Wardinski et al. (2008) and references therein. The jerks are found in geomagnetic data of the last century when regarding the time derivative of the east-component of the magnetic field. Recently Olsen & Mandea (2007a) found another jerk in the beginning of 2003. This jerk might have even an influence on the drift of the north magnetic dip pole, which accelerated for over 10 years but started to decelerate in 2003 (Olsen & Mandea, 2007b). This shows that this jerk had a major influence on the magnetic field of the Earth. We think, that it could also influence the location of the SAA as this location depends strongly onto the magnetic field. Jerks are defined as sudden changes in the secular variation, which means, they do have a long lasting effect onto the geomagnetic field. This agrees well with our data, as a sudden disruption causes a persistend change in the location of the SAA. The connection between jerks and irregularities in the movement of the SAA is further backuped as Mandea et al. (2000) have found a geomagnetic jerk around 1999, which conforms with the second break point we have found in our data at the end of 1998. This breakpoint was not so pronounced as the one in 2003, which agrees with the fact that the 1999 jerk seems not to have such a great influence on the magnetic field as the one in 2003. To determine the beginning and end of the feature in the movement more precisely, we extracted the data again with a higher temporal resolution of 1 month. It was necessary to average over all altitudes to retain a good signal to noise ratio. But as seen in Fig. 2.3.16 the position of the maximum of

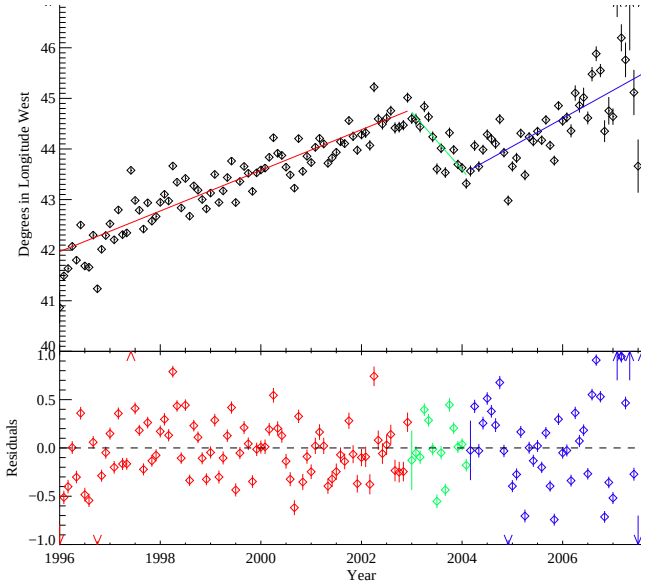

Figure 2.4.20: Position of the maximum of the Weibull Fit for lat −23°. Superposed three linear fits, with slope of $0.40(4)\,\mathrm{deg\,year^{-1}}$ (1996.0–2003.1), $-1.13(9)\,\mathrm{deg\,year^{-1}}$ (2003.2–2004.4) and $0.55(2)\,\mathrm{deg\,year^{-1}}$ (2004.5–2007.0). The second panel shows the residuals of the fit, the colors according to the three parts of the fit.

the SAA does not, or only slightly, depend on the altitude. Figure 2.4.20 shows the position of the maximum of the Weibull fit with a temporal resolution of 1 month. Superposed is again a linear fit, which allows the slope to change at two different points. The points were fitted to be in February 2003 and in April 2004. This means, the SAA region was moving against its usual movement for a bit more than 1 year. The movement rate was quite fast with about $1.14 \pm 0.094\,\mathrm{deg\ year^{-1}}$ eastwards. The feature in 1999, which was found in the altitude dependend data, is still seen weakly in the high time resolution data. But the backwards drift was distinctly shorter than the one in 2003 and thus we can not determine its duration, even in the new data. We did not include it in Fig. 2.4.20 as it does not change the features of the 2003 jerk. We do not know of any jerk or other magnetic distorsion which took place in the beginning of 2004 to account for the resuming of the westward drift of the SAA. Nonetheless the eastward drift is very likely to be connected to the jerk in 2003 and the duration of the eastward movement is just showing the slow response of the trapped particles in the atmosphere.

Still further investigations are necessary to analyze the connection between the jerks

and the location of the SAA. One very interesting satellites in orbit is the satellite for "Detection of Electro-Magnetic Emissions Transmitted from Earthquake Regions" (*DEMETER*), which was launched in 2004. Thus *DEMETER* could not measure the 2003 geomagnetic jerks and its influences on the trapped radiation. Sauvaud et al. (2008) published a very detailed map of the particle background in 700 km altitude, with the SAA clearly visible. Hopefully *DEMETER* is continuing to operate smoothly so that longterm studies are made possible. Additionally other X-ray satellites which are already in orbit should provide independent measurements of the particle background on a long timescale. To use other X-ray satellites is additionally intriguing, as they do posses different orbits. For example the International Gamma-Ray Astrophysics Laboratory (*INTEGRAL*) is on a very eccentric orbit and could provide good data about the outer radiation belts. Thus not only the near-Earth environment, but the whole radiation belts can be investigated.

The diversity of the phenomena of nature is so great, and the treasures hidden in the heavens so rich, precisely in order that the human mind shall never be lacking in fresh nourishment.

(Johannes Kepler)

3 Vela X-1

Contents

3.1 About neutron stars and orbits

3.1.1 Neutron stars

In the beginning of the 20th century there was a long discussion about what will happen when a star has burned all its nuclear fuel and the thermal pressure forces are no longer available to sustain the gravitational pressure. Fowler (1926) showed that then these stars will contract further to compact objects called white dwarfs. White dwarfs are stars in which the gravitational forces are equalized by the pressure

of the degenerate electron gas due to the Pauli exclusion principle. These objects have to be very compact, with a radius of a few 1000 km to have a large enough degenerate electron gas pressure. But Lev Landau and Subrahmanyan Chandrasekhar independently showed that this is only possible for stars which are not too massive. Chandrasekhar (1931) calculated the critical mass to be about $M = 1.44 M_{\odot}$, the so-called Chandrasekhar limit. Above this mass, the star will collapse further and become a neutron star. One possible scenario where a neutron star can be the end of stallar evolution is the evolution of a 15 solar mass ($M_{\odot}$) star (see Karttunen et al., 2007). The massive star will evolve quickly through the main sequence up to the giant phase. There it will burn all its nuclear fuel sources up to iron and at the end explode as a supernova. While the outer layers of the star are ejected the core will be compressed. If the mass of the remaining core is larger than the Chandrasekar limit the core will contract to a neutron star. When contracting under the immense gravitational force protons and electrons are then fusioned together to form neutrons under the release of neutrinos via inverse β decay. The pressure of the degenerate neutron gas is then able to withstand the gravitational force and the star will reach a stable state as a neutron star. As neutrons are fermions, the pressure of the degenerate neutron gas comes directly from the Pauli exclusion principle. The density of a neutron star is then about $10^{15}\,\mathrm{g\,cm^{-3}}$ and the radius will be about 10 km. But even this pressure is not high enough to withstand the graviational forces above the so called Oppenheimer-Volkov-Mass. The star will contract further and become a Black Hole. The exact value of the Oppenheimer-Volkov-Mass is not known but is something between 2 and 3 solar masses. For more detailed explanation of stellar evolution see Iben (1991), Iben et al. (1995) and references therein. If neutron stars would purely radiate as black bodies, we would not be able to detect them with modern telescopes. If we take typical values of a neutron star with $R = 10\,\mathrm{km}$ and $T = 10^6\,\mathrm{K}$ it would have a absolut optical magnitude of 19.7 mag. This would allow us to detect these objects only in about 100 pc distance. Compared to a the diamater of the Milky Way, which is about 30 000 pc, this is only our nearest neighbourhood. But fortunately there is another process which allows to release great amounts of energy: accretion. When mass falls onto a neutron star, its kinetic energy can be directly converted to radiation. From energy conservation it follows that the luminosity is about

$$L = \dot{M}\frac{GM_x}{R_x} = \eta \dot{M} c^2 \tag{3.1}$$

where G is the gravitational constant, M_x the mass of the neutron star, $\dot{M}$ the infalling mass rate, and R_x the radius of the neutron star. The accretion efficiency η is about 10%. This means that accretion is the most effective process in the universe. If we suppose that the neutron star is accreting about $\dot{M} = 10^{-8} M_{\odot}\,\mathrm{year}^{-1}$ and 10% are converted to energy, a luminosity of about $10^5 L_{\odot}$ is obtained. This huge amount of energy is carried away most effectivily in X-rays. The calculation is done in more detail in Lipunov (1992). To accrete enough mass, it is necessary, that the neutron star is in the vicinity of another, normal star. This is the case in binary systems.

3.1.2 Binary systems

In a binary system the evolution of the stars will be different compared to the one described above for single stars. Binary systems are one of the most interesting stellar systems in the sky as they show very unique and unexpected features. To delve deeper into the description of such binaries is beyond the scope of this work. Here I will describe only one possible scenario which would lead to a system like Vela X-1. To understand the processes which happen in a binary system it is meaningful to use the Roche model (see, e.g., Hilditch, 2001). This model describes the potential of two mass points in a corotating frame. It is assumed that the orbits are circular. The potential Φ of two masses m_1 and m_2 which a third body with infinitesimal mass would experience is given by the two point-mass potentials and the rotational potential:

$$\Phi = -\frac{Gm_1}{r_1} - \frac{Gm_2}{r_2} - \frac{\omega^2}{2}\left[\left(x - \frac{m^2}{m_1 + m_2}\right)^2 + y^2\right] \tag{3.2}$$

We can then calculate the equipotential surfaces in the corotating frame, which only depend on the distance $|m_1 - m_2|$ between the two masses and the ratio m_1/m_2 of the two masses. Figure 3.1.1 shows the Roche potential of two masses with a mass ratio of 2. The lines show the equipotential surfaces. Of course the surfaces of stars are surfaces of constant pontential, too. This is why the Roche model is so useful, because when the stars expand their surface they will always be shaped like the equipotential surfaces of the Roche model. The inner thicker plotted line in Fig. 3.1.1, shaped light a 8, is the maximal distance where mass is bound gravitationally to one of the stars. This means that when a star grows larger than this surface it will start to lose mass. A very important point is the point marked L1 in Fig. 3.1.1, the so-called inner Lagrangain point. Mass will flow from one star to the other through this point, in a process called Roche lobe overflow. More about the mathematics of the Roche system is found in Hilditch (2001).

The evolution of a system like Vela X-1, consisting of an early type supergiant and an old and evolved neutron star is described in a thorough way by van den Heuvel (1995). I will give a short description of the evolution here to get an overview of the physical properties of the system. In the early days of its life a system like Vela X-1 might have consisted of two main-squence stars, with one being more massive than the other. Let us call the more massive star star A, the lighter star B. Star A will evolve faster than star B because of its higher mass. When star A leaves the main-sequence and becomes a red giant it will grow very rapidly and fill out its Roche lobe. This is only the case in close systems with an initial orbital period of about 100 days. Due to the mass-transfer star A will soon be less massive then star B. Nonetheless it is further evolved and will explode in a supernova Type II first. Chances are good that the system is not destroyed in this explosion because star B is now more massive. As with a single

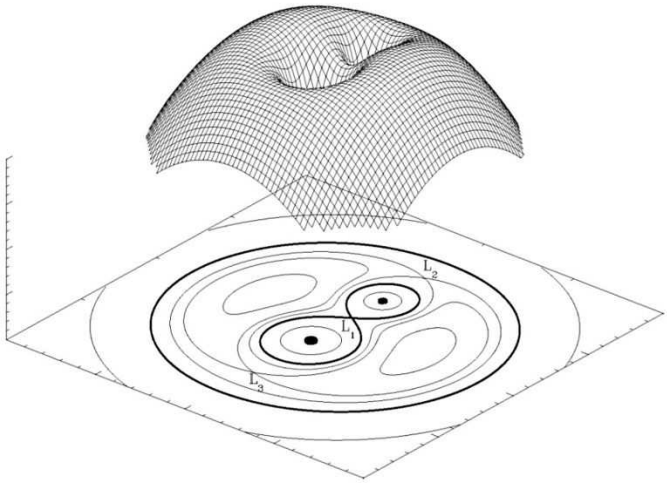

Figure 3.1.1: Three-dimensional represenation of the Roche potential of two masses with a mass ratio of 2. (from http://en.wikipedia.org/wiki/Image:RochePotential.jpg)

star, when the core of star A is massiv enough, it will collapse to a neutron star. In this state it is expected to see a radio pulsar with an unevolved main-sequence star as companion. Such systems were discovered, e.g. PSRB1259−63 (Johnston et al., 1992). When star B evolves it might exhibit a strong stellar wind. These winds can be accreted by the neutron star and transformed into X-rays. Depending on the distance between the two stars, we will see a brighter or a dimmer source as the density of the wind is decreasing quadratically with the distance from star B. Another possibility, as mentioned by Karttunen et al. (2007) is that star A does not go supernova, but contracts silently to a white dwarf, because it lost most of its mass to star B. When star B evolves it will transfer mass via Roche-lobe overflow to the white dwarf, which will show nova bursts. Some of the mass will be accreted on the white dwarf and it might eveantually reach the Chandrasekar limit. It will then explode in a type I supernova and the core could again remain as a neutron star.

Even the violent processes that lead to the creation of neutron stars can not violate the laws of physics. These laws require, among others, the conservation of the magnetic flux and the angular momentum. As the star contracts from a radius R_* of about 10^6 km to a radius $R_{\rm NS}$ of 10 km, the rotation speed and the magnetic field must increase by many decades. After the collapse the angular momentum $J = mr^2\dot{\theta}$ can be changed through mass ejection and accretion. We therefore expect to observe neutron stars with a broad range of rotation speeds, from a few seconds to hours. Vela X-1 for example has a period of about 283.5 sec, but this period is changing erraticly.

The magnetic flux Φ is defined as $\Phi = 4\pi R^2 B$. This leads to $R_{\mathrm{NS}}^2 B_{\mathrm{NS}} = R_*^2 B_*$ or

$$B_{\mathrm{NS}} = B_* \left(\frac{R_*}{R_{\mathrm{NS}}} \right)^2 \tag{3.3}$$

Taking the values from above for the radii and asuming a typical stellar B-field of $B_* \approx 100\,\mathrm{G}$ this leads to

$$B_{\mathrm{NS}} = 100\,\mathrm{G} \cdot \left(\frac{10^6\,\mathrm{km}}{10\,\mathrm{km}} \right)^2 = 10^{12}\,\mathrm{G} \tag{3.4}$$

These very strong magnetic field will of course influence the matter that falls onto the neutron star. Especially as the accreted matter from the companion star is mostly ionized it will couple to the B-field and is mainly influecend by it. The magnetic field can be modelled rudely as a dipole field. This means there are two points on the surface of the neutron star where the magnetic field lines penetrate its surface (magnetic south and north pole). As the magnetic field is very strong, almost all accreted matter will be channeled via the magnetic field lines onto these points. In the developing accretion column the accreted mass will be heated up to extremly high temperatures. The points where the material finally hits the neutron star surface are called hot-spost and have an area of about $1\,\mathrm{km}^2$ (Lamb et al., 1973). It it at these very strictly localized points where the X-rays are produced. This localization explains the observed pulsations. The hot-spots are corotating with the neutron star. If they are not aligned on the rotation axis they will be obsevered in a circle in the sky like a lighthouse. If the observer is in this region a pulsating X-ray flux will be observed.

Mass and orbit determination

Before we look at the lightcurves and spectra of Vela X-1 we should familiarize ourselves with the physical parameters of a binary system. The advantage of a binary system compared to a single star is that through Kepler's laws one can find the masses of the stars (see, e.g., Karttunen et al., 2007). The orbits of the objects are determined by the gravitaional forces only. If we can measure the orbit parameters we will be able to calculate the masses. This is important for different reasons: in case of the optical companion, the mass can help us to fix the age and luminosity of the star. In case of the compact object, we can find out if it is a neutron star or a black hole. Furthermore one can check the theories on the creation of such compact objects.

To determine the masses of binary systems one must now as much as possible about the orbit of the star in space. The orbit can be regarded in two different systems, either the relative orbit or the barycentric orbit (Hilditch, 2001). The relative orbit

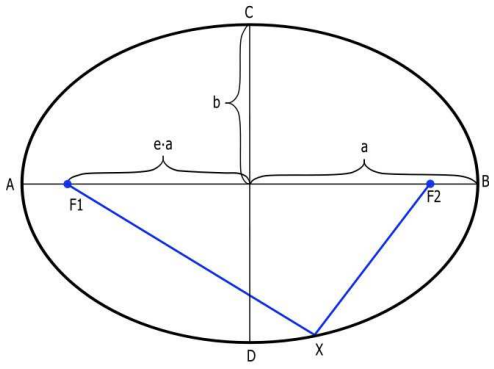

Figure 3.1.2: Example elipse (from http://en.wikipedia.org/wiki/Image:Elipse.svg)

describes the distance between the two objects. Therefore this orbit is the same when we regard the orbit of the optical companion seen from the neutron star or vice versa. This orbit is important, when studying lightcurves and eclipses. The barycentric orbit on the other hand describes the motion of the two stars from their common center of mass and is used when determining photometric velocities. To transfer the radius vectors from one system to another we can use the values $\vec{R}_x$ and $\vec{R}_o$. $\vec{R}_x$ is the radius vector of the neutron (X-rays emitting) star, while R_o is the radius vector of the optical companion, both from the center of mass. The relative orbit vector $\vec{r}$ is thus: $\vec{r} = \vec{R}_x - \vec{R}_o$. or, with help of the definition of the barycenter $m_x\vec{R}_x + m_o\vec{R}_o = 0$,

$$\vec{r} = +\frac{m_x + m_o}{m_o}\vec{R}_x \tag{3.5}$$

$$\vec{r} = -\frac{m_x + m_o}{m_x}\vec{R}_o \tag{3.6}$$

Most of the orbits of binary star systems are not circular, but elliptical. Elipses are easily described by two parameters, the eccentricity e and the length of the semimajor axis a.

As can be seen in Fig. 3.1.2, the semimajor axis a is the distance between the center of the elipse and the point, which is farest away from the center (called periastron in binary systems). The eccentricity e is the ratio of the distance between the focal point F and the center of the elipse to the semimajor axis a. This means a eccentricity of $e = 0$ describes a circle, as the focus point F is at the center. The radius vector r, i.e., the vector from one focus point to the actual location of the star is connected to the parameters of the ellipse via

$$r(t) = \frac{a\left(1 - e^2\right)}{1 + e\cos\theta(t)} \tag{3.7}$$

where θ is the angle between the semimajor axis and the radius vector, which is called

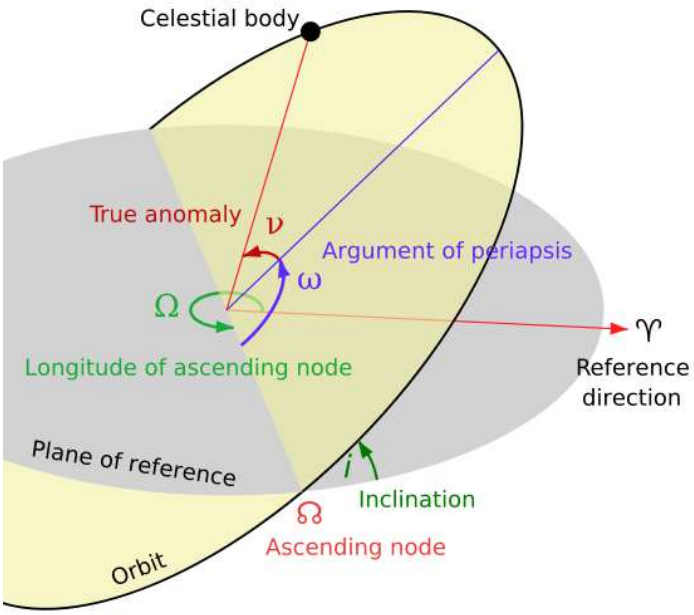

Figure 3.1.3: Parameters of an Keplerian orbit (from http://en.wikipedia.org/wiki/Image:Orbit1.svg)

true anomaly. In a binary system, θ is changing with time, and so is r, while a and e are constant in time.

To define the orientation of the orbit in space we need two more variables, namely the longitude or argument of periastron ω and the inclination i, see Fig. 3.1.3. The longitude of periastron is the angle between the ascending node Ω and the periastron, wich is the point of closest approach of the two stars. The inclination i is defined as the angel between our line of sight and the normal to the orbital plane. Stated the other way round, it is the angle between the plane of reference, which is the plane of the sky we watch and the plane of the orbit. This means that we see the system exactly from above at $i = 0°$ and edge on at $i = 90°$.

Measurements and calculations

To determine the parameters of the orbit it is enough to know the radius vector of the orbit as function of time. This vector can be obtained when the velocity profile is known. For an optically bright star, like the companion of Vela X-1, this can be done via the Doppler shift of spectral lines. Unfortunatly the inclination of the system can not be measured generally. This means only the projected velocity $v_o = v_{t,o} \sin i$ can

be measured.

For the neutron star, there is another way to determine the orbital parameters (see, e.g, Hilditch, 2001). As discussed in Sect. 3.3, the X-rays show regular pulsations. The arrival time of each pulse depends of course on the orbital phase where it was emitted. The projected distance z from the observer to the neutron star on a elliptcial orbit is

$$z(t) = r_x(t)\sin(\theta(t)+\omega)\sin i \tag{3.8}$$

The light travel time is then

$$z(t)/c = \frac{r}{c}\sin\left(\theta(t)+\omega\right)\sin i = \frac{a_x \sin i}{c}\frac{\left(1-e^2\right)\sin\left(\theta(t)+\omega\right)}{1+e\cos\theta(t)} \tag{3.9}$$

This means that the pulse arrival time of the nth pulse t_n can be calculated to

$$t_n = t_0 + nP_0 + \frac{z(t)}{c} \tag{3.10}$$

By measuring t_n and we can deduce the pulse period and $z(t)/c$ via the free parameters a_x, e and $\sin i$. These modeled parameters are just what defines the orbit of the neutron star. Combined with the parameters found for the optical companion, a complete description of the orbit as well as minimum values for both masses can be given. We can calculate now the mass of the neutron star with respect to the mass ratio of the system $q = M_x/M_\odot$.

As seen in equation 3.7, $a \propto r$, such that we can rewrite equation 3.6 for the relative semimajor-axis a as

$$a = \frac{(M_o + M_x)}{M_x}\cdot A_o \tag{3.11}$$

with A_o being the semimajor axis of the orbit of the optical companion in the center of mass system. Because of Kepler's Third Law

$$\frac{P^2}{4\pi^2} = \frac{a^3}{G\left(M_o+M_x\right)} \tag{3.12}$$

this leads to

$$M_x = \frac{A_o^3 4\pi^2}{GP^2}\frac{\left(M_o+M_x\right)^2}{M_x^2} = \frac{A_o^3 4\pi^2}{GP^2}\left(1+q\right) \tag{3.13}$$

Introducing the semiamplitude of the velocity curve K_x as

$$K_o = \frac{2\pi A_o \sin i}{P\left(1-e^2\right)^{\frac{1}{2}}} \tag{3.14}$$

equation 3.13 becomes (see Quaintrell et al., 2003)

$$M_x = \frac{K_o^3 P\left(1-e^2\right)^{\frac{3}{2}}}{2\pi G \sin^3 i}\left(1+q\right)^2 \tag{3.15}$$

Similarily we obtain for the the optical companion

$$M_o = \frac{K_x^3 P \left(1-e^2\right)^{\frac{3}{2}}}{2\pi G \sin^3 i} \left(1+\frac{1}{q}\right)^2 \tag{3.16}$$

The absolute masses can only be calculated when the inclination i is known. In the case that we have an eclipsing binary, we can constrain the possible values of the inclination. Eclipsing binary means, that the stars occult each other in our line of sight.

3.1.3 Radiation processes in neutron stars

In this section I will describe shortly how radiation and especially X-rays are produced in binary systems containing a neutron star. Only recently a huge success was made in explaining the physical processes which lead to the observed spectra by Becker & Wolff (2007, 2005). I will follow their explanation in this section. To achieve typical luminosities seen in X-ray binaries of about $L = 10^{38}\,\mathrm{erg\,s^{-1}}$ it is necessary to accrete about $\dot{M} = 10^{-8}\,\mathrm{M_\odot\,year^{-1}}$. This accretion rate can easily be achieved through the wind of a massive star, like in Vela X-1. The question arises if even higher luminosities can be achieved through accretion. To answer this, one has to look at the interaction between radiation and the in-falling mass. The point where the force of radiation pressure F_{rad} equals the gravitational force F_G action upon the in-falling gas is the so called "Eddington-limit". Assuming neutral hydrogen to spherical-symmetric accreted, this can be expressed in formulas:

$$F_G = \frac{GMm}{r^2} = \frac{\sigma_{\mathrm{T}} S}{c} = F_{\mathrm{rad}} \tag{3.17}$$

where S, the energy flux is given by

$$S = \frac{L}{4\pi r^2} \tag{3.18}$$

G is the gravitational constant, M the mass of the neutron star, m the mass of the accreted particle, r the radius of the neutron star, c the speed of light, and σ_{T} the Thomson cross-section. Thomson scattering describes the elastic scattering of photons with ionized particles, mostly electrons. The Thomson cross-section is proportional to the square of the ratio of the mass of the electron to the mass of the proton and such much smaller for protons. Nonetheless protons are coupled electrically to electrons and thus are effected by the radiation pressure as well. When equation 3.17 is evaluated it leads to an upper limit of the luminosity (Padmanabhan, 2001):

$$L < L_{\mathrm{E}} = 1.3 \times 10^{38} \mathrm{erg\,s^{-1}} \cdot \frac{M}{M_\odot} \qquad \text{Eddington-Limit} \tag{3.19}$$

This limit was calculated for spherical symmetric accretion, which is not the case in most real astrophysical sources. The actual shape of the accretion flow in binary systems and the unique processes taking place are known for more than 30 years now (Davidson & Ostriker, 1973) and have been described en detail in many prior works (e.g., Kreykenbohm, 2004, and references therein). Here I will only describe the most important effects of a strong magnetic field onto the accretion flow, as it is important for the emerging spectra. If no magnetic field would be present, uniforming in-falling material would fall uniformly onto the surface of the neutron star. But as the in-falling material is highly ionized, it interacts with the magnetic field. The magnetic field of a neutron star can be approximated by a dipole field, which leads to a magnetic field strength of about

$$B(r) \approx \frac{\mu^3}{r} \tag{3.20}$$

where μ is the magnetic dipole moment. The value of μ is determined by $\mu = B_{\rm NS} R_{\rm NS}^3$, where $B_{\rm NS}$ and $R_{\rm NS}$ are measured at the surface of the neutron star (Frank et al., 1992). This magnetic field exerts a pressure $P_{\rm mag}$ on the in-falling material at the distance r from the neutron star, which is

$$P_{\rm mag} = \frac{\mu^2}{8\pi r^6} \tag{3.21}$$

This means, the closer the material to the star, the stronger the magnetic pressure will be. Opposing this pressure is the ram pressure $P_{\rm ram}$ which is

$$P_{\rm ram} = \frac{(2GM)^{1/2}\,\dot{M}}{4\pi r^{5/2}} \tag{3.22}$$

Setting $P_{\rm mag} = P_{\rm ram}$ and solving for r leads to the so-called Alfvén radius $r_{\rm mag}$. At this radius the magnetic field dominates the accretion flow, and the material must follow the magnetic field lines. In terms of luminosity the Alfvén radius is (Frank et al., 1992)

$$r_{\rm mag} = 1800\,{\rm km} \left(\frac{R}{10\,{\rm km}}\right)^{12/7} \left(\frac{B}{10^{12}\,{\rm G}}\right)^{4/7} \left(\frac{M}{1.4\,M_\odot}\right)^{-1/7} \left(\frac{\dot{M}}{10^{-7}\,M_\odot\,{\rm yr}^{-1}}\right)^{-2/7} \tag{3.23}$$

The most important effect of the in falling material following the magnetic field lines, is the formation of two hot-spots and the magnetic dipoles. It is at these hot-spots where the accreted material is transformed to radiative energy, i.e., X-rays. This means, that the Eddington-limit for the luminosity has to be recalculated, as equation 3.17 only holds for spherical accretion. Following Becker (1998) and Basko & Sunyaev (1976) the critical luminosity is

$$L_{\rm crit} = L_{\rm E} \cdot \frac{r_0}{4R} = 3.14 \cdot 10^{37} \times \left(\frac{M}{M_\odot}\right)\left(\frac{r_0}{R}\right)\,{\rm ergs\,s^{-1}} \tag{3.24}$$

where r_0 is the radius of the hot-spot and R the radius of the neutron star. The numerical value is true for pure Thomson scattering only. But the influence of the

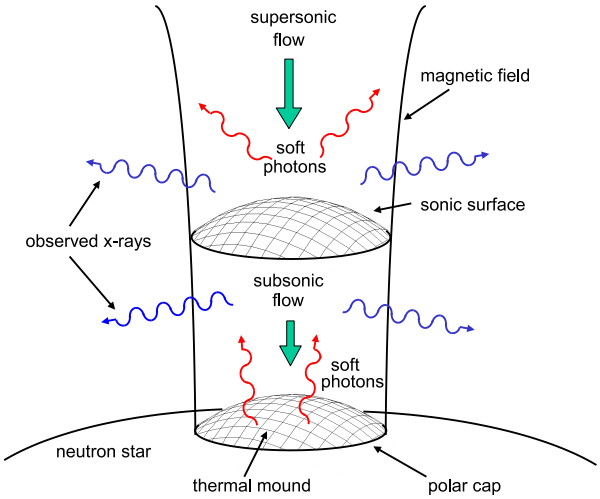

Figure 3.1.4: Schematic depiction of the accretion column and its features in a accreting neutron star (Becker & Wolff, 2007)

strong magnetic field is seen in the cross-section, too. There is a strong dependence of the cross-section on the direction of propagation of the photons with respect to the magnetic field. Becker & Wolff (2005) allow for this fact through two different energy-averaged cross-sections, $\sigma_{\parallel}$ for photons propagating along the field lines of the magnetic field and $\sigma_{\perp}$ for photons propagating perpendicular to that direction. These dependence alters the critical luminosity too

$$L_{\mathrm{crit}} = \frac{2.72 \times 10^{37} \sigma_{\mathrm{T}}}{\sqrt{\sigma_{\parallel} \sigma_{\perp}}} \left(\frac{M}{M_{\odot}} \right) \left(\frac{r_0}{R} \right) \mathrm{ergs\,s^{-1}} \tag{3.25}$$

This luminosity is smaller than the spherical-symmetric Eddington luminosity, and typical binary X-ray sources have comparable luminosities. This means, that these sources are "super-Eddington", i.e., the dynamical structure of the in falling material is dominated by the radiation pressure. The radiation can escape through the walls of the accretion funnel, and thus allowing that material is still accreted onto the neutron star. The emerging radiation pattern is called "fan-like" (Becker, 1998). Nonetheless, a radiation-dominated shock will form in the accretion column. Radiation-dominated shocks do have a defined sonic surface but are otherwise continuous velocity transitions. See Fig. 3.1.4 for a sketch of the accretion column and the shock which begins at the sonic surface.

With this model as a start point, Becker & Wolff (2007, 2005) have calculated the spectrum which emerges from the neutron star. I will briefly outline their main results.

The goal is to produce a theoretical spectrum which can be compared to known X-ray sources. As only a spectrum, which is averaged over all photon polarizations and the whole column is measured, this averaging has to be done for the theoretical spectrum, too, even though different parts of the accretion column produce different spectra. The three main sources for photons in the accretion column are from blackbody, cyclotron, and bremsstrahlung emission.

Blackbody photons are produced in the thermal mound, which represents the "photosphere" for photon creation and destruction (see Fig. 3.1.4. The temperature of the thermal mound is about $3 \cdot 10^7\,\mathrm{K}$ and thus produces photons with an energy of about $E_{\mathrm{bb}} = 2\,\mathrm{keV}$.

Cyclotron emission photons are produced in the whole accretion column through collisional excitation of electrons. The magnetic field of the neutron star is so strong, that the cyclotron frequency of electrons is quantized into Landau-Levels. The absolute values and effects of this quantization are discussed in detail in section 3.1.3. Here we will only regard the effect that electron, which was excitated to the first Landau level will fall back and emit a photon. The last important source for photons is the bremsstrahlung or free-free emission. It is produced as the electrons stream along the strong magnetic field and get accelerated. The appearance of the cyclotron energy E_{cyc} has to be taken into account when calculating the detailted spectrum from bremsstrahlung. But this would lead far beyond the scope of this work.

The injected photons from blackbody, cyclotron, and bremsstrahlung emission are exposed to strong Comptonization in the accretion column. The Compton effect describes the acceleration of a low energy photon interacting with a high energy electrons. Two different kinds of Comptonization are found by Becker & Wolff (2007): bulk and thermal Comptonization. In bulk or dynamical Comptonization, photons gain energy when scattered by uniformly streaming electrons. To increase the energies of the photons explicitly, it is necessary that the electrons are situated in a converging flow, i.e., their mean velocity increases (Turolla et al., 2002). This is the case in the accretion column of neutron stars. When reprocessing the seed photons through bulk Comptonization and allowing for the escape of the photons through the column walls, the overall shpae of different X-ray spectra can be calculated. This shape shows the typical power-law at higher energies and a blackbody spectrum at lower energies. Becker & Wolff (2005) have shown that the calculated spectra agree fairly well with the measured spectra of 4U 1258−61 and 4U 0352+30. Thermal Comptonization is the process where electrons gain energy of hot electrons, i.e., electrons with uncorrelated velocity direction. Through multiple scattering, the photons can gain stochastically energy, if the temperature of the electron gas is higher than the temperature of the photons (Rybicki & Lightman, 1986). At typical energies of neutron stars of about 10^6–$10^7\,\mathrm{K}$ and typical inflow speeds of $v \sim 0.5\,\mathrm{c}$, bulk Comptonization will always be playing a greater part in the reprocessing of the seed photons than thermal Comp-

tonization. Becker & Wolff (2007) strengthen the fact, however, that the shape of the spectra can still drastically change through thermal Comptonization. In extensive calculations using the transport equation and a eigenfunction expansion of the emerging Green's function, Becker & Wolff (2007) show that with these assumptions, the spectra of Her X-1, LMC X-4 and Cen X-3 can be modelled accurately. Only a extra iron-line has to be added to the calculated spectra, to express the feature in the measured spectra at about 6 keV. Overall, the models of Becker & Wolff (2007, 2005) seem very promising as they explain the shapes of spectra from different high-mass X-ray binaries quite well, using only sensible physical premises. The models should be compared to more well known X-ray sources, like Vela X-1. As the calculation and integration of the models is relativly complicated and time-consuming this will be done in a future work. For this thesis the spectrum of Vela X-1 is still fitted only with simple models, like a cut-off power-law, which do not have direct meaning to the underlying physical processes.

Cyclotron lines

Let us now return to the peculiar features of extremly strong magnetic fields. We have said in section 3.1.3 that the gyrotation frequencies of electrons are quantized. This can be understood quasi-classicaly, although a thorough analysis of course needs a quantum-mechanical approach, see, e.g., Grämer (2008). I will follow the aproach of Kreykenbohm (2004). Classically the Lamor-frequency ω_L, is the frequency of a electron rotating around a magnetic field line (compare section 2.1.1). The Lamor-frequency depends on the velocity $v_\perp$ of the electron perpendicular to the magnetic field and on the magnetic field B itself:

$$\omega_\mathrm{L} = \frac{v_\perp}{r} = \frac{e}{m} B \tag{3.26}$$

This simply leads to the gyrotation radius r_gyr:

$$r_\mathrm{gyr} = \frac{m v_\perp}{eB} \tag{3.27}$$

On the other hand, the de Broglie wavelength of an electron is given by

$$\lambda_\mathrm{dB} = \frac{\hbar}{mv} \tag{3.28}$$

In extremely strong magnetic fields, r_gyr can be equal to λ_dB. Similar to the Bohr-radius in atoms, this means that the frequencies around the magnetic field lines get quantized (see Kreykenbohm, 2004, and references therein). The emerging energy-levels are called Landau-levels and can be calculated to

$$E_n = mc^2 \sqrt{1 + \left(\frac{p_\parallel}{mc}\right)^2 + 2n\frac{B}{B_\mathrm{crit}}} \tag{3.29}$$

At

$$B_{\text{crit}} = \frac{m^2 c^2}{e\hbar} = 44.14 \times 10^{12}\,\text{G} \tag{3.30}$$

the cyclotron energy will be close to the rest mass of the electron, 511 keV, which then requires a complete relativistic treatment of the problem. As we do not measure such high magnetic fields in Vela X-1, this calculation is not done here. From equation 3.29 we can calculate the difference between two Landau levels to

$$E_{\text{cyc}} = \hbar\omega = \frac{\hbar e B}{e} \approx 11.57 \times B_{12} \tag{3.31}$$

The final result in equation 3.31 is known as the 12-B-12 rule, as B_{12} describes the magnetic field strength in terms of 10^{12} G. We denoted the difference with E_{cyc}, as this difference is the important cyclotron energy. This energy is necessary to bring the electron from one Landau level to the next, i.e, a photon with the energy $E_{\text{cyc}} = h\nu$ can be absorbed by the electron. The lifetime of an excited state is extremely short, so that the electron will decay to the ground state almost immediately, emitting a photon with an energy of E_{cyc}. This high decay rate makes it meaningful to talk about a scattering process, rather than a absorption and emission process. Photons with an energy equal to the cyclotron energy do have a very high optical thickness in the accreting material, meaning that it is very unlikely for them to leave the accretion column. This means that in the measured spectrum as a line-like feature at the cyclotron energy. It is important to note that this feature is due to a scattering process and thus correctly called "Cyclotron resonant scattering feature" (CRSF) rather then simply cyclotron line. Unfortunatly, the CRSFs are not seen as nice, small lines in the measured X-ray spectra. Mostly only small dips in the spectra are seen, dominated by the overall shape of the spectra. A good example with apparant CRSFs is shown in Fig. 3.1.5. This spectrum was taken with PCA and HEXTE aboard of *RXTE*.

The scattering features are smeared out by several effects, beginnig with thermal broadingn due to the high temperatures in the plasma. Additionally, the scattering cross section is not a delta function, but broadend to some extend (Araya & Harding, 1999) . This means, that photons with slightly different energies can scatter resonantly with electrons. Another very important ones is the so-called photon spawning. This happens, when the electron is excited to a higher level than the first. When it deexcites, it will emit more than one photon. In the relativistic regime, the Landau levels are not spaced equidistant. This means the photons from different levels do have slightly different energies, and thus smear the line out. Additionally gravitational redshift changes the energy of the photons. Through Monte Carlo simulations Schönherr et al. (2007) have investigated these effects. When measuring CRSF in spectra of X-ray binaries it is thus important, to look very carefully at the spectrum. It can happen, that the second harmonic, meaning photons which deexcitated two Landau levels at once, is more prominent than the ground frequency. But to get a correct measurement of the magnetic field of the neutron star, it is important to know the ground level.

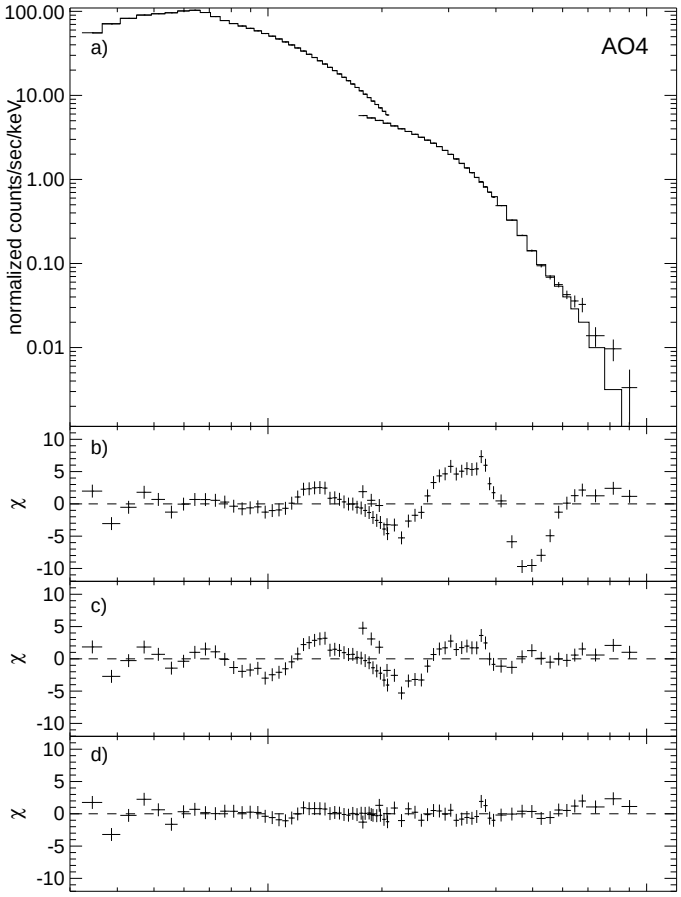

Figure 3.1.5: Spectrum of Vela X-1 taken with *RXTE*. Panel b) shows the residuals with only the continuum modeled, c) with the added first CRSF and c) with both CRSF modeled (from Kreykenbohm, 2008, priv. comm.)

When this is ensured, measuring the energy of the CRSF is the most direct way to get a measurement of the magnetic field of the neutron star. This helps to check the theories about stellar evolution.

3.2 The INTEGRAL satellite

Satellites are today the most common observatories for X-rays. One of the best for high-energy X-rays is the European "INTErnational Gamma-Ray Astrophysical Laboratory" (*INTEGRAL*) (Winkler et al., 2003). It offers very good imaging

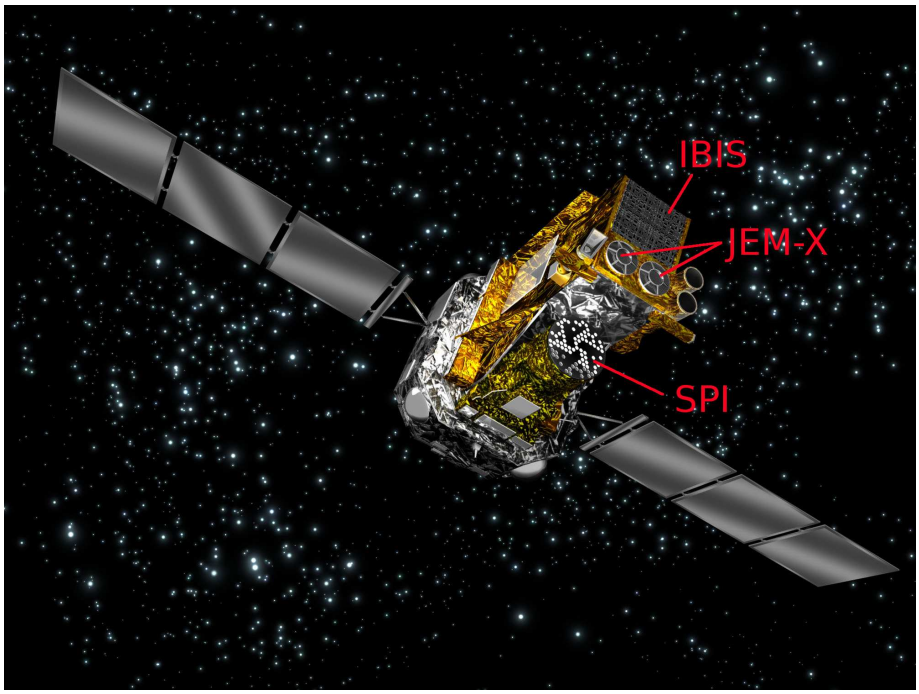

Figure 3.2.6: An artistic view of the *INTEGRAL* satellite in space. The instruments IBIS, JEM-X and SPI are marked.

capability for photons up to 10 MeV and unmatched spectral resolution for energies up to 8 MeV. Fig. 3.2.6 shows an artistic view of the satellite in space.

INTEGRAL is in a highly eccentric orbit around the Earth, with a perigee of 9 000 km and a apogee of 152 600 km. The orbit has an inclination of 51.67 deg and it takes the satellite 72 h to travel once around the Earth. Due to Kepler's Second Law (Kepler, 1609), the satellite spends most of its time outside the radiation belts of the Earth, see Fig. 3.2.7. This helps to reduce the background radiation, which could easily spoil the observations as the detectors are extremely sensible to achieve their scientific goals. The orbital period means that every 3 days near its perigee *INTEGRAL* is not able to take any scientific data, but can observe one source continuously for the rest of the time.

3.2.1 Coded masks

It is not possible to refract high energy X-ray photons in the same way as at optic wavelengths. This is due to the fact, that the X-ray photons have wavelengths on the order of atomic radii and thus interact in a completely different way with material.

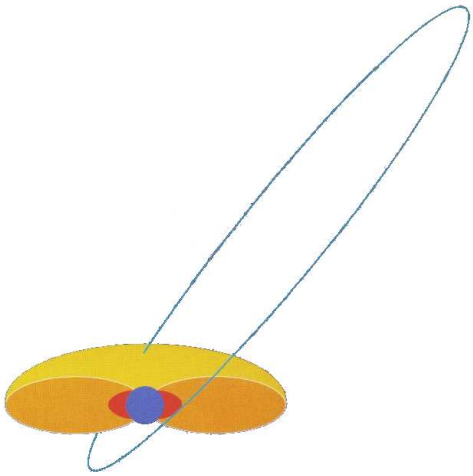

Figure 3.2.7: A sketch of the orbit of *INTEGRAL*, shown in blue. In yellow the approximate size of the radiation belts is shown (from `http://isdc.unige.ch/index.cgi?Outreach+integral`).

The refractive index can be calculated to (see Fritz, 2008, and references therein)

$$n = \left(1 - \frac{\omega_\mathrm{p}^2}{\omega^2}\right)^{1/2} \tag{3.32}$$

where ω_p is the plasma frequency of the refracting material and $\omega_\mathrm{p} \propto Z$, the atomic mass number. ω_p is typically in the range of some $10^{12} - 10^{15}$ Hz, compared to about $1.5 \cdot 10^{18}$ Hz for 1 keV X-rays. As equation 3.32 shows, refractive indices which are distinctly different from 1 need materials with extremely high Z. But in materials with high Z absorption of X-rays plays an important role as the absorption coefficient σ_PI for photoionization is $\propto Z^5$. Thus no focusing lenses can be built for X-rays. The same holds for reflecting mirrors as used commonly in the optical, as X-rays are merely absorbed in the material but not reflected. One often used technique to reflect and focus X-rays are the so-called Wolter-Telescopes (Wolter, 1952) which use total reflection at gracing incidence angles. Famous satellite missions using this technique are "Chandra" and "XMM-Newton". With the help of Snell's law and a Taylor series expansion, one can conclude that the critical value β_crit of the incident angle where total reflection occurs is (Fritz, 2008)

$$\beta_\mathrm{crit} = \frac{\omega_\mathrm{p}}{\omega} \tag{3.33}$$

β_crit thus depends on the inverse of the frequency of the photons. For 20 keV X-rays the angle drops to about $\beta_\mathrm{crit} = 0.45 \cdot 10^{-3}$ when using gold ($\omega_\mathrm{p}^\mathrm{Au} = 3.8 \cdot 10^{15}\,\mathrm{sec}^{-1}$, Tretyakov, 2007) as reflecting material. This makes the use of Wolter-telescopes, if not impossible, very impractible at these energy ranges.

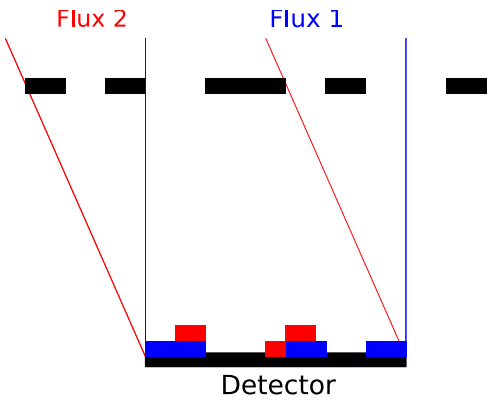

Figure 3.2.8: A simple example of a one-dimensional mask. Flux 1 is producing counts in the bins shown in blue, while flux 2 of the same power is producing counts in the bins shown in red (after in't Zand, 1992).

Other methods to image the sky in hard X-rays have been discussed, see, e.g, Groeneveld (1999) and references therein. The technique used most often and at all instruments of *INTEGRAL* are the "coded masks telescopes". This technique makes use of a coded mask, which is a grid with opaque and transparent parts placed at some distance above the detector. When the mask and the detector are illuminated by a single source, this source will produce a unique shadow on the detector through which the location of the source can be estimated. In Fig. 3.2.8 the simplest case of a one-dimensional mask is depicted. Flux 1 produces the blue counts, flux 2 the red ones. It is obvious, that the same flux prodcues different shadows when in different position on the sky.

The "coded mask method" thus encodes the image of the sky via the mask. Only this encoded image is seen by the satellite, and no direct imaging technique like in optical or Wolter-telescopes is possible. To reconstruct the image of the sky the coded image needs to be decoded again, done in second step the so called "deconvolution". Such a technique involving more than one step to achieve the final image is know as spatial multiplexing technique (Caroli et al., 1987). When more than one source is in the field of view, special requirements are put to the coded mask. If its auto-correlation function is not a delta-function, sources in different positions of the sky can lead to the same shadow image on the detector. A perfect delta-function is only achieved, when using just one hole, like in a pinhole camera. In fact, a pinhole can be seen as the simplest implementation of a coded mask instrument, allthough it is a directly measuring instrument and no multiplexing is needed. Only one hole with a small aperture however reduces the effective area of the detector drastically, which leads to a worse signal-to-noise ratio. A larger aperture of the pinhole on the other hand would lead to decreased spatial resolution (in't Zand, 1992). Good spatial resolution

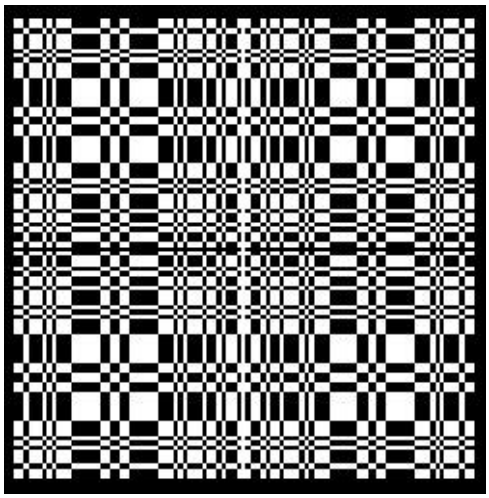

Figure 3.2.9: The coded mask of IBIS, which uses a cyclic replication of MURA

at large effective opening can be achieved when placing more pinholes in the mask, e.g., a multi-pinhole camera. The location of the pinholes in the mask defines the code through wich the image is encoded. Another restriction to the coded mask is, that preferably a simple and fast reconstruction of the shadow image should be possible, too. There are different algorithms and approaches to calculate a near optimal coded mask, see, e.g., in't Zand (1992). As an example, Fig. 3.2.9 shows the coded mask of one of the instruments aboard *INTEGRAL*, IBIS, which uses a cyclic replication of a "Modified Uniformly Redundant Array" (MURA) of order 53 (see the "IBIS Analysis User Manual"). The mask is about 50% opaque and still allows a very accurate reconstruction of many sources in the field of view. Fig. 3.2.10 shows a sketch of the IBIS detector, illuminated by two sources. It is clearly seen, that the shadow image is quite complicated, especially when considering the overlay of the two sources. Still, through the carefully chosen mask, it is easily possible to evaluate the correct position of the sources in the sky, even for more than a dozen sources.

To further improve the resolution and quality of the reconstructed images, *INTEGRAL* usually operates in a such a way, that it does not stare onto one point for the whole observations time, but that the observation is split into many single pointings, separated by about 2 deg. This means, that in each pointing the sources are shifted a little bit and thus provide more information about their location (Courvoisier et al., 2003).

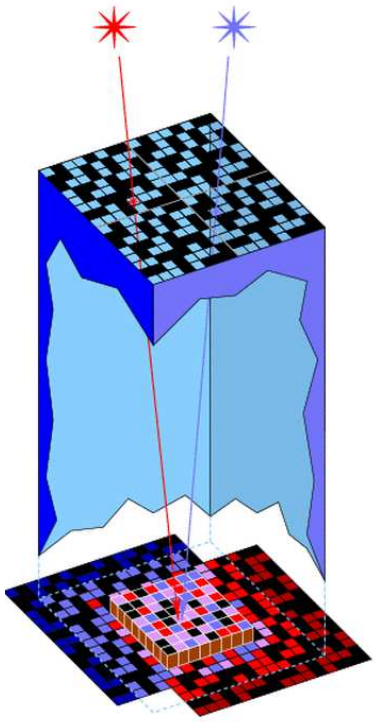

Figure 3.2.10: An example of the IBIS detector, illuminated by two different sources, shown as stars in red and blue. The overall shadow image on the detector is measured and can be used to calculate the position of the two sources.

3.2.2 The instruments of *INTEGRAL*

The following analysis of Vela X-1 in section 3.5 is mostly performed with data from the X-ray instruments aboard *INTEGRAL*. Three different X-ray instruments are located aboard the satellite: the SPectrometer on *INTEGRAL* (SPI), the Imager on Board the *INTEGRAL* Satellite (IBIS) and the Joint European X-ray Monitor (JEM-X). The IBIS instrument is described in detail in Ubertini et al. (2003), here I will only discuss the most important facts. IBIS consits of two independent detectors, placed atop of each other. On top is the *INTEGRAL* Soft Gamma-Ray Imager (ISGRI), which consists of 8 detection units made of Cadmium Telluride compromising 16 384 pixels and a total sensitive are of 2621 cm^2 (Lebrun et al., 2003). ISGRI is sensitive in the range between 15 keV and 1 MeV and offers a angular resolution of 12 arcmin, while having a field of view of 9×9 deg. The spectral resolution of ISGRI is only 9% at 100 keV. All the lightcurves used in this work, see section 3.5, are made with this instrument. The other detector of IBIS is the "Pixellated Imaging CaeSium Iodide Telescope" (PICsIT) which is sensitive in the energy range between 175 keV

Table 3.2.1: Facts about the X-ray instruments aboard *INTEGRAL*

	IBIS (ISGRI)	**SPI**	**JEM-X**
Effective area (cm^2)	2621	508	500
Field of view (deg)	9×9	16	4.8
Spatial resolution	12 arcmin	2.5 deg	3 arcmin
Energy range (keV)	15 – 1000	20 – 8000	3 – 35
Energy resolution	9 keV at 100 keV	2.33 keV at 1.33 MeV	1.2 keV at 10 keV

and 10 MeV (Di Cocco et al., 2003). It consists of CsI(Tl) scintillation crystals and has a total sensitive area of 2890 cm^2. Its angular resolution is the same 12 arcmin as the one of ISGRI, as the resolution is determined by the coded mask. Sadly, the very high background reduces the possibilities of PICsIT, as not enough telemetry is available and only certain parts of the scientific data can be submitted. For this reason, no PICsIT data is used in this work. The low energy range aboard *INTEGRAL* is the JEM-X detector. JEM-X consists of two independent instruments, which have the same coded-mask but rotated by 180 deg. The aperture of JEM-X is circular and the underlying algorithm of the coded-mask is a different one than for IBIS. In JEM-X only 25% of the mask are transparent, to achieve better angular resolution, but not at least to save telemetry data (Lund et al., 2003). JEM-X is sensitive between 3–35 keV as a field of view of only 4.8 deg diameter with 3 arcmin spatial resolution. It detects X-rays via micro strip gas counters with an effective area of 500 cm^2 in each instrument. The small field of view restricts the monitoring capabilities of JEM-X, so that no successional lightcurves can be presented in this work. Nonetheless, spectra of JEM-X are calculated, where JEM-X offers a resolution of 1.2 keV at 10 keV. The last X-ray instrument of *INTEGRAL* is SPI, which is sensitive between 20 keV and 8 MeV and offers outstanding spectral resolution of 2.33 keV at 1.33 MeV (Vedrenne et al., 2003). The detectors are made of high purity germanium and have geometrical area of 508 cm^2. The field of view of SPI is 16 deg with an angular resolution of 2.5 deg. SPI uses again some other coded-mask, where about 59% of the pixels are opaque. The single pixels consit of 30 mm thick tungsten to absorb X-rays up to 1 MeV with an efficiency of 95%. No SPI spectra can be presented in this work, as the countrate of Vela X-1 is too low in that high energy range as to be properly measured by the instrument. Table 3.2.1 summarizes the most important facts about the instruments aboard *INTEGRAL*.

Data of *INTEGRAL* is provided by the "*INTEGRAL* Science Data Center" (ISDC) located in Versoix near Genève in Switzerland. The data are provided in single files, each consiting of one "Science Window" (ScW). One ScW is usually on pointing, spanning typically over 1800 sec, 2200 sec or 3600 sec. Time on *INTEGRAL* is measured in "*INTEGRAL* Julian Date", which is the Modified Julian Date (MJD) minus 51544. 51544 MJD is midnight January 1, 2000. MJD can be converted to Julian Date (JD)

by adding 2 400 000.5, which is then the time in days since noon January 1, 4713 BC. The ISDC additionally provides the software pipeline to reduce the data. The standard pipeline is split into different levels, depending on the instrument. In the following I will depict the most important steps of the IBIS-pipeline, as most of the analysis of this work is based upon data from that instrument. In the first step the deconvolution of the shadow image or shadowgram is done. In IBIS this is done in a straightforward way, by folding the data with the inverse of the coded-mask. Using the inverse of the coded-mask is only useable as long as the auto-correlation function of the mask is close to a δ-function. At the edges of the field of view, this is no longer the case, as only parts of the detector are illuminated by the light of the source. So every sky-pixel has to be calculated seperatly through the folding of the data with an extended inverse array of the mask (Goldwurm et al., 2003). This calculation can be very computationally intesive. In the reconstructed image a iterative search for sources is done, and all identified soures are stored with their coordinates and their flux in a catalog. As the deconvolution process is not perfectly stable, it is necessary to check the catalog and the image if all the correct sources were located. Based upon a corrected version of the catalog, the pipeline can extract spectra and lightcurves of the sources. The standard pipeline is doing a complete deconvolution of the shadowgrams for every new data point in a spectrum or a lightcurve, because this is the safest way to calculate the correct fluxes. As was said, the deconvolution can be quite time consuming and so no lightcurves with high-time resolution can be extracted in this way, as the computational time would be immense. To extract lightcurves with higher time resolution, the software `ii_light` is provided. It is not part of the standard pipeline, but maintained at the ISDC as well. `ii_light` is using a "Pixel Illumination Factor" (PIF) to construct the lightcurves. This means, it uses fixed sources and fluxes and calculates which pixel of the detector would be illuminated by how much of the flux. With these values the actual flux of the source is adjusted. This way, lightcurves up to about 0.1 sec resolution can be extracted without overloading the computational abilities. As shown in section the values of `ii_light` are nonetheless trustworthy.

3.3 Vela X-1

VELA X-1 is a high mass X-ray binary system (HMXB). HMXB are systems consisting of two stars, a compact object and a supermassive star. The compact object is in the case of Vela X-1 a neutron star, while the supermassive star is a B0.5Ib supergiant known in the optical as HD 77581 or GP Vel. HD 77581 has a mass of about $23\,M_\odot$ and a radius of about $30\,R_\odot$ (van Kerkwijk et al., 1995), while the mass of Vela X-1 was calculated to be $1.8\,M_\odot$ by Quaintrell et al. (2003). This mass is one of the highest masses of all known neutron stars. Using a distance of 2.0 kpc (Sadakane et al., 1985) the luminosity of Vela X-1 is about $\sim 4 \times 10^{36}\,\mathrm{erg\,s^{-1}}$ (Kreykenbohm,

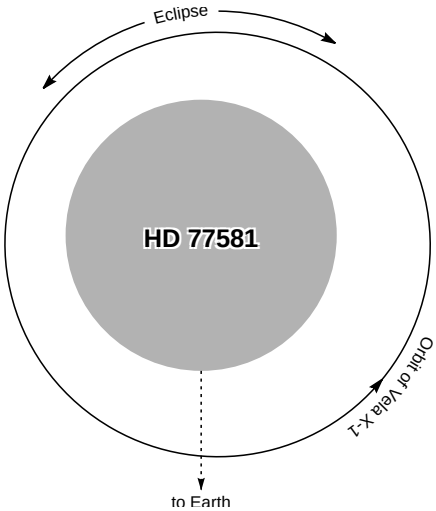

Figure 3.3.11: Sketch of the orbit of Vela X-1, using the values $a \sin i = 112.98$ lt-sec, $e = 0.0885$, and $\omega = 150.6$ (Kreykenbohm et al., 2008). Plot after Kretschmar et al. (1997b).

2004), which is typical for an X-ray binary. The system was first seen in the X-ray band by Chodil et al. (1967) on their second rocket flight. They reported it as a very weak source. This is why it took 5 more years of detector development and a satellite mission to detect a 9 day period in the lightcurve of Vela X-1 (Ulmer et al., 1972). This period was correctly interpreted as the orbital period of Vela around its companion and could only be seen so clearly because Vela X-1 is an eclipsing binary system. In 1976, McClintock et al. (1976) discovered a 283 sec variation in the lightcurve of Vela X-1. This was the final clue that Vela X-1 is indeed a neutron star. The newest measurements of the star give values of 283.5320 ± 0.002 s for the rotation period and 8.964386 ± 0.000015 d for the orbital period (Kreykenbohm et al., 2008). The pulse period is known to change erratically (Bildsten et al., 1997), in a random walk like manner on all timescales (Deeter et al., 1989). The amplitude of the changes is about 0.2 s, which can be neglected for the goal of this work. Erratic changes in the pulse period are typical for neutron stars embedded in a stellar wind (Matsuda et al., 1987). This is the case in the Vela X-1 system, as HD 77581 is a relatively young star, which has a strong stellar wind of about $\dot{M}_\star = 4 \times 10^{-6}\,\mathrm{M}_\odot\,\mathrm{yr}^{-1}$ (Nagase et al., 1986) and the semimajor axis of Vela's orbit is only about $1.8\,\mathrm{R}_\star$ (Barziv et al., 2001). Fig. 3.3.11 shows a scale to scale sketch of the orbit. As can be seen, the neutron star orbits very close to the red supergiant.

Nagase et al. (1986) additionally stated that the stellar wind should be clumpy, in order to account for the soft-excess. Sadakane et al. (1985) also find, that the wind must be highly structured through infrared observations with the "International Ultraviolet

Explorer" (*IUE*) satellite. This goes well with the fact that Vela X-1 is known for its high variability in intensity. Inoue et al. (1984) and Kreykenbohm et al. (1999) found that the luminosity is sometimes reduced to less then 10% of its usual value, while Kreykenbohm et al. (2008) found giant flares with about 700% of the luminosity of the normal state. These large variability can be ascribed to the fact, that through the clumped wind, the mass accretion rate $\dot{M}$ changes dramatically on short timescales and thus leading to drastic changes in the X-ray brightness. The possible physical processes behind this variability will be discussed in more detail in sect. 3.5.3.

The pulse profile of Vela X-1 looks quite different in different energy bands. It is determined by averaging the lightcurve over several periods. Although Vela X-1 shows a strong pulse-to-pulse variability, the time-averaged pulse profile is constant throughout long time intervals (Staubert et al., 1980). As can be seen in Fig. 3.3.12, the shape of the pulse profile has a quite complicated structure with 5 discernible peaks up to about 10 keV. At higher energies the shape evolves into a simple 2-peaked profile (Raubenheimer, 1990; Kreykenbohm et al., 1999). At higher energies the two-peaked profile is persistent, but Kreykenbohm et al. (2008) notice that there are slight, energy-dependent differences in the shape of the two peaks.

In the spectrum of Vela X-1 a Cyclotron Resonant Scattering Feature (CRSF) (see sect. 3.1.3) was found firstly by Kendziorra et al. (1992). Kreykenbohm et al. (1999) confirmed two CRSF, one at about 23.3 keV, the first harmonic at about 54.5 keV (see Fig. 3.1.5). As was said in sect. 3.1.3 it is important to know the energy of the fundamental line to infer to the correct magnetic field of the neutron star. With the values of Kreykenbohm et al. (1999) this leads to a magnetic field strength of $B \approx 2 \times 10^{12}$ G, when neglecting the gravitational redshift. Using *INTEGRAL* observations from November 2005, Schanne et al. (2007) could confirm two CRSF, at ≈ 27 keV and ≈ 54 keV. Additionally, Grämer (2008) found both lines in HEXTE data, so that the fundamental line with ~ 25 keV can be accepted as proven.

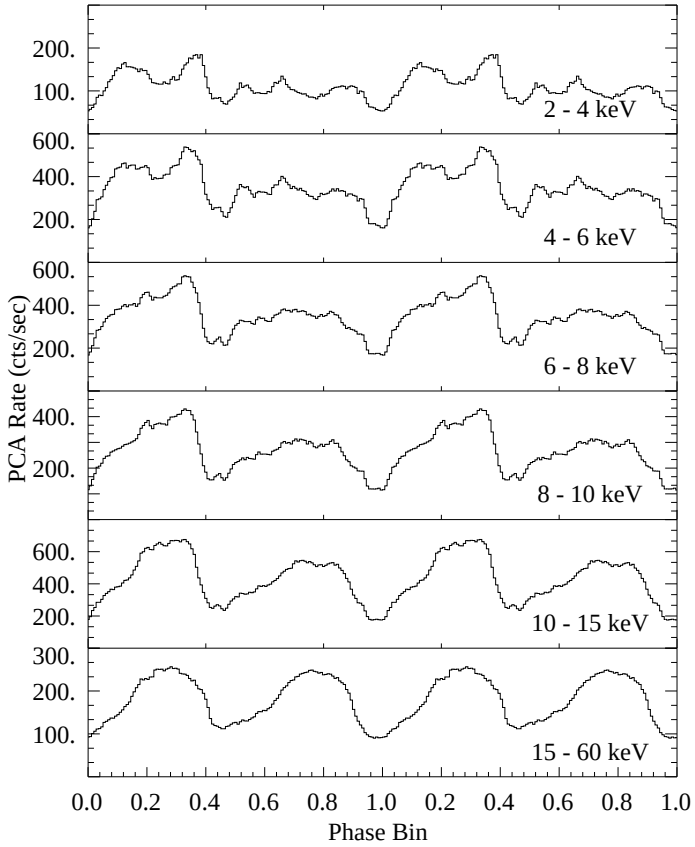

Figure 3.3.12: Pulse profiles of Vela X-1 for different energy bands. Adopted pulse period is 283.5320 s (Kreykenbohm et al., 1999)

3.4 The statistical approach

THE data analyzed in this work spans over a time range of $\sim$ 3.6 Msec, which is a large amount of data compared to other measurements. Parts of the data have been analyzed in great detail already (Kreykenbohm et al., 2008; Schanne et al., 2007), presenting lightcurves and spectra. A repetition of these works was not aimed for, instead another ansatz was taken, namely to analyze the data statistically. The amount of available data made this statistical approach very intriguing. Statistical approach means that not individual events are regarded, but all events are binned in some kind of common grid. For example, the lightcurve is binned into a histogram with N bins, ranging from $B_{\min}$ to $B_{\max}$. Following the definition of the "IDL Reference

Guide" [1], one bin would than have the size of

$$\text{Binsize} = (B_{\max} - B_{\min})/(N-1) \tag{3.34}$$

Every data point in the lightcurve is assigned to one specific bin, according to its countrate. With F_i the countrate of the data point, and v the number of the bin this binning can be written as

$$P(F_i, v) = \begin{cases} 1 & v \leq (F_i - B_{\text{Min}})/\text{Binsize} < v+1 \\ 0 & \text{otherwise} \end{cases} \tag{3.35}$$

which leads to the histogram function H_v

$$H_v = \sum_{i=0}^{N-1} P(F_i, v) \tag{3.36}$$

These binned data per se do not bear that much information, as it is only a small sample of an underlying distribution. More information can be extracted by fitting an adequate distribution function to the histogram. The idea behind the fit is that the fitted distribution describes the underlying function . The most common distribution is surely the Gaussian distribution, which is a symmetric distribution around its mean. This is due to the "Central Limit Theorem" (Roe, 2001), which states that the sum of independent random variables will be normal distributed. This means, when measuring the random variable $y = x_1 + x_1 + \cdots + x_n$, where the x_i are independent random variables, the function $F((y - \bar{y})/\sigma_y)$ will be normal distributed for large n. Here $\bar{y}$ denotes the mean value of all y and σ_y the variance. These kind of sums of random variables is always there present, where many independent effects influence the measured value in an additive way. These influence may not be clear and can not be named explicitly, but it is obvious that every physical process is under the influence of such processes. In particular, the distribution of uncertainties of observational errors follows a normal distribution. Furthermore, many physical processes like the Brownian Motion (Einstein, 1905) can be described by a normal distribution. If a random variable y is measured, which is described by the multiplication of many independent random variables x_i, the emerging distribution is a log-normal distribution (Roe, 2001). This is easy to see, as

$$y = x_1 \cdot x_2 \cdot \ldots \cdot x_n = \prod_{i=1}^{n} x_i \tag{3.37}$$

$$\Rightarrow \log y = \log\left(\prod_{i=1}^{n} x_i\right) = \sum_{i=1}^{n} \log x_i \tag{3.38}$$

[1] `http://find.uchicago.edu/idl_help/refguide.pdf`

which is the sum of independent random variables and thus normal distributed in the limit of large n. The log-normal distribution is not symmetric, but as an extended tail to higher values. It is evident that in a logarithmic plot the distribution looks like a usual Gaussian. The log-normal distribution is also common in physical processes, one simple example is a photomultiplier tube. In a photomultiplier a incoming photon knocks out $a \pm \sigma_a$ electrons out of the first anode. Every single one of these electrons knocks out $b \pm \sigma_b$ electrons at the second anode, which knock out more electrons at the third and so forth. The number of knocked out electrons is randomly distributed, so that the final number of electrons is the multiplication of independent random variables. This means, it will follow a log-normal distribution. Not only in hard physics, but in the vivid field of econo- or social physics the log-normal distribution plays an important role, like in the distribution of e-mail traffic (Stouffer et al., 2006) or in financial time series (see Bacry et al., 2008, and references therein). The log-normal distribution also describes the histograms of the countrates of Vela X-1 well, as discussed in Sect. 3.5.3. Another important, non-symmetric distribution function is the Weibull-distribution (Weibull, 1951). The Weibull-distribution was used in chapter 2 to described the shape of the SAA. Weibull distributions are applicable for a wide range of phenomena, like the distribution of the wind speed over oceans (Pavia & O'Brien, 1986). See Brown & Wohletz (1995) for an overview. It is important to note that the log-normal distribution and the Weibull distribution can look quite similar for the right set of parameters. To understand the underlying physical processes correctly, it is important to use the correct distribution. For discussions on the discrimnations between these two distributions see Szajnowski (1977) or Sekine et al. (1987). For the data presented in Sect. 3.5.3 the log-normal distribution leads to a distinctly better fit than a Weibull distribution and is furthermore explainable by a successful model.

3.5 Results

3.5.1 Lightcurves and hardness-ratios

I analyzed three sets of data for a total of about 3.6 Msec observation time. The first block was from *INTEGRAL* revolution 137 to 141 which translates to a start-date of 2003 November 27 and an end-date of 2003 December 11. These data were also analyzed in detail by Kreykenbohm et al. (2008). The second data block started in revolution 373 and ended in 383, which means it lasted from 2005 November 04 to 2005 December 04. These data have been preliminary analyzed by Schanne et al. (2007). The last block started in revolution 433 and ended in revolution 440. This is date 2006 May 2 to 2006 May 24. The detailed timing information is summarized in table 3.5.2.

Table 3.5.2: Dates and Revolution data of the investigated observations

Block	ScW	MJD	Data
1	013700070010 – 014101140010	52970.4 – 52984.9	03/11/27 – 03/12/11
2	037300480010 – 038300480010	53678.1 – 53708.3	05/11/04 – 05/12/04
3	043300470010 – 044000600010	53857.1 – 53879.1	06/05/02 – 06/05/24

Lightcurves were extracted from ISGRI in three different energy bands: 20–40 keV, 40–60 keV, and 20–60 keV with 283.5 sec time-resolution. The time resolution was chosen to average each data-point over one pulse period and so to eliminate these fluctuations. In Figs. 3.5.13, 3.5.14, and 3.5.15 the lightcurves of the 20–60 keV band for the respective blocks are shown in the upper panel. The vertical dashed lines show the beginning and the end of the eclipse according to the ephemeris data from Kreykenbohm et al. (2008), and the dash-dotted line shows the respective center of eclipse. The black curve is extracted using *ii_light* with a time resolution of 283.5 sec. The red curve is the average of the *ii_light* data averaged over one Science Window (ScW). The blue curve is the count-rate as calculated for each ScW using the *ii_lc_extract* routine from the standard pipeline. These data is read from the `isgri_sky_res.fits` files, which were created for every single ScW and will be referred to as "skyres-data". The standard pipeline is deconvolving the shadograms of the detector to images, while looking for a given number of sources. For these sources flux data are then written to `isgri_sky_res.fits`. There are data missing in some ScWs, especially in the eclipse. This is due to the fact that the pipeline did not find Vela X-1 in these ScWs and thus no flux could be calculated. For *ii_light*, however, a fixed position for Vela X-1 is used, as *ii_light* is not making a complete deconvolution of the shadogram. This means, values are calculated even if Vela X-1 is not or only hardly visible. These values are not to be mistaken for actual fluxes as they only show the systematic uncertainty of the routine and the detector. For example in eclipse, almost no photons are emitted into our line of sight, still the flux is not identical zero. Still the flux values can be physical relevant even at times, were Vela X-1 was not found in the deconvolved image of the ScW. The "IBIS Analysis User Manual"[2] cautions that *ii_light* should be used carefully when determining absolute fluxes and rather be used only to check the relative variability on short time-scales. Our lightcurves show clearly, however, that the fluxrates extracted with *ii_light* can be trusted, as was stated by Kreykenbohm et al. (2008) already. This is additionally supported by the fact that a Kolmogorov-Smirnoff-Test (K-S-Test) (Smirnoff, 1939) between the two lightcurves leads to a p-value of 0.99741. This means, it is highly probable that the two lightcurves are statistically identical and no artifical bias is measured. The K-S-Test was performed using the S-Lang Statistics Module by John

[2] `http://isdc.unige.ch/Soft/download/osa/osa_doc/prod/osa_um_ibis-7.0.pdf`

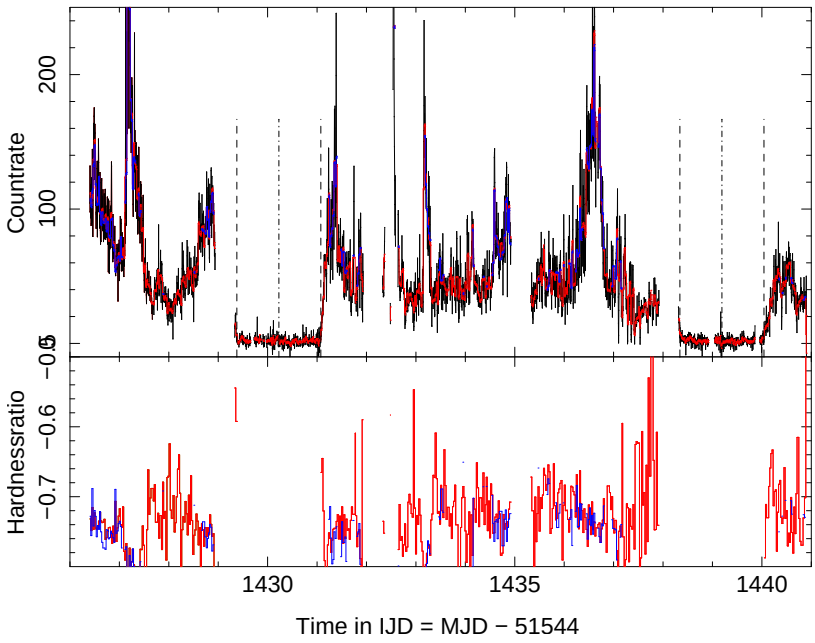

Figure 3.5.13: Lightcurve in the 20–60 keV band and hardness-ratio of the first data block, ranging from 2003 Nov 27 to 2003 Dec 11. For the hardness-ratio the hard band from 40–60 keV and the soft band from 20–30 keV was used.

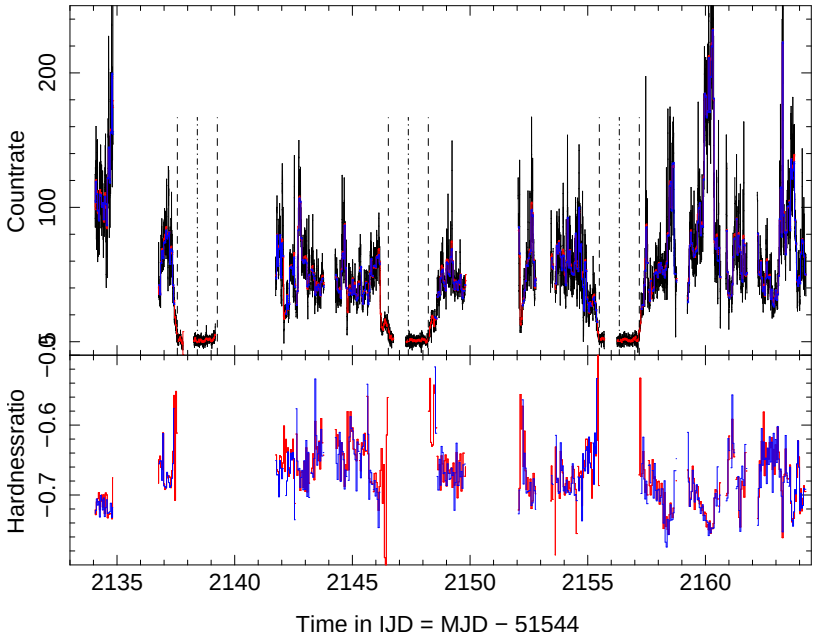

Figure 3.5.14: Same as Fig. 3.5.13 for for the second data block, ranging from 2005 Nov 04 to 2005 Dec 04.

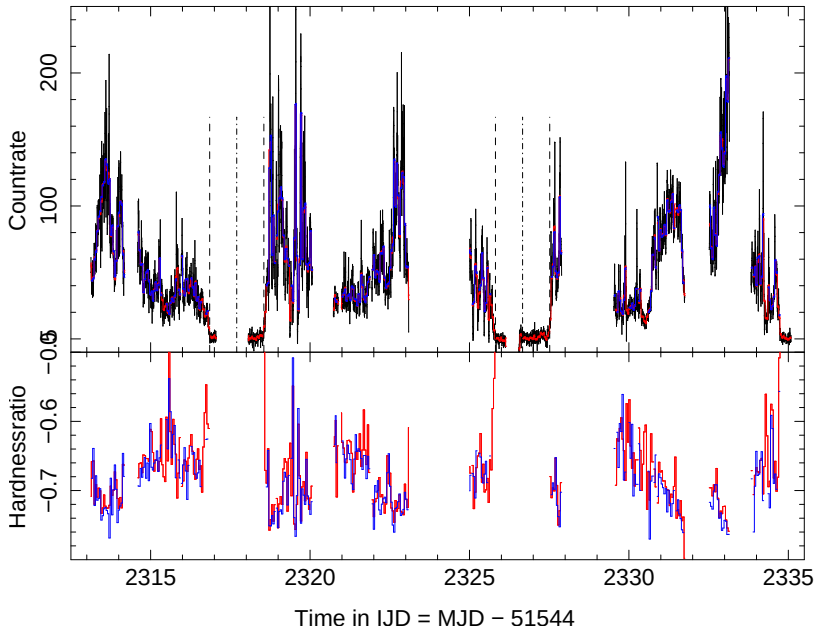

Figure 3.5.15: Same as Fig. 3.5.13 for for the third data block, ranging from 2006 May 02 to 2006 May 24.

E. Davis, available freely in the internet[3]. To further quantify the relation between the two lightcurves and to analyze it in different energy bands I calculated the ratio between the data from *ii_light* and the skyres-data for every ScW. These values were rebinned into 256 bins between a ratio of 0.8 and 1.2 and then plotted as histogram separately for each energy band, see Fig. 3.5.16. The colors represent the different energy bands, but as can be seen easily all three curves have their peak at about 1 and follow a normal distribution. A normal distribution is a good indicator that the variance is a stochastic process and no systematic error is made. The mean values and variances for each energyband are shown in table 3.5.3. This further puts confidence in the values extracted via *ii_light*. I have to caution, however, that the K-S-Test of the lightcurves in the 40–60 keV leads only to a p-value of 0.63977. I ascribe this to the fact that the countrates in the hard-band are typically lower, and both routines, *ii_light* as well as *ii_lc_extract*, do not perform so well at low countrates. The value is still large enough to be confident that the overall behavior of the lightcurves is still very similar.

The second panel of Figs. 3.5.13, 3.5.14, and 3.5.15 shows the hardness-ratio for the respective data blocks. Again, the colors represent the different procedures used to extract the rates, red for data of *ii_light*, blue for the skyres-data. The hardness-ratio is only given on the timescale of ScWs to smooth out the noise. The hardness-ratio ϑ

[3] `http://space.mit.edu/cxc/software/slang/modules/stats/index.html`

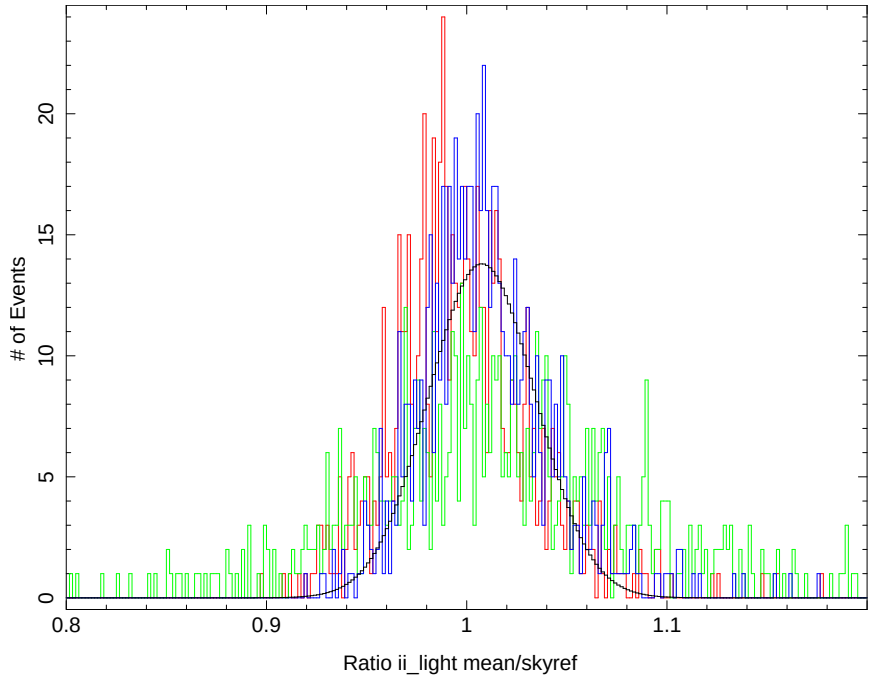

Figure 3.5.16: Histogram of the ratio between *ii_light* and the skyres-data. The 20–30 keV band is shown in red, 40–60 keV in green and 20–60 keV in blue. Superimposed in black is the best fit Gaussian to the 20–60 keV data.

Table 3.5.3: Mean values and variances for the distribution of the ratio between *ii_light* and the skyres-data. Additionally is the color code for Fig. 3.5.16 given.

Energy band (keV)	color	Mean values	Variance
20–30	blue / black	0.997	0.036
40–60	red	1.020	0.076
20–60	green	1.010	0.034

is calculated as

$$\vartheta = \frac{H - S}{H + S} \tag{3.39}$$

where H is the countrate in the hard band between 40–60 keV and S is the countrate in the soft band between 20–40 keV. A larger value of ϑ, i.e., a less negative value, is called harder, where as smaller values of ϑ is called softer. The hardness-ratio is a gauge for the physical processes taking place and is indicating the shape of the spectra. A overall brightening of the source would not result in a change in ϑ, but when the spectral shape changes, this is seen in the hardness-ratio as well. The advantage of the hardness-ratio is that it can be calulated on short timescales, while for reasonably god spectra longer exposure times are needed. In Figs. 3.5.13, 3.5.14, and 3.5.15 it can be

clearly seen that in the flares, e.g, at $t = 26$ in Fig. 3.5.14, Vela X-1 becomes distinctly softer. But this is not the only time the spectrum becomes softer. A more active and brighter phase of Vela X-1 has almost always a softer hardness-ratio, too. This can be seen nicely in Fig. 3.5.15 at $t = 2321$–2323 and $t = 2329.5$–2331.5. Especially in the bright part of the second time range, ranging from about $t = 2330.5$–2331.5, Vela X-1 does not show distinct flaring, but is overall almost thrice as bright as in first part, ranging from $t = 2\,329.5$–2331.5. To analyze this behavior more closely, I took a look at the spectra in this time range. As the time range is relatively short, I combined the spectra from the both active states of Fig. 3.5.15 and the spectra from the two quiet states. Both combined spectra were fitted in XSPEC (Arnaud, 1996) independently but with the same model, namely

$$I(E) = C \cdot (I_{\mathrm{phabs}} \cdot I_{\mathrm{cont}}) \times I^1_{\mathrm{gauabs}} \cdot I^2_{\mathrm{gauabs}} \tag{3.40}$$

Which describes a photoabsorbed continuum, superposed by two Gaussian absorption lines, one to take care for the CRSF, the other to model a yet unexplained feature at $\sim$10 keV. The constant C is needed, as spectra from two different instruments, namely JEM-X and ISGRI were used. The calibration between these instruments is inconsistent, so that slightly different absolute fluxes are measured. All other parameters of the model spectrum are the same for both instruments. The photoabsorption takes care for the decline at lower energies, as soft X-rays can be absorbed by the surrounding medium via photoionization. The optical thickness of the column, N_{H}, between the source and the observer is measured in units of 10^{22} hydrogen atoms cm^{-2}. The photoionization cross-section σ_{bf} is a strong function of the photon energy with $\sigma_{\mathrm{bf}} \sim E^{-3}$, so that the model can be written as

$$I_{\mathrm{phabs}}(E) = \exp\left(-N_{\mathrm{H}}\sigma_{\mathrm{bf}}(E)\right) \tag{3.41}$$

The continuum can be described by a powerlaw with a Fermi-Dirac-cutoff. The powerlaw dominates the overall shape of the spectra, but to model it accurately a cut-off at high energies is needed. Kretschmar et al. (1997a) point out that it is important to use a smooth transition between the powerlaw and the cutoff to model all lines correctly. A smooth transition is achieved with the Fermi-Dirac-Cutoff model (Tanaka, 1986). This common model component can be written as:

$$I_{\mathrm{cont}}(E) = AE^{-\Gamma} \cdot \frac{1}{1 + e^{(E - E_{\mathrm{cut}})/E_{\mathrm{fold}}}} \tag{3.42}$$

where Γ is the photoindex of the powerlaw, A the norm, E_{cut} is the so-called cut-off energy and E_{fold} the folding energy. The Gaussian absorption lines are modeled via the local "gauabs" model of XSPEC (see Suchy et al., 2008, and references therein). It is a Gaussian line profile at the energy E_{gauabs} with a width of σ_{gauabs} and a depth τ:

$$I^i_{\mathrm{gauabs}}(E) = \exp\left(-\frac{\tau}{2\pi\sigma_{\mathrm{gauabs}}} e^{\left(E - E_{\mathrm{gauabs}}\right)^2 / 2\sigma_{\mathrm{gauabs}}}\right) \tag{3.43}$$

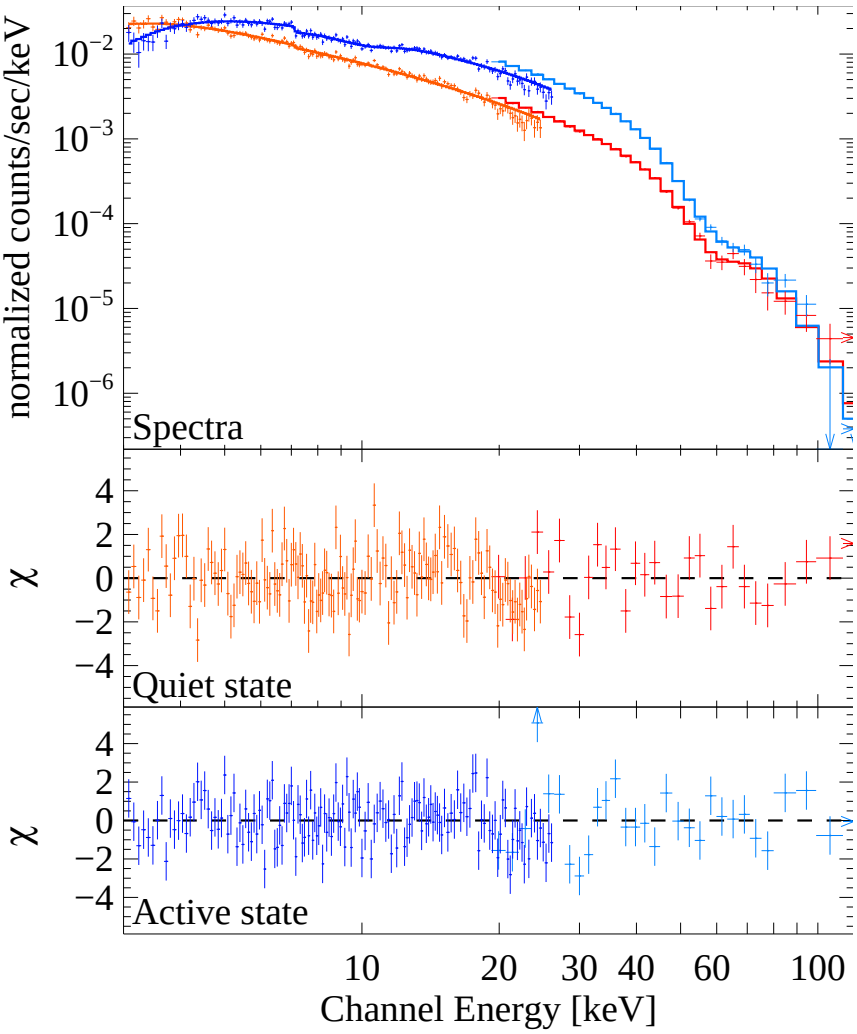

Figure 3.5.17: Spectra combined of JEM-X and ISGRI data. The blue spectrum shows the active state, the red one the quiet state. The second and third panel are the according residuals.

The unfolded spectra and the fitted models are shown in Fig. 3.5.17, the according fit parameters in table 3.5.4 for the quiet state and in table 3.5.5 for the active state. The left part of the spectra is extracted using JEM-X from 3.0 keV to 26.5 keV, the harder part to the right emerges from ISGRI data between 19.0 keV and 130.0 keV. The fundamental CRSF feature could not be detected in the data, allthough Schanne et al. (2007) state that is is apparent in at least part of the data. I ascribe the failure of detection to the fact that in the corresponding energy range at about 25 keV both instruments are not perfectly calibrated. It is the upper limit of JEM-X and the lower limit of ISGRI. At this intersection point every line detection should be

Table 3.5.4: The fitparameters of the quiet spectra shown in red in Fig. 3.5.17. The spectra were modeled for JEM-X and ISGRI data simultaneously. As explained, the constant factor takes care of the different calibration of the two instruments. To calculate the correct values for JEM-X the model as to be multiplied by the constant. Only one `gauabs` line is included in the model, as a second one at ∼10 keV did not improve the fit any further. Underlined is the photo index of the powerlaw, which is discussed in the text.

Model	Parameter	Value	Uncertainty
phabs	N_{H}	4.41	± 1.1
powerlaw	photo index	<u>1.304</u>	$\begin{cases} +0.077 \\ -0.089 \end{cases}$
powerlaw	norm	0.231	$\begin{cases} +0.030 \\ -0.026 \end{cases}$
fdcut	cut-off energy(keV)	23.5	$\begin{cases} +5.1 \\ -7.5 \end{cases}$
fdcut	folding energy (keV)	14.8	$\begin{cases} +1.7 \\ -1.5 \end{cases}$
gauabs	E_{gauabs} (keV)	58.3	$\begin{cases} +2.6 \\ -1.9 \end{cases}$
gauabs	sigma keV	7.4	$\begin{cases} +1.7 \\ -1.4 \end{cases}$
gauabs	depth	0.95	$\begin{cases} +0.22 \\ -0.18 \end{cases}$
constant	factor	1.17	±0.029

Table 3.5.5: Same as tab. 3.5.4, but for the active spectra and with an additional `gauabs` line, which models the 10 keV feature.

Model	Parameter	Value	Uncertainty
phabs	N_{H}	10.2	±1.5
powerlaw	photon index	<u>0.964</u>	$\begin{cases} +0.078 \\ -0.089 \end{cases}$
powerlaw	norm	0.200	$\begin{cases} +0.034 \\ -0.030 \end{cases}$
fdcut	cut-off energy (keV)	23.5	$\begin{cases} +2.6 \\ -3.5 \end{cases}$
fdcut	folding energy (keV)	11.30	$\begin{cases} +0.86 \\ -0.73 \end{cases}$
gauabs	E^1_{gauabs} (keV)	58.6	$\begin{cases} +1.8 \\ -1.5 \end{cases}$
gauabs	sigma^1 (keV)	8.29	$\begin{cases} +1.2 \\ -1.1 \end{cases}$
gauabs	depth^1	1.04	$\begin{cases} +0.20 \\ -0.16 \end{cases}$
gauabs	E^2_{gauabs} (keV)	10.15	$\begin{cases} +0.32 \\ -0.34 \end{cases}$
gauabs	sigma^2 (keV)	1.35	$\begin{cases} +0.47 \\ -0.37 \end{cases}$
gauabs	depth^2	0.152	$\begin{cases} +0.035 \\ -0.031 \end{cases}$
constant	factor	1.284	±0.025

taken with great care. Furthermore Kreykenbohm et al. (2002) have shown that the depth of the CRSF is a strongly depending on pulse phase. As I averaged over the complete pulse and did not perform phase-resolved spectroscopy it is not unexpected to miss the fundamental line. The second and third panel of Fig. 3.5.17 show the respective residuals as reduced χ^2 value. As can be clearly seen in Fig.3.5.17 and in tables 3.5.4 and 3.5.5, where the values are underlined, the photo index of the quiet state is about 1.5 times the one of the active state. This means that less photons

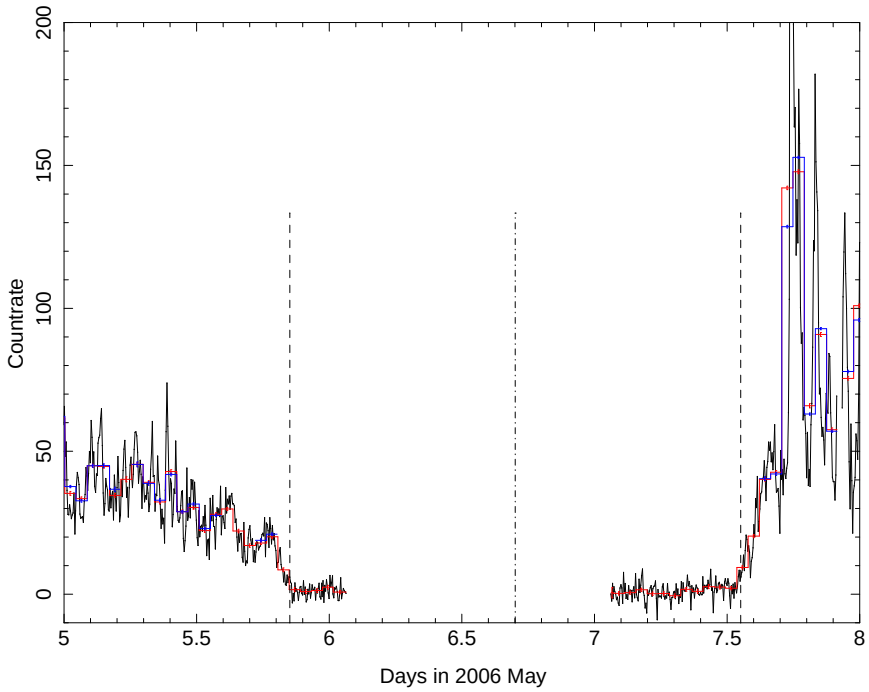

Figure 3.5.18: Lightcurve in the 20–60 keV band around the eclipse of 2006 May 6. The colors represent the same ways of extracted lightcurves as in Fig. 3.5.13.

were Comptonized to high energy in the accretion column of the neutron star (see Sect. 3.1.3). Additionally, as the object absolute brightens, more material must be accreted. This might lead to a higher absorption coefficient, which then means that the photons are either emitted or absorbed before they can be scattered to high energies. This would explain the effect that the spectrum softens while Vela is getting brighter. Additionally, in the active state, the N_{H} value of the photoabsorption is higher, which is a direct effect of more material in the vicinity of the neutron star. The energy and the shape of the CRSF does not change within the uncertainties, so that an influence of the magnetic field on the shape of the spectrum can be ruled out.

3.5.2 Eclipses

The duration and location of the eclipses in the lightcurve of a binary system allow a good instrument for determining the orbit parameters. When eclipses are seen the inclination i can be restricted to large values. Through the duration of the eclipse, hints on the size of the optical companion and the orbit are given. Vela X-1 shows relativly long eclipses of about 1.70d (Kreykenbohm et al., 2008). During this eclipse no relevant X-rays are measured by ISGRI. This lack of radiation is easily explained,

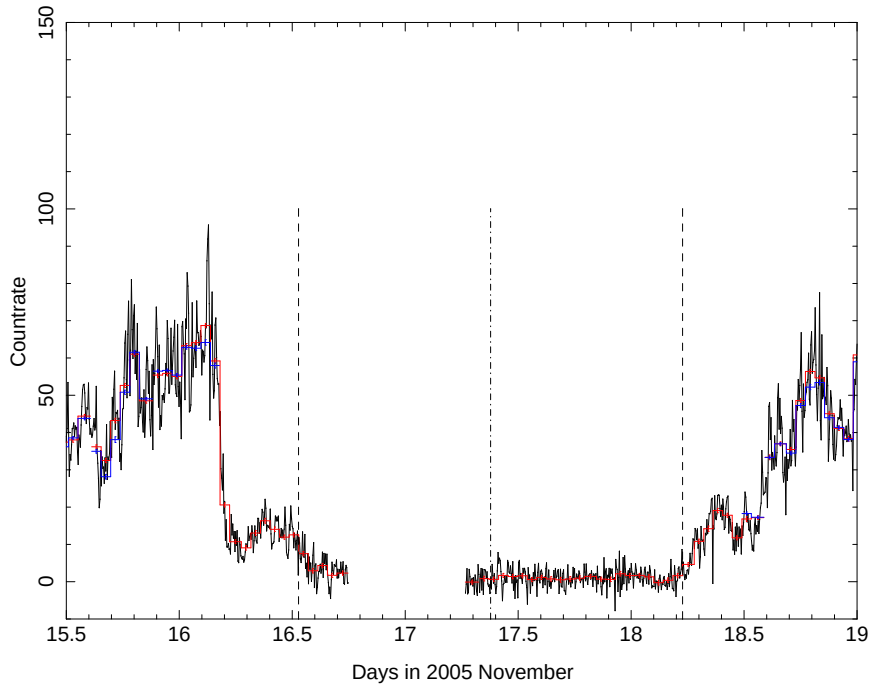

Figure 3.5.19: Lightcurve in the 20–60 keV band around the eclipse of 2005 November 17. The colors represent the same ways of extracted lightcurves as in Fig. 3.5.13. Note the apparent humps shortly before and after the eclipse, which are not visible in Fig. 3.5.18.

as the X-rays are produced very close to the neutron star and the res supergiant is of course impenetrable for even the most energetic X-rays. The star itself on the other hand is too cool to produce any measurable X-rays in the energy band of ISGRI (see Chap. 1). The atmosphere and the wind of the optical companion are almost completely transparent for X-rays above 20 keV, so that an almost sudden disappearance of the X-ray radiation is expected, as soon as the neutron star moves behind the star itself. This can be seen in Fig. 3.5.18, showing the lightcurve in the 20–60 keV band during the eclipse around 2006 May 6. The dotted lines represent the beginning, center and end of the eclipse calculated with the ephemeris data from Kreykenbohm et al. (2008). The ingress into eclipse happens in a relatively quite state, so that the transition is rather smooth. In contrary, after the egress Vela X-1 is very bright and active so that the countrate rises steeply. It is can be assumed that Vela transited into the active phase while in eclipse and invisible to us.

Fig. 3.5.18 shows a common eclipse. In the data I analyzed, 7 eclipses are visible (compare Figs. 3.5.13, 3.5.14 and 3.5.15). Most of them do look very similar. Fig. 3.5.19 allthough shows an eclipse in November 2005, which shows very characteristic

humps before the beginning and after the end of the eclipse. The countrate drops by about factor 5 shortly before the eclipse. With that low countrate, the standard pipeline could not find Vela X-1 in on single ScW anymore, and thus no data for *ii_light_extract* in blue is given during these phases in Fig. 3.5.19. The lines mark the beginning, center and end calculated with the same ephemeris data as in Fig. 3.5.18, where they fit very accurately. In all other eclipses, the ephemeris data is correct, too. A mistake in the calculated timing of the eclipse can thus be ruled out. Both, before ingress and after egress Vela X-1 is in a very active state. The sudden drop and the rim of the eclipse is so very unlikely to be due to the characteristic flaring behavior. One possible explanation might be a drastically increased absorption in the trailing accretion stream. The composition of the accretion stream must have changed notably to explain an increased absorption, as the photoionisation cross-section for X-rays above 20 keV is very small. The absorption could also be due to Thomson scattering, which plays an important role when N_{H} is distinctly larger than 10^{24}. The humps might be also due to a change in the atmosphere of the optical companion. It might be possible that a large flare or clump of material is emerging from the star, and thus occulting the neutron star. Note however, that this clump must be extraordinarily thick to absorb the strong X-ray emission from the active Vela X-1. To fully understand how the configuration of the Vela system changed during that eclipse, more observations of eclipses are necessary. The observations should also be done with other instruments, which provide higher timing resolution and different energy bands.

3.5.3 Flaring behavior

Kreykenbohm et al. (2008) measured giant flares during their observeration of Vela, which are evident in Fig. 3.5.13, too. To understand if such giant flares are explainable by the same physical process as the other, common flares in Vela X-1, I analyzed the flaring behavior for the whole data. The flares of Vela have typical duration of some hours. To get a good coverage of these flares, the chosen temporal resolution of 283.5 sec is fine. The lightcurve data were binned logarithmically into 256 countrate bins after eliminating all datapoints which are measured during the eclipse of Vela X-1. Fig. 3.5.20 shows the histogram for the whole 20–60 keV band. The solid line is a Gaussian fitted to the data, representing a log-normal distribution. The fit parameters can be found in table 3.5.6.

The Figs. show that the flaring follows closely a log-normal distribution. Even though the system is quite different, it is interesting to note that Uttley & McHardy (2001) for short time-scales and Poutanen et al. (2008) for long time-scales found a similar log-normal distribution when analyzing the flaring behavior of Cygnus X-1. These results were confirmed by Gleissner et al. (2004). Uttley et al. (2005) modeled this

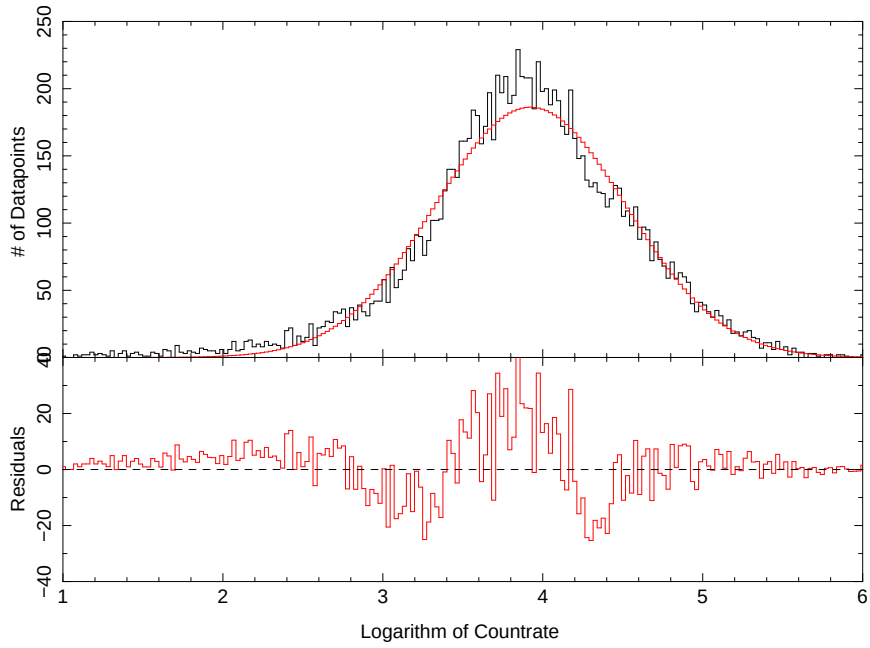

Figure 3.5.20: Histogram of the lightcurve of the 20–60 keV band, binned to 256 bins. The red curve shows the best fit single Gaussian. Fit values are shown in tab. 3.5.6

behavior by taking the exponential function of a linear, aperiodic lightcurve. Such a linear, aperiodic lightcurve can be achieved by adding a large number of sine-waves with randomly distributed amplitudes A_i, frequencies ν_i and phases φ_i, where the root distribution follows a normal distribution. The emerging lightcurve $x(t)$ can thus be written as

$$x(t) = \exp\left(\sum_{i=0}^{\infty} A_i \sin(2\pi\nu_i t + \varphi_i)\right) \tag{3.44}$$

In taking the exponential function of this lightcurve, a non-linear term is introduced. This is intrinsically log-normal distributed, as the $x(t)$ are normal distributed. Uttley et al. (2005) could show that with that model the lightcurve of Cygnus X-1 could be represented quite well. As the distribution of the flares in Vela X-1 looks quite similar, this should be true for Vela, too. This will be analyzed in a future work.

Even if the log-normal distribution is a rather good description of the histogram, small offsets at especially high and low countrates are apparent in Fig. 3.5.20. This means that the process is not produced by completely multiplicative components, but small additive components must play a not-negligible role. To improve the fit, two additional Gaussians where added to the fit. Their parameters are also found in table 3.5.6. This improves the fit drastically, as seen in Fig. 3.5.21. It is difficult to

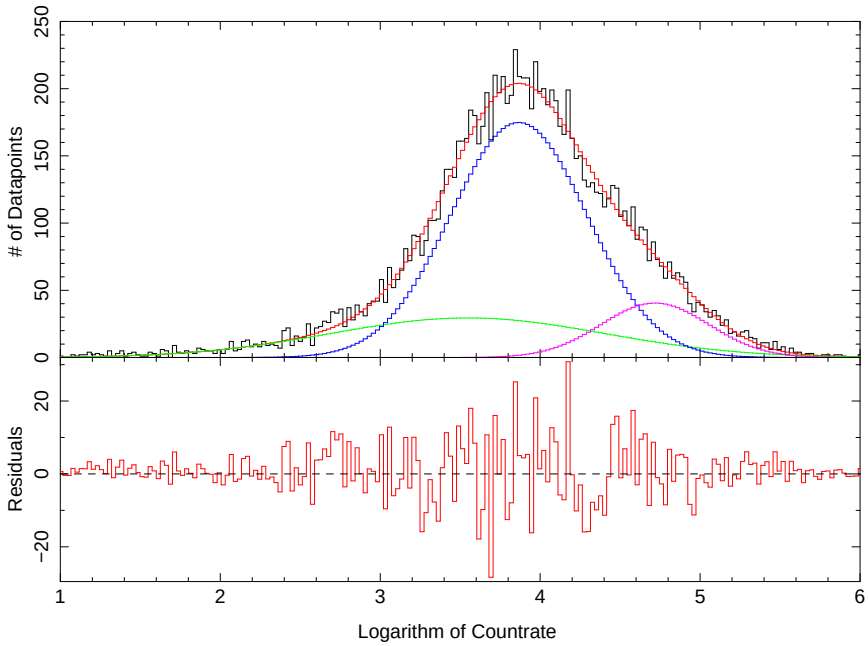

Figure 3.5.21: Histogram of the lightcurve of the 20–60 keV band, binned to 256 bins. The red curve shows the best fit consting of 3 Gaussians. The blue curve shows the Gaussian #1, the violet one Gaussian #2 and the green one Gaussian #3, as in tab. 3.5.6

measure the improvement in terms of χ^2, as the uncertainties of the histogram can not be calculated analytically. Uttley et al. (2005) presumed a Poisson-statistic for every single bin and took the square root of the events per bin as their error. This is only statistcally valuable with about 100 or more events per bin. In our data, this is not the case for the most bins. I therefore refrain from using χ^2 values to describes the goodness of the fit. Instead I calculated histograms for theoretical datapoints, which were calculated by adding or subtracting the uncertainties of the data.

$$F_{\max}(t) = \text{data}(t) + \text{error}(t) \tag{3.45}$$
$$F_{\min}(t) = \text{data}(t) - \text{error}(t) \tag{3.46}$$

The histograms of $F_{\max}$ and $F_{\min}$ thus give extreme values for each single histogram bin. Of course, the difference in each single bin between rate plus error and rate minus error is not an error representing any confidence range for the measured countrate in that bin. These histograms were also fitted with three independent Gaussians. This fit smooths out the extreme variations and gives a hint about the variance of the histograms. Fig. 3.5.22 shows these fits together with the data without errors. As can be clearly seen, the blue and green curve envelops the measured data well. This

Table 3.5.6: The fitparameters of the Gaussian log-normal fits to the binned lightcurve in the 20–60 keV band. The upper part corresponds to Fig. 3.5.20, the lower part to Fig.3.5.6.

Parameter	Value	Uncertainty
gauss(1).area	11000	±170
gauss(1).center	3.9228	±0.0094
gauss(1).sigma	0.5979	±0.0078
gauss(1).area	7400	$\begin{cases} +950 \\ -1200 \end{cases}$
gauss(1).center	3.867	$\begin{cases} +0.032 \\ -0.053 \end{cases}$
gauss(1).sigma	0.43	$\begin{cases} +0.50 \\ -0.19 \end{cases}$
gauss(2).area	1300	$\begin{cases} +940 \\ -470 \end{cases}$
gauss(2).center	4.72	$\begin{cases} +0.10 \\ -0.16 \end{cases}$
gauss(2).sigma	0.337	$\begin{cases} +0.064 \\ -0.046 \end{cases}$
gauss(3).area	2500	$\begin{cases} +760 \\ -650 \end{cases}$
gauss(3).center	3.547	$\begin{cases} +0.096 \\ -0.165 \end{cases}$
gauss(3).sigma	0.857	$\begin{cases} +0.073 \\ -0.067 \end{cases}$

means they are good estimates for the underlying statistical variance. To quantify this result, I calculated the percentile difference D between the two new fits compared to the values of the standard one.

$$D = \frac{|F_{\max} - F_{\min}|}{F} \cdot 100 \tag{3.47}$$

As can be seen in the lower panel of Fig. 3.5.22 this difference is in the main part below 20%, which puts confidence in the chosen binning and fit. The average value of D is $|D| \approx 137\%$. Additionally the overall shape of the fit functions of only the data, the data plus error and the data minus error is very much the same, so that the drawn conclusions are independent of the chosen histogram.

Obviously the main part of the flaring behavior can be explained by a log-normal distribution, but especially the most active states require another log-normal distribution to be modelled accordingly. The probability to measure extremely bright flares with more than 300 counts $\sec^{-1}$ in the 20–60 keV band is with one Gaussian ∼0.10%, while when using 3 Gaussians it is ∼0.16. This is a rather small number but far from impossible, so that I can conclude that bright flares are rare but not once-in-a-lifetime events.

A fit with three independent Gaussians was also done for the logarithmic binned lightcurves of the soft 20–30 keV band and the hard 40–60 keV band, see figs. 3.5.23 and 3.5.24. The fit parameters are listed in tables 3.5.7 and 3.5.8 respectively. It is seen that Gaussian #2, describing the brighter part of the distribution is even more pronounced in the data of the soft band than in the data for the overall band. On

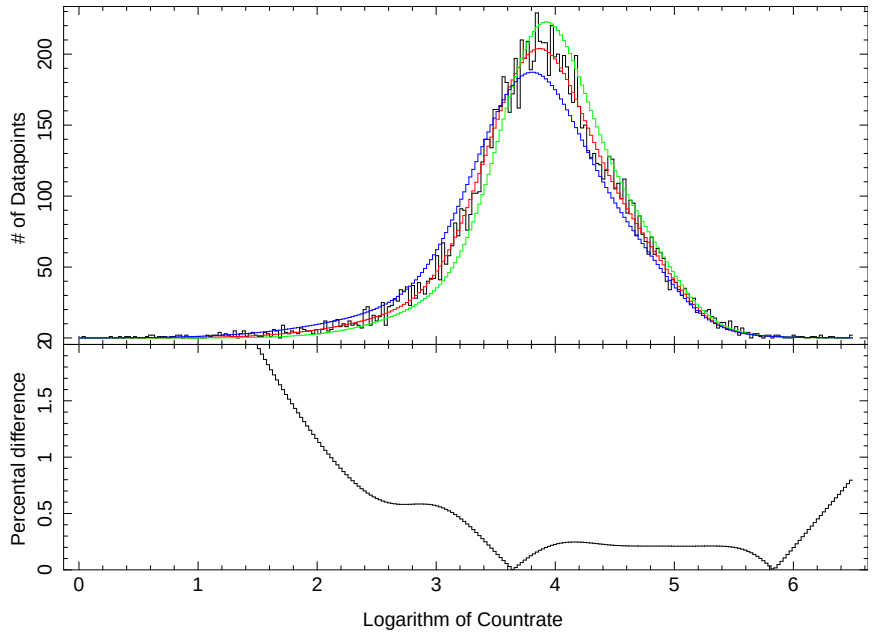

Figure 3.5.22: Histogram of the lightcurve of the 20–60 keV band, binned to 256 bins. The red curve shows the best fit consting of 3 Gaussians. The blue curve shows the best fit for the data minus its error, the violet the best fit for the data plus its error. In the lower panel the absolute value of percental difference as is plotted.

the other hand, no Gaussian is needed to model the active end of the histogram for the hard band. Even more, the main Gaussian #1 models the distribution almost perfectly, so that the other two are very small. Gaussian #3 is in all fits responsible for the quiet end continuum and is not changing much in its width, only its overall strength is less pronounced in the hard band. To compare the peak values of the Gaussian, on has to keep in mind that because of the power-law-like spectrum of Vela X-1 the hard band intrinsically has lower countrates than the soft band. Assuming a factor of Soft / Hard of about 5.6 one has to add to the center value of the Gaussians of the hard band a value of $\log(5.6) = 1.73$ to receive the center values of the Gaussians of the soft band. This approximation would lead for the main Gaussian #1 to a value of ~ 3.7, which is near the actual measured value.

To compare my findings to more measurements I looked at data from the All-Sky Monitor aboard *RXTE*. The ASM is described in Sect. 2.1.3. The ASM performs 90 min dwells on a irregular basis onto Vela X-1. This provides us with a good statistic of Vela in the 2–10 keV range. I performed the same analysis of the ASM data as of the ISGRI data, with binning the logarithm countrate to 256 after removing datapoints in the eclipse. A model of three individual Gaussians was then fitted to

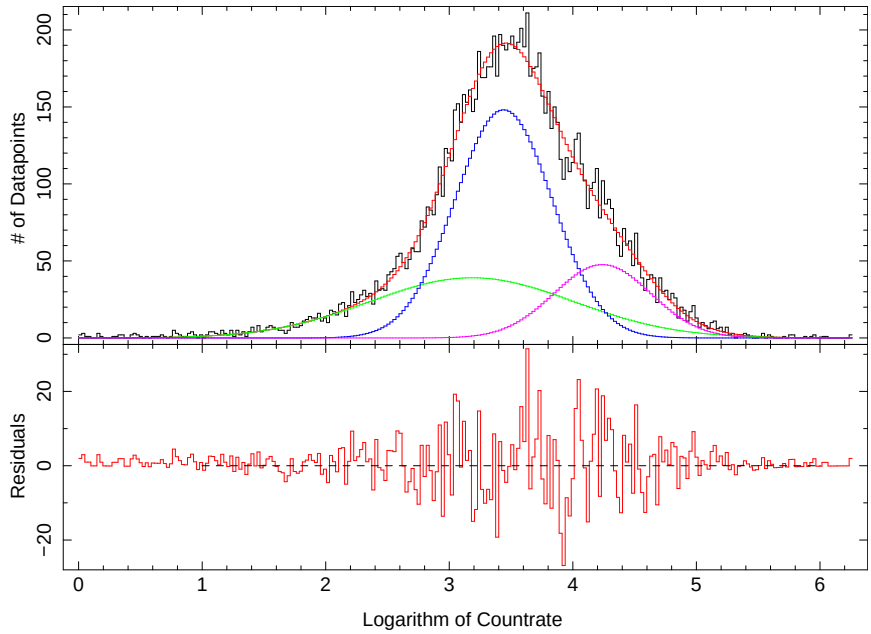

Figure 3.5.23: Histogram of the lightcurve of the 20–30 keV band, binned to 256 bins. The red curve shows the best fit consting of 3 Gaussians. The blue curve shows the Gaussian #1, the violet one Gaussian #2 and the green one Gaussian #3, as in tab. 3.5.6

Table 3.5.7: The fitparameters of the Gaussian log-normal fits to the binned lightcurve of the soft 20–30 keV band, see Fig. 3.5.23

Parameter	Value	Uncertainty
gauss(1).area	6000	$^{+1200}_{-1800}$
gauss(1).center	3.440	$^{+0.049}_{-0.077}$
gauss(1).sigma	0.394	$^{+0.046}_{-0.047}$
gauss(2).area	1900	$^{+1800}_{-750}$
gauss(2).center	4.24	$^{+0.15}_{-0.25}$
gauss(2).sigma	0.392	$^{+0.098}_{-0.064}$
gauss(3).area	3300	$^{+840}_{-890}$
gauss(3).center	3.183	$^{+0.095}_{-0.213}$
gauss(3).sigma	0.823	$^{+0.059}_{-0.065}$

the data. The parameters of the fit can be found in table 3.5.9. The 2–10 keV range is clearly softer than the soft band of ISGRI so that a even stronger bright excess would be expected. As can be seen in Fig. 3.5.25 however, no bright excess is measured. Even more, the second Gaussian, responsible for modelling the bright excess in the *INTEGRAL* data has vanished completely. One possible explanation for this behavior

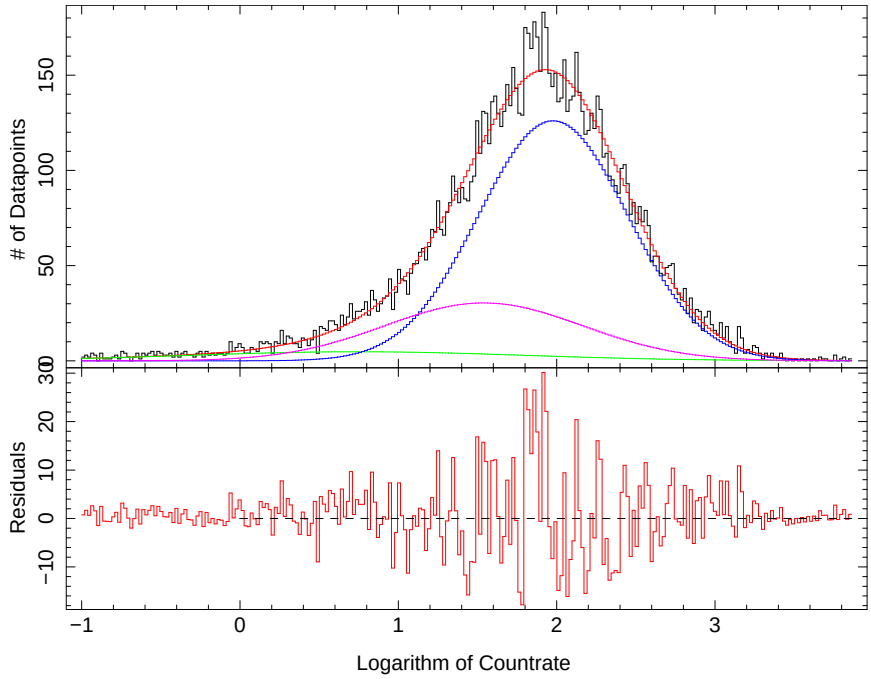

Figure 3.5.24: Histogram of the lightcurve of the 40–60 keV band, binned to 256 bins. The red curve shows the best fit consting of 3 Gaussians. The blue curve shows the Gaussian #1, the violet one Gaussian #2 and the green one Gaussian #3, as in tab. 3.5.6

Table 3.5.8: The fitparameters of the Gaussian log-normal fits to the binned lightcurve of the hard 40–60 keV band, see Fig. 3.5.24

Parameter	Value	Uncertainty
gauss(1).area	9800	$^{+430}_{-1}$
gauss(1).center	1.922	$^{+0.013}_{-8.0^{-11}}$
gauss(1).sigma	0.498	$^{+0.011}_{-0.012}$
gauss(2).area	140	$^{+111}_{-63}$
gauss(2).center	0.746	$^{+0.077}_{-0.295}$
gauss(2).sigma	0.124	$^{+0.092}_{-0.043}$
gauss(3).area	1100	$^{+430}_{-440}$
gauss(3).center	0.89	$^{+0.26}_{-0.44}$
gauss(3).sigma	0.88	$^{+0.12}_{-0.20}$

would be that the photo-absorption in the active state is drastically increased. As the cross-section of the photo-absorption is declining fast with increasing energy, X-ray photons of about 20 keV are only slightly absorbed. On the other hand, the 2–10 keV photons are strongly absorbed. The increased absorption can be clearly seen in the

Table 3.5.9: The fitparameters of the Gaussian log-normal fits to the binned lightcurve of the 2–10 keV band of the ASM aboard RXTE, see Fig. 3.5.25

Parameter	Value	Uncertainty
gauss(1).area	9800	$\begin{cases} +430 \\ -1 \end{cases}$
gauss(1).center	1.922	$\begin{cases} +0.013 \\ -8.0e{-}11 \end{cases}$
gauss(1).sigma	0.498	$\begin{cases} +0.011 \\ -0.012 \end{cases}$
gauss(2).area	140	$\begin{cases} +110 \\ -63 \end{cases}$
gauss(2).center	0.746	$\begin{cases} +0.077 \\ -0.295 \end{cases}$
gauss(2).sigma	0.124	$\begin{cases} +0.092 \\ -0.043 \end{cases}$
gauss(3).area	1100	$\begin{cases} +430 \\ -440 \end{cases}$
gauss(3).center	0.89	$\begin{cases} +0.26 \\ -0.44 \end{cases}$
gauss(3).sigma	0.88	$\begin{cases} +0.12 \\ -0.19 \end{cases}$

spectrum in Fig. 3.5.17. This means, even though the flares could be brighter in the soft band they are not measureable, because the X-rays can not penetrate the surrounding medium anymore. A higher absorption in the active states can easily be explained, as more material is accreted onto the neutron star, which means that it moves through denser parts of the stellar wind. Another reason that no bright excess can be seen in the histogram of the ASM might be the inadequate sampling rate of the ASM. Staubert et al. (2004) have shown that flares which were clearly visible in *INTEGRAL* data do not show up in the ASM data. Even more, the ASM erroneously detects fluxes of the order of the flaring fluxes while Vela was in eclipse (Kreykenbohm et al., 2008). This even more reduces the trust which should be put into the histogram of the ASM data.

We already noted that brighter parts of the lightcurve are softer. This goes well with the observation that the second Gaussian is vanishing in the bright part of the histogram for the high band, while it is undoubtedly clear in the soft band. This result could mean that two different physical processes are at work when producing the X-rays of Vela X-1. One process is responsible for the most of the variability, having the same strength in all energy bands. This could be due to small variations in the accretion stream, without changing the overall configuration of the system. The other process just produces soft X-rays, but with distinctly higher countrates. This process is not so common as the first one. It might be explained by extreme increased accretion which than increases the optical depth in the accretion column dramatically. As explained above, this would lead to a softer spectrum. Much more work on this topic is necessary to understand the physical processes.

Another approach in analyzing the flaring behavior of lightcurve is to use Bayesian Blocks (Scargle, 1998). In simple words, this algorithm tries to find sections of about the same countrate, which are as long as possible. This means, a quiet phase in the

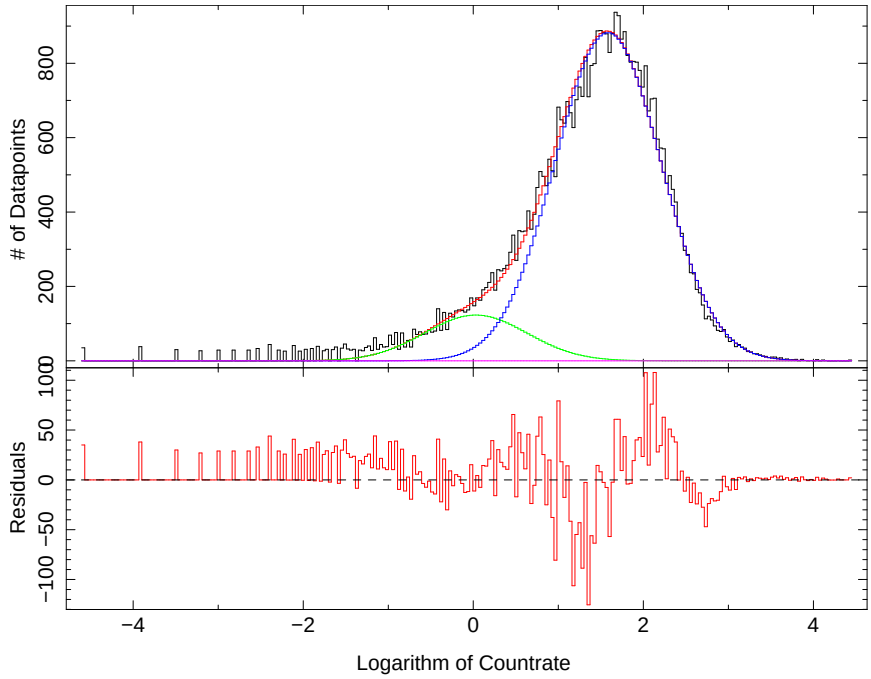

Figure 3.5.25: Histogram of the lightcurve of the ASM of *RXTE* in the 2–10 keV band, binned to 256 bins. The red curve shows the best fit consting of 3 Gaussians. The blue curve shows the Gaussian #1, the violet one Gaussian #2 and the green one Gaussian #3. Gaussian # 2 as vanished completely and the bright flank is perfectly modelled with only one Gaussian.

countrate would result in a long, constant block. A flare on the other hand would bring a short block. The countrate of the block represents the average countrate of the lightcurve during the period the block spans. The Bayesian Blocks as a whole are thus a kind of smoothed lightcurve which can be binned and worked into a histogram in the same way as the normal lightcurve. To apply the Bayesian Blocks technique to my data I used ISIS scripts provided in the SITAR package by Michael Nowak[4]. These scripts require to give a parameter `ncp`, representing the prior probability for the number of blocks. The significance level of each detected block can than be calculated as $1 - \exp(-\texttt{ncp})$. This is only a unprecise approximation. In our case, this approximation seems to fail miserably, as the value of `ncp` has to be set to `ncp` $= 3{\cdot}10^{-5}$ which represents a significance of about the same value. This is an unrealistic low value and more investigations on this approximation will be done. A example of the lightcurve and the respective Bayesian Blocks is given in Fig. 3.5.26. This time range shows characteristically the different active and quiet phases of Vela X-1, as well as a eclipse. As can be seen, in the eclipse many different blocks were found. This can

[4] `http://space.mit.edu/cxc/analysis/SITAR/`

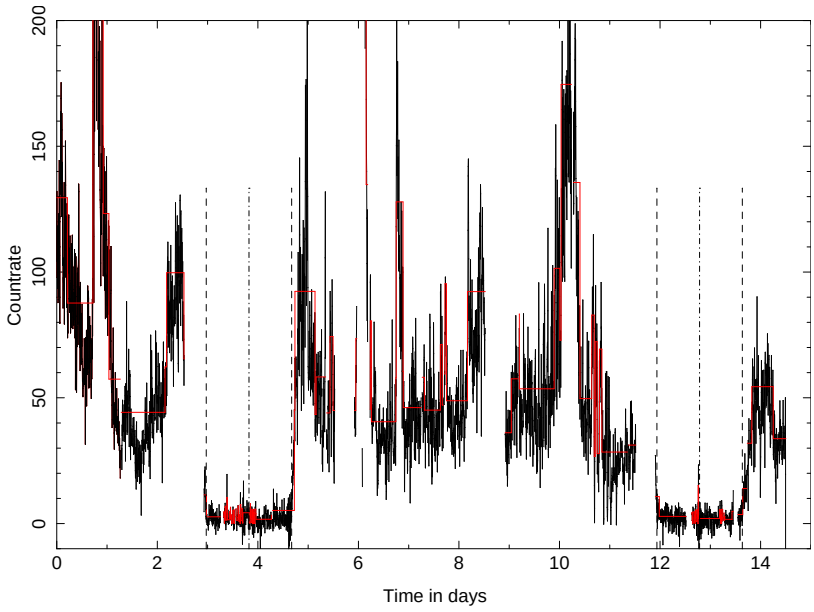

Figure 3.5.26: Lightcurve in the 20–60 keV band with superimposed the respective Bayesian Blocks.

be ascribed to the fact that in the eclipse the countrates are compatible with zero and the overlying Poisson noise is producing large fake flares. This leads the algorithm to construct many individual blocks.

Outside the eclipse only 184 different blocks were found Even with the low `ncp` value. This is hardly enough to have a good statistic. Nonetheless, the histograms follows a log-normal distribution, as can bee seen in Fig. 3.5.27. A fit with three individual Gaussians is not sensible to this inaccurate data. Hopefully more data of Vela X-1 will be accumulated in the next few years, so that the statistics can be improved further.

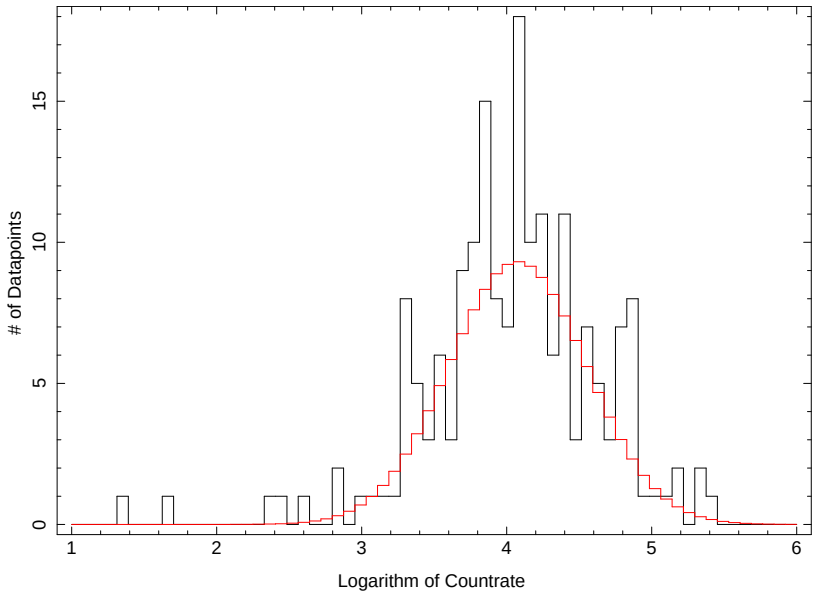

Figure 3.5.27: Histogram of the Bayesian Blocks calculated out of the lightcurve in the 20–60 keV band. As only very few blocks were found, the data looks quite noisy. The red curve is the best fitted Gaussian to the data.

3.6 Summary and conclusion

I have presented data of Vela X-1 taken with ISGRI and JEM-X aboard *INTEGRAL*. Overall about 3 Msec of data were analyzed. Lightcurves in the energy bands 20–30keV, 20–60 keV and 40–60 keV were extracted. The lightcurves were extracted using two different routines, namely *ii_lc_extract* and *ii_light*. I have shown that the both routines produce very similar lightcurves. In the lightcurve, different states of Vela X-1 are apparent. There are time-periods, where Vela X-1 is very quiet and the overall brightness is low. At these times the hardness-ratio is usually harder. At other times Vela X-1 shows strong flaring behavior and is overall brighter. This brightening goes along with a softening of the spectrum. The softening in the bright states can be explained with a theory proposed by Becker & Wolff (2007). In this theory, when more mass is accreted, e.g, the luminosity is higher, the optical depth of the accretion column is higher, too. This means that thermal photons do not stay long enough in the accretion column to be Comptonized to high energies. Only photons with lower energies, e.g., softer photons can escape. n the momentary extracted spectra, using combined data from JEM-X and ISGRI, the aforementioned change in hardness is visible, too. In this spectra a possible higher absorption coefficient in the active state is visible. To probe this theory, more spectra in different states need to be extracted and checked for changes in the absorption. In momentarily extracted spectra only

one CRSF is visible at $\sim$ 58 keV. The fundamental line at $\sim$ 25 keV could not be detected. Here a phase-resolved spectroscopy, as done by Kretschmar et al. (1997b) might help to detect the line. In phase-resolved spectroscopy spectra over many pulses are averaged, but only spectra for part of the averaged pulses are extracted. The number of pulses which are averaged should be chosen with respect to accumulate enough counts for the spectra but without adding up pulses from different states. An analysis of phase-resolved spectra for the different states will be presented in a future work.

The lightcurves were given a closer look in the region of the eclipses. Through the behavior around the eclipses, information about the stellar atmosphere of the optical companion and the accretion wake of the neutron star can be gained. I have found that most eclipses show a rather sudden egress and ingress. One eclipse however was found, which exhibits characteristic humps shortly before and after the main eclipse. In these humps the countrate drops dramatically and rises slightly again before the neutron star vanishes behind its optical companion. No thorough explanation can be given for this behavior, allthough a optical thick blob in the stellar wind might be a possible explanation. Data from other satellites, providing different energy ranges will be used to analyze the effect and to draw further conclusions.

The data of the extracted lightcurve were binned into histograms. All 3 Msec data were used, excluding the eclipses, to have the best possible statistic. I have shown that the histograms follow a log-normal distribution. In the soft band, the fit could be drastically improved, when modelling three independent log-normal distributions. Especially in the brighter part of the histogram an additional Gaussian models a bright excess very well. This bright excess can be related to the softening of the spectrum in active states. This means, the bright and soft parts of the spectrum seem to be produced by another process, which is additive to the process producing the standard brightness of Vela X-1. Log-normal distributions are calculated via the product of many independent random variables. Uttley et al. (2005) have shown that the lightcurve of Cygnus X-1 can be explained by multiplying different, randomly distributed sine waves. This model should be applicable for the flaring behavior of Vela X-1, too. In the soft band, the model should be adjusted by allowing for the addition of another model lightcurve, itself consisting of the multiplication of independent sine waves. The direct physical implications of this model are not clear yet, but it shows that different multiplicative processes could be at work in producing the luminosity of Vela X-1. The irregularity in the flaring of Vela X-1 can be physically explained by a clumped stellar wind of the optical companion (Walter & Zurita Heras, 2007). The clumping of wind from hot stars is a field of intense research, see, e.g, Hamann et al. (2008). If the clumps would be distributed following a log-normal distribution, the shape of the countrate histogram would be apparent. However no such evidence has been brought up yet. The scenario of a clumped stellar wind would connect Vela X-1 to the newly discovered group of "Supergiant Fast X-Ray Transients"

(SFXTs). SFXTs are systems, consisting of a neutron star and a supergian optical companion, but contrary to Vela X-1 are not persistent. The flares of SFXTs can reach up to 1000 times the brightness as in the quiescence states. The main difference between Vela X-1 and the SFXT group might be that in SFXT-systems the neutron star as a larger orbit around the star. The density of the wind is declining with increasing radius and so SFXT can only accrete enough material to be visible, when a large clump is encountered. Vela X-1 on the other hand is close enough to the supergiant that almost at all times material is accreted. The spectra of SFXT and Vela X-1 look quite similar so that most likely the same physical processes are at work. To put the histograms of the lightcurve extracted from ISGRI data into context, I analyzed the lightcurve of the ASM aboard *RXTE* in the same way. The ASM is sensitive at lower energies than ISGRI an thus opens another energy band. No bright excess could be measured in the ASM histogram. I ascribe this to the fact, the the absorption in the active states is higher, and the soft X-rays the ASM measures are absorbed before they reach the Earth.

To analyze the flaring behavior more closely, other statistical tests need to be done. Uttley et al. (2005) have shown that with a log-normal distribution of the countrate, a linear RMS-flux correlation emerges. This could be a good test if the flaring behavior of Vela X-1 can be explained with the same model as the on of Cygnus X-1. Furthermore, a Fourier-transformation of the lightcurve should be analyzed. As the lightcurve is not taken continuously and are irregularly spaced, a Lomb-Scargle (Lomb, 1976) transformation must be done to construct a correct power-spectral density (PSD) diagram. These test will be performed in a future work.

Concluding one can say that the statistical analysis of the archival Vela X-1 data as proven to be really useful to analyze the flaring behavior. Different states of the system require for different explanation and the system must be put into context with other similar systems like SFXTs. Considering this, the available data can be analyzed more thoroughly, but more detailed spectra and timing data would prove useful to understand the physical properties of the system.

A dwarf standing on the shoulders of a giant
may see farther than a giant himself.

(Robert Burton, "Anatomy of Melancholy", 1621)

4 Conclusion and Outlook

MANY more things could be said about the two topics which were covered in this diploma thesis. Most of it will, however, require more detailed work, which will be carried out in the following dissertation. Here I will briefly summarize the findings in this work and give an outlook to the future work. See Sects. 2.4 and 3.6 for detailed discussions.

In Chap. 2 I have shown detailed measurements of the region of increased particle background known as the "South Atlantic Anomaly". With data taken by the particle monitor of the HEXTE instrument aboard the "Rossi X-Ray Timing Explorer" (*RXTE*) it was possible to cover 11 years of constant monitoring of this region. The resolution of the extracted data was 0.5 deg in latitude, 0.25 deg in longitude, and 10 km in altitude, with the data binned on a 3 months basis. I have shown clearly that the SAA is varying antiphased with the solar activity. This can be seen in the particle flux maps as well as in the fits to the particle flux distribution along the southernmost latitude. With the help of these fits it was further possible to measure the location of the SAA with an an accuracy of less than 0.25 deg. I have shown in agreement with previous works that the location of the SAA is moving slowly westwards with an average rate of $0.29\,\mathrm{deg\,year^{-1}}$. This movement is not smooth, however, but shows glitches, meaning that the SAA moves in the opposite direction. These glitches were not observed before, because no continuous investigations of the movement were available previous to this work. The glitches can be correlated with "geomagnetic jerks", which are sudden changes in the slow variation of the magnetic field of the Earth. These results are very promising and thus more work on the subject will be done. First of all, data from the "Reuven Ramaty High Energy Solar Spectroscopic Imager" (*RHESSI*) will be reduced. Similar to *RXTE* *RHESSI* is in a low-Earth orbit. *RHESSI* features are more sophisticated particle monitor than *RXTE*, which is able to distinguish between protons and electrons. As protons are drifting around the Earth in the opposite direction than electrons, slightly different locations of the SAA are expected. Furthermore, *RHESSI* is in an orbit with 38 deg inclination, which means that it will reach closer to the center of the SAA. This

might help to determine a north- or southward movement of the SAA. A northward movement is seen in the north-magnetic pole (Olsen & Mandea, 2007b), so that it is not unlikely that the SAA shows a similar behavior. The outer radiation belts can be examined with similar methods, too, using satellites in very eccentric orbits like the European "International Gamma-Ray Astrophysical Observertory" (*INTEGRAL*). Aboard *INTEGRAL* the "*INTEGRAL* Radiation Environment Monitor" (IREM) provides a good way to analyze the particle population in the radiation belts. The outer belts are under stronger influence from the solar wind, so that coronal mass ejections and the like should be clearly visible in the data. Mullen et al. (1991) have shown that during solar storms, a two-peaked structure of the inner radiation belt evolves, which should be also measurable with IREM. *INTEGRAL* data will be analyzed in the near future.

In Chapter 3 the high-mass X-ray binary Vela X-1 was studied. The data used for the analysis was all publicly available data of the system taken by *INTEGRAL*. Overall more than 3 Msec of data were analyzed. Lightcurves in different energy bands between 20–60 keV were extracted and the hardness-ratios were calculated. I could show that most of the times when Vela X-1 is in a very active state the hardness-ratio is lower than in quieter states. This softness is mirrored in the spectra taken separately for the more active and the quieter states. Additionally the spectra show increased absorption in the active state, which could be explained by a denser wind. A denser wind would mean that more mass can be accreted, so that the system would turn brighter. Additionally the denser wind would absorb more soft photons, so that the observed increased photon-index can be explained. To verify this theory, more spectra in different states of activity will be extracted in the future. These spectra will also provide a good possibility to test the stability of the cyclotron line. It is very likely that only the second harmonic can be measured with good enough statistics, but this measurement would still provide a good estimate for the magnetic field strength. No dependence between the cyclotron energy and the luminosity or flaring activity could be measured up to now. The large available dataset can provide a better statistic for this statement. Besides the spectra and hardness-ratios, I analyzed the flaring behavior of Vela X-1. It was easily seen that the system shows strong flaring, with some flares reaching around factor 70 of the average luminosity. I investigated this behavior in a statistical way. The flux distribution follows a log-normal distribution. It is seen, however, that in the softer 20–40 keV band a bright excess is measured. Bright excess means, that the right flank of the flaring distribution is not fitted well with a single log-normal distribution, but that a second distribution is needed. This excess is not visible in the harder 40–60 keV band. I take this as evidence that the brightest flares are distinctly softer than the average state of Vela X-1. This supports the observation in the hardness-ratios, which drops in the more active, and thus brighter, states. It is necessary to check the consistency of this analysis with a light-curve extracted with *ii_lc_extract* rather than *ii_light*. As *ii_lc_extract* uses a complete deconvolution of the shadowgram to calculate the fluxes of the sources, this takes a

long time to be calculated. This was not possible in the time frame of this diploma thesis, but will be done in the course of the following dissertation. The log-normal distribution of the flares can be explained qualtitatively by the clumped stellar wind of the optical companion. The same explanation is given for the flaring behavior of "Superfast X-Ray Transients" (SFXT) and so puts Vela X-1 into the same kind of system. The major difference is of course that Vela X-1 is a persistent source, whereas the SFTXs are, as the name suggests, transients. More statistical analysis of the flaring behavior of SFXTs is necessary to confirm this claim. Statistical data of the SFXT IGR J17544-2619 will be provided by David Smith (UC Santa Cruz) and will be analyzed in the the near future. Vela X-1 is only one amongst many HMXB systems, showing eclipses and cyclotron lines. Another prominent system is GX 301−2, which was analyzed in detail by Kreykenbohm (2004). New observations with *Suzaku* will become available in the next weeks and will be analyzed in the following dissertation. Additionally, archival data from *RXTE* as well as *INTEGRAL* is available, so that the flaring behavior can be studied on a large time-scale as well. It will be interesting to compare the two systems with respect to the flaring behavior in order to learn more about the physical process taking place in wind-accreting neutron stars.

A Appendix

List of Figures

List of Tables

Bibliography

Adolphsen J., Barth J.L., Stassinopoulos E.G., et al., 1995, IEEE Trans. Nuc. Sci. 42, 1964

Araya R.A., Harding A.K., 1999, ApJ 517, 334

Arnaud K.A., 1996, In: Jacoby G.H., Barnes J. (eds.) Astronomical Data Analysis Software and Systems V, Vol. 101. Astronomical Society of the Pacific Conference Series, p.17

Asikainen T., Mursula K., 2005, Geophys. Res. Lett. 32, 16102

Bacry E., Kozhemyak A., Muzy J., 2008, arXiv:physics.data-an:0804.0185v1 804

Badhwar G.D., 1997, J. Geophys. Res. 102, 2343

Badhwar G.D., Konradi A., Braby L.A., et al., 1994, Adv. Space Res. 14, 67

Barth J.L., Dyer C.S., Stassinopoulos E.G., 2003, IEEE Trans. Nuc. Sci. 50, 466

Barziv O., Kaper L., Van Kerkwijk M.H., et al., 2001, A&A 377, 925

Basko M.M., Sunyaev R.A., 1976, MNRAS 175, 395

Basset M., The AGILE Team 2007, Nuclear Instruments and Methods in Physics Research A 572, 474

Becker P.A., 1998, ApJ 498, 790

Becker P.A., Wolff M.T., 2005, ApJ 630, 465

Becker P.A., Wolff M.T., 2007, ApJ 654, 435

Becker-Guedes F., Sahai Y., Fagundes P.R., et al., 2007, Ann. Geophys. 25, 863

Bildsten L., Chakrabarty D., Chiu J., et al., 1997, ApJS 113, 367

Brown W.K., Wohletz K.H., 1995, J. App. Phys. 78, 2758

Brueckner G.E., Delaboudiniere J.P., Howard R.A., et al., 1998, Geophys. Res. Lett. 25, 3019

Bühler P., Desorgher L., Yehnder A., et al., 1996, Radiat. Meas. 26, 917

Caroli E., Stephen J.B., di Cocco G., et al., 1987, Space Science Reviews 45, 349

Chandrasekhar S., 1931, ApJ 74, 81

Chodil G., Mark H., Rodrigues R., et al., 1967, ApJ 150, 57

Courvoisier T.J.L., Walter R., Beckmann V., et al., 2003, A&A 411, L53

Dachev P., Tomov B.T., Matviichuk Y.N., et al., 1999, Rad. Meas. 30, 269

Davidson K., Ostriker J.P., 1973, ApJ 179, 585

de Chambure D., Lainé R., van Katwijk K., Kletzkine P., 1999, ESA Bulletin 100, 30

Deeter J.E., Boynton P.E., Lamb F.K., Zylstra G., 1989, ApJ 336, 376

Di Cocco G., Caroli E., Celesti E., et al., 2003, A&A 411, L189

Einstein A., 1905, Annalen der Physik 322, 549

Elsasser W.M., 1946, Phys. Rev. 69, 106

Fowler R.H., 1926, MNRAS 87, 114

Frank J., King A., Raine D., 1992, Cambridge Astrophysics Series 21

Fritz S., 2008, Ph.D. thesis, Eberhard-Karls-Universität Tübingen

Fürst F., Wilms J., Rothschild R., et al., 2008, in prep.

Garrett H.B., Hastings D., 1994, In: 32nd Aerospcae Sciences Meeting & Exhibit., AIAA, AIAA, Reston, p.590

Giacconi R., Gursky H., Kellogg E., et al., 1971, ApJ 167, L67

Giacconi R., Gursky H., Paolini F.R., Rossi B.B., 1962, Phys. Rev. Let. 9, 439

Giacconi R., Murray S., Gursky H., et al., 1974, ApJS 27, 37

Gilbert W., 1991, De Magnete, Courier Dover Publications Facsimile of 1893 Mottelay translation

Ginet G.P., Thompson T., Madden D., Easley S.M., 2006, AGU Fall Meeting Abstracts A1359

Gleissner T., Wilms J., Pottschmidt K., et al., 2004, A&A 414, 1091

Goldwurm A., David P., Foschini L., et al., 2003, A&A 411, L223

Golian S.E., Krause E.H., Perlow G.J., 1946, Physical Review 70, 223

Grämer C., 2008, Zyklotronlinien – eine RXTE-Sample, Zulassungsarbeit an der Dr. Remeis-Sternwarte Bamberg

Grigoryan O.R., Petrov A.N., Romashova V.V., 2005, In: WDS '05 Proceedings of Contributed Papers, Vol. 2., Matfyzpress, Prague, p.251

Groeneveld H.A., 1999, Ph.D. thesis, Eberhard-Karls-Universität Tübingen

Hamann W.R., Feldmeier A., Oskinova L.M., (eds.) 2008, Clumping in hot-star winds

Harrington J.D., Harris D., Cominsky L., 2008, `http://www.nasa.gov/mission_pages/GLAST/news/glast_renamed.html`

Hilditch R.W., 2001, An Introduction to Close Binary Stars, An Introduction to Close Binary Stars, by R. W. Hilditch, Cambridge, UK: Cambridge University Press, March 2001.

Huston S.L., Kuck G.A., Pfitzer K.A., 1996, In: Lemaire J.F., Heyndericks D., Baker D.N. (eds.) Radiation Belts: Models and Standards., AGU Geophysical Monograph 97, AGU, Washington, p.119

Iben I.J., 1991, ApJS 76, 55

Iben I.J., Tutukov A.V., Yungelson L.R., 1995, ApJS 100, 217

Inoue H., Ogawara Y., Waki I., et al., 1984, PASJ 36, 709

in't Zand J.J.M., 1992, Ph.D. thesis, AA(Space Research Organization Netherlands, Sorbonnelaan 2, 3584 CA Utrecht, The Netherlands)

Jahoda K., Markwardt C.B., Radeva Y., et al., 2006, ApJS 163, 401

Johnston S., Manchester R.N., Lyne A.G., et al., 1992, ApJ 387, L37

Karttunen H., Krüger P., Oja H., et al., (eds.) 2007, Fundamental Astronomy, Fundamental Astronomy, Edited by H. Karttunen, P. Krüger, H. Oja, M. Poutanen, and K.J. Donner. Berlin: Springer, 2007.

Kelley R., Mitsuda K., 2002, APS Meeting Abstracts 11002

Kendziorra E., Mony B., Kretschmar P., et al., 1992, In: Tanaka Y., Koyama K. (eds.) Frontiers Science Series., p.51

Kepler J., 1609., Astronomia nova seu, Physica coelestis, tradita commentariis De motibus stellae martis, ex observationibus G.V. Tychonis Brahe, Kepler, Johannes

Killeen J., Hess W.H., Lingenfelter R.e., 1963, J. Geophys. Res. 68, 4637

Konradi A., Badhwar G.D., Braby L.A., 1994, Adv. Space Res. 14, 911

Kretschmar P., Kreykenbohm I., Wilms J., et al., 1997a, In: Winkler C., Courvoisier T.J.L., Durouchoux P. (eds.) The Transparent Universe, Vol. 382. ESA Special Publication, p.141

Kretschmar P., Pan H.C., Kendziorra E., et al., 1997b 325, 623

Kreykenbohm I., 2004, Ph.D. thesis, Eberhard-Karls-Universität Tübingen

Kreykenbohm I., Coburn W., Wilms J., et al., 2002, A&A 395, 129

Kreykenbohm I., Kretschmar P., Wilms J., et al., 1999, A&A 341, 141

Kreykenbohm I., Wilms J., Kretschmar P., et al., 2008, A&A

Lamb F.K., Pethick C.J., Pines D., 1973, ApJ 184, 271

Lauriente M., Vampola V.L., Gosier K., 1996, In: Lemaire J.F., Heyndericks D., Baker D.N. (eds.) Radiation Belts: Models and Standards., AGU Geophysical Monograph 97, p.109

Lebrun F., Leray J.P., Lavocat P., et al., 2003 411, L141

Levine A.M., Bradt H., Cui W., et al., 1996, Astrophys. J., Lett. 469, L33

Lipunov V.M., 1992, Astrophysics of Neutron Stars, Berlin: Springer

Lomb N.R., 1976, Ap&SS 39, 447

Lund N., Budtz-Jørgensen C., Westergaard N.J., et al., 2003, A&A 411, L231

Mandea M., Bellanger E., Le Mouël J.L., 2000, Earth Planet. Sci. Lett. 183, 369

Matsuda T., Inoue M., Sawada K., 1987, MNRAS 226, 785

McClintock J.E., Rappaport S., Joss P.C., et al., 1976, Astrophys. J., Lett. 206, L99

Michelson P.F., 2008, APS Meeting Abstracts L2002

Mullen E.G., Ginet G., Gussenhoven M.S., Madden D., 1998, IEEE Trans. Nuc. Sci. 45, 2954

Mullen E.G., Gussenhoven M.S., Ray K., Violet M., 1991, IEEE Trans. Nuc. Sci. 38, 1713

Nagase F., Hayakawa S., Sato N., et al., 1986, PASJ 38, 547

Olsen N., Mandea M., 2007a, Earth Planet. Sci. Lett. 255, 94

Olsen N., Mandea M., 2007b, EOS Transactions 88, 293

Padmanabhan T., 2001, Theoretical Astrophysics, Volume 2: Stars and Stellar Systems, Theoretical Astrophysics, Cambridge, UK: Cambridge University Press, April 2001.

Pavia E.G., O'Brien J.J., 1986, Journal of Applied Meteorology 25, 1324

Pinto, Jr. O., Gonzalez W.D., Pinto I.R.C.A., et al., 1992, J. Atmos. Terrest. Phys. 54, 1129

Pittori C., Cutini S., Gasparrini D., et al., 2008, The Astronomer's Telegram 1583

Pottschmidt K., Rothschild R.E., Gasaway T., et al., 2006, In: Bulletin of the American Astronomical Society, Vol. 38. Bulletin of the American Astronomical Society, p. 384

Poutanen J., Zdziarski A.A., Ibragimov A., 2008, MNRAS 389, 1427

Prölss G.W., 2001, Physik des erdnahen Weltraums : Eine Einführung, Springer-Verlag Berlin Heidelberg New York

Quaintrell H., Norton A.J., Ash T.D.C., et al., 2003, A&A 401, 313

Raubenheimer B.C., 1990, A&A 234, 172

Ritz S., 2008, `http://blogs.nasa.gov/cm/blog/GLAST`

Roberts P.H., Glatzmaier G.A., 2000, Rev. Modern Phys. 72, 1081

Roe B.P., 2001, Probability and statistics in experimental physics, Springer-Verlag New York, 2nd edition

Rothschild R.E., 1996, `http://mamacass.ucsd.edu:8080/hexte/status/hexte_status_960307.html`

Rothschild R.E., Blanco P.R., Gruber D.E., et al., 1998, Astrophys. J. 496, 538

Rybicki G.B., Lightman A.P., 1986, Radiative Processes in Astrophysics, Wiley-VCH, New York

Sadakane K., Hirata R., Jugaku J., et al., 1985, ApJ 288, 284

Sauvaud J.A., Maggiolo R., Jacquey C., et al., 2008, Geophys. Rev. Lett. 35, 9101

Sawyer D.M., Vette J.I., 1976, NASA STI/Recon Technical Report N 77, 18983

Scargle J.D., 1998, ApJ 504, 405

Schanne S., Gotz D., Gerard L., et al., 2007, In: Proceedings of the 6th INTEGRAL Workshop, Moscow, 2006 07 03-07, ESA SP-622 .

Schönherr G., Wilms J., Kretschmar P., et al., 2007, A&A 472, 353

Schreier E.J., 1978, In: van der Hucht K.A., Vaiana G. (eds.) Advances in Space Exploration., p.189

Sekine M., Chen C.D., Musha T., 1987, IEEE Transactions on Antennas and Propagation 35, 358

Smirnoff N.W., 1939, Bull. University Moskov Ser. Internat 3–8

Staubert R., Kendziorra E., Pietsch W., et al., 1980, ApJ 239, 1010

Staubert R., Kreykenbohm I., Kretschmar P., et al., 2004, In: Schoenfelder V., Lichti G., Winkler C. (eds.) 5th INTEGRAL Workshop on the INTEGRAL Universe, Vol. 552. ESA Special Publication, p.259

Stouffer D.B., Malmgren R.D., Amaral L.A.N., 2006, arXiv:physics/0605027

Suchy S., Pottschmidt K., Wilms J., et al., 2008, ApJ 675, 1487

Swank J., 2007, The RXTE technical appendix F, NASA / GSFC, `http://heasarc.gsfc.nasa.gov/docs/xte/RXTE_tech_append.pdf`

Szajnowski W., 1977, IEEE Transactions on Aerospace Electronic Systems 13, 480

Tanaka Y., 1986, In: Mihalas D., Winkler K.H.A. (eds.) IAU Colloq. 89: Radiation Hydrodynamics in Stars and Compact Objects, Vol. 255. Lecture Notes in Physics, Berlin Springer Verlag, p.198

Taylor B.G., Andresen R.D., Peacock A., Zobl R., 1981, Space Science Reviews 30, 479

Tretyakov S., 2007, Metamaterials 1, 40

Trümper J., 1990, In: Gorenstein P., Zombeck M. (eds.) IAU Colloq. 115: High Resolution X-ray Spectroscopy of Cosmic Plasmas., p.291

Turolla R., Zane S., Titarchuk L., 2002, ApJ 576, 349

Ubertini P., Lebrun F., Di Cocco G., et al., 2003 411, L131

Ulmer M.P., Baity W.A., Wheaton W.A., Peterson L.E., 1972, Astrophys. J., Lett. 178, L121

Uttley P., McHardy I.M., 2001, MNRAS 323, L26

Uttley P., McHardy I.M., Vaughan S., 2005, MNRAS 359, 345

van Allen J.A., 1958, Radiation belts around the earth, San Francisco: Freeman, 1958

van den Heuvel E.P.J., 1995, Journal of Astrophysics and Astronomy 16, 255

van Kerkwijk M.H., van Paradijs J., Zuiderwijk E.J., et al., 1995, A&A 303, 483

Vedrenne G., Roques J.P., Schönfelder V., et al., 2003, A&A 411, L63

Verrecchia F., Gasparrini D., Cutini S., et al., 2008, The Astronomer's Telegram 1582

Vette J.I., 1991, NASA STI/Recon Technical Report N 92, 24228

Walt M., 1994, Camb. Atmos. Space Sci. Ser., Vol. 10, 10

Walter R., Zurita Heras J., 2007 476, 335

Wardinski I., Holme R., Asari S., Mandea M., 2008, Earth Planet. Sci. Lett. 267, 468

Weibull W., 1951, J. Appl. Mech.-Trans. ASME 18(3)

Weisskopf M.C., Tananbaum H.D., Van Speybroeck L.P., O'Dell S.L., 2000, In: Truemper J.E., Aschenbach B. (eds.) Proc. SPIE Vol. 4012, 2-16, X-Ray Optics, Instruments, and Missions III, Vol. 4012., p.2

Winkler C., Courvoisier T.J.L., Di Cocco G., et al., 2003 411, L1

Wolter H., 1952, Annalen der Physik 445, 286

Danksagung

Ich danke allen, die mich beim Erstellen dieser Arbeit unterstützt und begleitet haben. Besonderer Dank gilt meinem Betreuer Jörn Wilms, der immer für Fragen zur Verfügung stand und mit seinem weitreichenden Wissen mir immer wieder neue Impulse geben konnte. Außerdem will ich Ingo Kreykenbohm in besonderem Maße danken, weil er mich bei der Analyse der *INTEGRAL* Daten immer unterstützt hat und mir die Dinge auch nach der zehnten Nachfrage noch geduldig erklärt hat. Der gesamten Röntgenarbeitsgruppe der Sternwarte danke ich für die gute Atmosphäre im Büro. Namentlich Manfred Hanke, unseren ISIS-Mann, Moritz Böck der meine Arbeit fleißig Korrektur gelesen hat, Laura Barrágan für die Hilfe bei den Spektren, Stefan Pirner und Christian Schmid für die fruchtbaren Diskussionen. Außerdem Christian Grämer, dessen Arbeit mir sehr weitergeholfen hat. Den restlichen Mitarbeitern der Sternwarte möchte ich für die netten Mittagspausen und die auflockerenden Gespräche danken.

Ich danke allen Mitarbeitern an der UCSD für ihre hilfreichen Ideen und den freundlichen Empfang. Besonderer Dank geht an Slawo Suchy, bei dem ich in San Diego wohnen durfte, sowie Rick Rothschild and Richard Lingenfelter, die mir gute Ideen die SAA betreffend geliefert haben. Dabei will ich auch Katja Pottschmidt meinen Dank aussprechen, auf deren Arbeit meine Analyse der HEXTE Hintergründe aufbaut.

Darüberhinaus danke ich natürlich meinen Freunden und Kommilitonen, daß ich mit meinem Physik-Studium überhaupt so weit gekommen bin und nicht schon am Anfang verzweifelt bin. Besonders den Mitgliedern der Fachschaft möchte ich danken, da sie mir gezeigt haben, dass die Uni aus mehr als nur Physik besteht.

Nichtzuletzt möchte ich meiner Freundin danken, die immer zu mir gehalten hat und mich immer wieder motiviert hat, weiterzumachen. Ich denke, während der Promotion werde ich noch viel mehr auf sie angewiesen sein und bedanke mich jetzt schon für ihre Liebe und ihr Vertrauen. Meinem Vater gebührt auch großer Dank, dass er mir das Physik-Studium ermöglicht hat und mit mir über die Sterne und das Universum diskutiert hat.

Hiermit erkläre ich, dass ich die Arbeit selbstständig angefertigt und keine anderen als die angegebenen Hilfsmittel verwendet habe.

Bamberg, 24. September 2008

Felix Fürst